

UNIVERSITY OF ALBERTA

REFINED TRANSVERSE SHEAR STRAINS IN THICK
PLATE-SHELL ELEMENTS

BY

MANSOUR ZIYAEIFAR



A thesis submitted to the Faculty of Graduate Studies and Research in partial fulfilment
of the requirements for the degree of Doctor of Philosophy in
Structural Engineering

DEPARTMENT OF CIVIL ENGINEERING

EDMONTON, ALBERTA

Fall, 1996



National Library
of Canada

Acquisitions and
Bibliographic Services Branch

395 Wellington Street
Ottawa, Ontario
K1A 0N4

Bibliothèque nationale
du Canada

Direction des acquisitions et
des services bibliographiques

395, rue Wellington
Ottawa (Ontario)
K1A 0N4

Your file Votre référence

Our file Notre référence

The author has granted an irrevocable non-exclusive licence allowing the National Library of Canada to reproduce, loan, distribute or sell copies of his/her thesis by any means and in any form or format, making this thesis available to interested persons.

L'auteur a accordé une licence irrévocable et non exclusive permettant à la Bibliothèque nationale du Canada de reproduire, prêter, distribuer ou vendre des copies de sa thèse de quelque manière et sous quelque forme que ce soit pour mettre des exemplaires de cette thèse à la disposition des personnes intéressées.

The author retains ownership of the copyright in his/her thesis. Neither the thesis nor substantial extracts from it may be printed or otherwise reproduced without his/her permission.

L'auteur conserve la propriété du droit d'auteur qui protège sa thèse. Ni la thèse ni des extraits substantiels de celle-ci ne doivent être imprimés ou autrement reproduits sans son autorisation.

ISBN 0-612-18141-3

Canada

University of Alberta

Library Release Form

Name of Author: Mansour Ziyaeifar

Title of Thesis: Refined Transverse Shear Strains in Thick Plate-Shell Elements.

Degree: Doctor of Philosophy

Year this Degree Granted: 1996

Permission is hereby granted to the University of Alberta Library to reproduce single copies of this thesis and to lend or sell such copies for private, scholarly, or scientific research purposes only.

The author reserves all other publication and other rights in association with the copyright in the thesis, and except as hereinbefore provided, neither the thesis nor any substantial portion thereof may be printed or otherwise reproduced in any material form whatever without the author's prior written permission.

M. Ziyaeifar

220, Civil/Elec. Bldg.,
University of Alberta,
Edmonton, Alberta, T6G 2G7.

Date: Sept. 27th, 1996

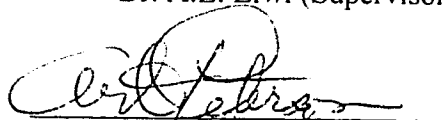
University of Alberta

Faculty of Graduate Studies and Research

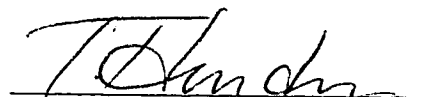
The Undersigned certify that they have read, and recommend to the Faculty of Graduate Studies and Research for acceptance, a thesis entitled "Refined Transverse Shear Strains in Thick Plate-Shell Elements" submitted by Mansour Ziyaeifar in partial fulfilment of the requirements for the degree of Doctor of Philosophy in Structural Engineering.



Dr. A.E. Elwi (Supervisor)



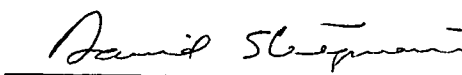
Prof. Dr. A. E. Peterson



Dr. T. M. Hrucey



Dr. S.D.B. Alexander



Dr. D. J. Steigmann



Dr. A. Ghali (External Examiner)

Date: Aug. 27, 1996

To:
my beloved parents

ABSTRACT

High transverse shear force regions in concrete plates and shells have always been a controversial subject in structural design and analysis. Punching shear in the slab-column connections is a case in point. Existing building codes all over the world do not have a common approach to handle this phenomenon and could be unduly conservative. Offshore structures and highly pressurized concrete containments are other examples in which the presence of high transverse shear forces makes it hard to determine the failure mode, ductility and thus reliability of the design in the analysis process.

Numerical analysis of structure by finite element method offers a substitute to expensive experimental investigations in such cases. Nevertheless, the available finite element models for concrete plates or shells are not accurate in the regions of high transverse shear force. Inaccuracy in finite element analysis of concrete shells and plates stems from the strain field approximation and material model idealization. To address the former a new plate-shell element with a refined strain field is developed in this work. This element which is called "*Refined Degenerated Shell Element*", is capable of adjusting its strain field approximation to the actual situation of strain in the structure more closely than that of other shell elements. This unique characteristic is especially important in the case of concrete plates and shells which are subjected to diffuse material failure across the thickness. The concrete material model is another issue which needs special consideration. In this work a three dimensional material model based on the fracture energy and plasticity approaches for concrete is integrated into the finite element model of plate and shells to remove the problems associated with inclined cracking in zones of high transverse shear force. Tension stiffening is also addressed and its implementation in the finite element modeling of these problems discussed.

Examples to verify the new shell element are presented. The material model is also verified in special cases that are pertinent to ordinary stress fields in thin plates and shells. Lastly, the results of numerical analysis of different thick plate and beam type structures in the presence of high transverse shear forces are attempted and discussed.

ACKNOWLEDGMENTS

This project would not have been possible without the help of so many people. The challenging academic and scientific environment in the University of Alberta was the inspiration behind my research and it is appreciated. The author is deeply indebted to Dr. A.E. Elwi for his invaluable help, support and guidance throughout the course of this thesis. My understanding and strength in this research area is also owed in part to Dr. T.M. Hruddy and Dr. D.H. Chan and I am truly thankful to them.

The funding of this project was provided in part by the Natural Sciences and Engineering Research Council of Canada and the Ph.D. scholarship by the Iranian Ministry of Culture and Higher Education. The author wishes to express his gratitude to these sources.

There are numerous colleagues whom I would like to thank, in particular N. Yoosof-Ghods, S. Afhami, R. Driver and A. Touhidi-Baghini for their valuable suggestions and also for their friendship. The support and encouragement of my parents and my sisters during this work were of great value and I am eternally grateful to them.

TABLE OF CONTENTS

CHAPTER	Page
1. INTRODUCTION	1
1.1. PROBLEM STATEMENT	1
1.2. BACKGROUND AND REVIEW	2
1.3. RESEARCH OBJECTIVES AND SCOPE	4
1.4. LAYOUT OF THE THESIS	5
2. REFINED STRAIN FIELD IN THE REGIONS OF HIGH TRANSVERSE SHEAR FORCES..	7
2.1 Introduction And Literature Survey	7
2.1.1 Refined Shell Elements	10
2.2 Adjustable Refined Bending Theory For Shells	12
2.3 Proposed Refined Strain Field In This Study	15
2.4 Refined Degenerated Shell Elements	16
2.4.1 Large Deformation Formulation	20
2.4.1.1 Geometric Transformation	21
2.4.1.2 Finite Element Displacement Field	21
2.5 Finite Element Formulation	23
2.5.1 Field Equations	23
2.5.2 Derivation of The Strain Displacement Matrix	24
2.5.3 Stress State Matrix and Vector	31
2.6 Boundary Conditions	31
2.7 Programming	34
3. VERIFICATION OF THE REFINED ELEMENT	46
3.1 Introduction	46
3.1. Elastic Behavior of Thin and Thick Shells	46
3.2. Elastic-Plastic Analysis of Plate	47
3.3. Plate with Unsymmetric Material Behavior Across the Thickness	48
3.4. Strain Dist. Close to the Point of Discontinuity of Shear Force	48

4. FINITE ELEMENT MODELING OF CONCRETE SHELLS AND PLATES	58
4.1 Introduction	58
4.2 Single Crack Development and Localization	58
4.2.1 Mesh Dependency	59
4.2.1.1 Mesh Size	61
4.2.1.2 Mesh Alignment	62
4.3 Concrete Material Model	63
4.3.1 Three dimensional constitutive model	66
4.3.2 Fracture Energy Based Plasticity Model	68
4.3.2.1 Isotropic Hardening model	68
4.3.2.2 Isotropic softening model	68
4.3.3 Implementation of 3D Material Model in Plate and Shell	71
4.3.4 Programming	72
4.4 Tension Stiffening	73
4.5 Verification of the Concrete Material Model	75
4.5.1 Description of Specimens	76
4.5.2 Finite element model for PV-Series	76
4.5.3 Prediction of the PV-Panels Response	76
4.5.3.1 Response of the Specimens in Pure Shear	78
4.5.3.2 Response to Combined In-plane Normal and Shear Forces	79
5. RESULTS AND DISCUSSION	89
5.1. Introduction	89
5.2. Description of specimens	90
5.2.1. Shear Failure in Thick Plates	90
5.2.2. Slab-Column Connection	91
5.3. Observations In The Analysis	92
5.3.1. Refined Degenerated Shell Element in Concrete Structures	93
5.3.1.1. Strain field idealization	93
5.3.1.2. Integration across the thickness	96
5.3.1.3. Sensitivity in the analysis	97
5.3.2. Concrete Material Model for Plates and Shells	98
5.3.2.1. Concrete material model in general state of stress	98
5.3.2.2. Extensive cracking	100
5.3.2.3. Sensitivity to the increment of strain	101
5.3.2.4. Numerical instability	102
5.4. Prediction of The Response of The Specimens	106
5.4.1. Shear Failure in Thick Plates	106
5.4.2. Slab-Column Connection	109

6. SUMMARY AND CONCLUSION	140
6.1. Summary	140
6.2. Conclusion	142
7. REFERENCES	144

LIST OF TABLES

Table		Page
4.1	PV panels material properties	82
5.1	Material properties and loading mechanism of the SP panels	113
5.2	Reinforcement arrangement for edge slab-column connection	114
5.3	Reinforcement arrangement for interior slab-column connection	114

LIST OF FIGURES

Figure		Page
2.1	Love-Kirchhoff hypothesis on bending	36
2.2	Mindlin-Reissner hypothesis on bending	37
2.3	Layered shell element	38
2.4	Solid-shell element	39
2.5	Third order deformation theory	40
2.6	Multi-layered shell	41
2.7	Strain distribution in the case of diffused material failure	42
2.8	Shape function across the thickness	43
2.9	Definition of rotational degrees of freedom	44
2.10	Displacement and shear strain distribution across the thickness	45
3.1	Thin shell example, vertical deflection of central point	50
3.2	Thin shell example, stress distribution at point A	51
3.3	Thick shell example, normal stress distribution at point A	52
3.4	Plate supported at corners, stress dist. at point A	53
3.5	Plate supported at corners, vertical defl. at point A	54
3.6	Plate supported at centre, stress distribution at point A	55
3.7	Beams loaded at mid-span and at 1/4 of span	56
3.8	Shear stress close to points of shear force discontinuity	57
4.1	Tension stiffening	83
4.2	Strain softening in different combination of bi-axial stress	83
4.3	Load application Mechanism on PV panels (Vecchio and Collins1982)	84
4.4	Finite element model for PV series	84
4.5	Finite element analysis of PV-4 with different reinforcement ratio	85
4.6	Finite element analysis and experimental results for panel PV-4	85
4.7	Finite element analysis and experimental results for panel PV-6	86
4.8	Finite element analysis and experimental results for panel PV-27	86
4.9	Finite element analysis and experimental results for panel PV-23	87
4.10	Comparison between PV-23 and PV-27	87

4.11	Finite element analysis and experimental results for panel PV-28	88
5.1	Cross section and reinforcement pattern of the SP specimens	115
5.2	Finite element of SP-Series specimens and their loading mechanism	116
5.3	Finite element model of the Afhami et al. slab-column connection	117
5.4	Transverse shear strain distribution across the thickness in SP3	118
5.5	Shear strain distribution in the case of simultaneous softening of the cross section at top and bottom	119
5.6	Shear strain distribution constructed based on refined approach	119
5.7	Refined shell based finite element model of a deep beam	120
5.8	Transverse shear strain distribution in deep beam with different k_u	121
5.9	Proposed shape function for simultaneous softening at extreme fibers with the associated shear strain distribution	122
5.10	Normal strain distribution across the thickness in SP3 specimen	123
5.11	Transverse shear stress distribution across the thickness in SP3	124
5.12	Normal stress distribution across the thickness in SP3 specimen	125
5.13	Distribution of normal stress at a point close to column face in the Afhami et al. slab-column connection	126
5.14	Sensitivity of concrete material model to the increment of strain	127
5.15	Shear stress distribution across the thickness in SP3 at high load level	128
5.16	Normal stress dist. across the thickness in SP3 at high load level	129
5.17	Normal and shear stress dist. in SP3 at two consecutive load steps	130
5.18	Normal and shear stress dist. in SP3 at two consecutive load steps.	131
5.19	Time history of angle of similarity in SP3 for points across the thickness	132
5.20	Normal stress dist. across the thickness in SP3 at high load level	133
5.21	In-plane shear stress vs. principal strain in SP8 specimen	134
5.22	Load-deformation response of SP3 specimen	135
5.23	Load deformation behavior of the Afhami et al. slab-column connection at point C	136
5.24	Shear intensity distribution on the face of interior strip and edge strip in the Afhami et al. specimen	137
5.25	Torsional moment intensity on the face of interior strip and edge strip in the Afhami et al. specimen	138
5.26	Tension in outer layer of reinforcement in the Afhami et al. slab-column connection	138
5.27	Shear stress distributions in Afhami et al. slab-column connection using refined and ordinary shell elements	139

LIST OF SYMBOLS

* Latin Characters

A_c	Crack surface area in compression
A_t	Crack surface area in tension
$[^m B_L]_n$	Matrix of strain-displacement approximation
$[^m B_{NL}]_n$	Matrix of displacement derivative approximation
$[C]$	Constitutive matrix
C^0	Displacement continuity condition
C^1	Displacement derivative continuity condition
c_{ijkl}	Constitutive tensor
D_{ij}^n	Displacement derivative transformation parameter
E	Modules of elasticity
EI_{eff}	Effective cross sectional properties of concrete plates
e_{ij}	Strain tensor
$\{e\}$	Strain vector
$f(t)$	Shape function for linear variation of displacement
$f_c^{'}$	Compressive strength of concrete
$f_t^{'}$	Tensile Strength of concrete
f_y	Yield stress of steel
F_{ij}^n	Rotation-displacement transformation component at node n
$[F_n(^m \psi_1, ^m \psi_2)]$	Rotation-displacement transformation matrix in current configuration m at node n
$g(t)$	Shape function for parabolic shear strain across the thickness
$g^{'}(t)$	Derivative of function $g(t)$ in the thickness direction

G_f	Fracture energy release rate
G_f^I	Fracture energy in tension
G_f^{II}	Fracture energy in shear
h	Shell thickness
h_t	Tensile crack spacing in concrete
h_c	Compression crack spacing in concrete
$[^mH]$	Strain gradient template matrix
$[J]$	Jacobian of transformation
J_2, J_3	Second and third deviatoric invariants in the stress space
j_{ij}^{-1}	The components of the matrix of inverse Jacobean
k	Hardening parameter in concrete material
k_0	Initial value for hardening parameter
k_p	Peak value for hardening parameter
$k(\tilde{\varepsilon}_p, \chi_p)$	Hardening rule in concrete material
$k(t)$	Shape function for unsymmetric shear strain distribution
$k'(t)$	Derivative of function $k(t)$ in the thickness direction
$[K_L]$	Linear stiffness matrix
$[K_{NL}]$	Geometric stiffness matrix
L	Vector length in transformation matrix
l	Total number of nodes in one element
$l(t)$	Shape function for multi-layered shell structures
$[N]_n$	Interpolation sub-matrix at node n
$[^mN'(\zeta, \eta, t)]^n$	Derivative of the interpolation sub-matrix in local coordinate for incremental displacement in current configuration m at node n
$[^m\tilde{N}'(\zeta, \eta, t)]^n$	Derivative of the interpolation sub-matrix for total displacement
$q(t)$	Shape function for simultaneous softening at top and bottom
$\{^mQ\}$	Internal equilibrating force vector at current configuration

$\{^m \cdot^l R\}$	The load level in the current configuration
$[^m S]$	Stress matrix in current configuration
$\{^m \hat{S}\}$	Stress vector in current configuration
$^m S_{ij}$	Second Piola-Kirchhoff stress tensor
$^m u_i(t)$	Displacement in current configuration
$\{u\}_n$	Incremental displacement vector for node n
$\{u_{i,j}\}_n$	Incremental displacement derivative vector for node n
$\{^m u_{i,j}\}_n$	Displacement derivative vector in current configuration at node n
$\{^m \bar{u}\}^n$	Displacement vector for node n
$\{\nabla u\}$	Derivative of increment of displacement vector
$u_\theta, v_\theta, w_\theta$	Translational displacement of mid-cross section in plates
$u_\alpha, u_\beta, u_\lambda$	Cross section displacement attributed to each shape function
u_f	Fracture displacement of concrete in tension
u_γ	Cross section displacement attributed to shear deformation
u, v, w	Displacement in global frame of reference
V	Volume
x, y, z	Axis in Global frame of reference
$\{\Delta^m x\}$	Displacement translational vector in the current configuration

*** Greek Characters**

$\alpha, \beta, \lambda, \eta$	Shape function coefficients
$\{\alpha_i\}_n$	Rotational degrees of freedom at node n
$\{\beta_i\}_n$	Refined degrees of freedom for parabolic shear strain at node n
χ_p	Ductility parameter in concrete material
δ	Variation notation

ε_{ij}	Strain tensor
$\tilde{\varepsilon}_p$	Plastic strain indicator
$\tilde{\varepsilon}_f$	Fracture strain indicator
ϕ^n	Interpolation shape function on the mid-surface at node n
$\phi^n_{,i}$	Shape function derivatives on the mid-surface for translational degrees of freedom at node n
$\phi_\alpha^n_{,i}$	Shape function derivatives on mid-surface for rotational and refined degrees of freedom at node n
$\gamma_{xz}(z)$	Shear strain distribution across the thickness
η_{ij}	Nonlinear part of increment of Green-Lagrange strain tensor
$\{\lambda_i\}_n$	Refined degrees of freedom for unsymmetric shear strain at node n
ν	Poisson ratio
θ	Angle of similarity in plasticity model
σ_{ij}	Stress tensor
${}^m\psi_i$	Rotational deformation of nodes in current configuration
ξ, η, t	Natural coordinate in shell element

*There was a song,
like a whisper in the busy air,
very deep into the sky.*

*There were only a few,
digging out the sky searching for it.*

*They never found it, but ... ,
they flew.*

.... , nobody has ever heard of them since.

CHAPTER ONE

INTRODUCTION

1.1. PROBLEM STATEMENT

Large scale concrete plate and shells are becoming more and more popular in the design and construction of huge and important structures specially in offshore environments. The advantages of concrete plates and shells include not only the cost of the structure but also its low heat conductivity and better structural damping characteristics among others. This area of application of concrete shells is flourishing rapidly. Design of huge LNG (Liquid Natural Gas) super-tankers made of reinforced concrete are examples showing the popularity of this trend. In the design process of such important projects, a powerful analysis tool is required to ensure the availability of sufficient ductility and thus reliability of the structure. The major concern is to improve the accuracy of analysis in determining the failure mode and post peak behavior of the structure. The problem in these cases arises mostly at the intersection of plates and shells with different flexural characteristics. At such intersections a high out of plane shear force is expected due to load transfer from a flexible shell to a stiffer one. Collision with icebergs or other moving objects is another example that could cause concentrated shear forces in the structure. These high transverse shear zones increase the possibility of brittle failure and must be predicted in the analysis and prevented in the design.

Analysis and design of concrete plates and shells in the regions of high transverse shear forces have always been controversial. Designing for punching shear around columns in slabs is a graphic example of this case. The degree of uncertainty in understanding the behavior of the structure in this region causes discrepancy in the design rules in different building codes all over the world.

1.2 BACKGROUND AND REVIEW

Plates and shells are highly indeterminate structures. In concrete shells and plates progressive material failure is expected almost from the beginning of the loading process. Thus, the load carrying mechanism in the structure varies through different stages in the loading history. Therefore, in some cases it is hard to predict the final mode of failure. Determining the failure mode and the post peak behavior of the structure are the priorities in every analysis of a reinforced concrete structure, required to satisfy ductility and reliability conditions. However, the existence of high transverse shear forces in shells and plates causes a great deal of inaccuracy in the conventional analysis techniques and sometimes make it impossible to capture the brittle mode of failure in the analysis process.

In order to illustrate the complexity involved in the analysis of plates and shells in the regions of high transverse shear forces, one may examine the most common example in this area; the punching shear problem in slab-column connections. After a large number of experimental and analytical studies on this subject, there is still a great deal of controversy about the mechanism of punching shear in the slab-column connections (see, for example, Moe 1961, Regan et al. 1985, Moenle et al. 1988 and Alexander et al. 1992). Investigations in this area are mostly experimental. The primary reason is the relatively low cost of a full scale test of a slab-column connection.

Investigation in the other examples of the occurrence of high transverse shear force such as offshore structures or highly pressurized containments involve costly experimental studies. This restricts the number of these experiments to only a few tests on smaller scale models of the actual structures or its components (see McLean 1987, Saito et al. 1989 and Horschel 1988-a and b). The only alternative method of investigation is numerical analysis. The work by Clauss (1987 and 1989) and Weatherby (1990) are examples in which pre-test and post-test finite element analysis of an experimental study have been carried out in order to justify and improve the numerical analysis techniques.

The need for an accurate prediction of the response of these structures has stimulated research activities in the field of computational analysis of concrete structures during the last 25 years. Advancement in the areas of nonlinear solution techniques, concrete constitutive modelling and enhancement in strain field approximation in the finite element method have made the analysis of complex concrete structures possible. Nevertheless there are several shortcomings in the current analysis techniques particularly in plate and shell structures.

The source of inaccuracy in finite element analysis of concrete plates and shells in the regions of high transverse shear force, is rooted in both strain field approximations and material model representations.

Concrete plates and shells exhibit a complex structural response with various important nonlinearities in the constitutive behavior of concrete. Progressive material failure throughout the thickness due to tensile cracking and compression crushing of concrete, causes a complicated distribution of strain in the thickness direction that varies in accordance with the level of progression of material failure. This behavior in concrete plates and shells requires special treatment at the level of strain field approximations in the finite element method. In other words, refinement techniques are required to keep the strain field approximation in the finite element method as close as possible to the actual strain field in the structure.

The transverse shear force in the structure is accompanied by shear deformation. The out of plane shear strain associated with this deformation is not uniformly distributed across the thickness. As an example in the case of elastic materials, a parabolic distribution of shear strain across the thickness is expected. A more complicated distribution of strain is anticipated when a diffused material failure across the thickness is likely to occur. Nevertheless existing plate and shell elements ignore the effect of shear deformation in the structure or only account for this phenomenon in an average sense by assuming a uniform shear strain distribution across the thickness. This crude strain field approximation in the presence of high transverse shear forces in the structure could

mislead the analyst to ignore a brittle mode of failure. There are some suggestions to resolve this dilemma: using several layers of three dimensional elements in the thickness direction in the vicinity of high transverse shear zones or utilizing refined plate-shell elements. The latter are extended versions of ordinary plate-shell elements that include more accurate strain fields in the thickness direction.

The other important aspect is the concrete material model. In fact, there is still no universally accepted material model for concrete that covers accurately the wide range of nonlinear behavior of this material. Also it is indisputable that all the material nonlinearities of concrete depend strongly on the tri-axial state of stress. This is specially important in plate and shell structures in the presence of high transverse shear force.

The contribution of out of plane shear forces in plate and shells initiates inclined cracking. The progression of inclined cracking in the region of high transverse shear forces coalesce sometimes into localized fracture zones that lead to brittle modes of failure. To be able to universally capture this mode of behavior, the constitutive relationships of the concrete material model must be able to represent the out of plane and inplane components of stress and strain.

1.3 RESEARCH OBJECTIVES AND SCOPE

The main objective of this study is to improve the accuracy of the finite element method in the analysis of shell structures in zones of high transverse shear forces. This objective is categorized into several sub-domains.

- (1) To develop a new plate shell element with refined strain field to use in the zones of high transverse shear forces.
- (2) To verify the potential of the refined shell elements to represent a more realistic stress-strain field in regions of shell structures dominated by transverse shear.
- (3) To implement a three dimensional plasticity concrete material constitutive relation into the shell finite element.

- (4) To validate the performance of the three dimensional concrete material model in some particular states of stress that exist in plate-shell structures.
- (5) To examine the possibility of introducing the effect of tension stiffening in a three dimensional plasticity material model.

1.4 LAYOUT OF THE THESIS

This thesis consists of six chapters including this introduction as Chapter One. The main concept of each of the following chapters is briefly summarized as follows:

Chapter 2 introduces the new *Refined Degenerated Shell Element*. This chapter starts with an introduction and a short literature review, followed by a discussion of the concept of refinement in degenerated shell elements. The formulation of the new element and the boundary condition of the new degrees of freedom are addressed in the remainder of the chapter.

Chapter 3 presents some examples of the application of refined degenerated shell elements in the zones of high transverse shear force in plate and shell structures. Verification of this new element and comparison of the results with other methods of analysis form the last part of this chapter.

Chapter 4 discusses the concrete material model. Starts with an introduction and a brief literature review, it focuses on the three dimensional fracture energy based plasticity model and its implementation in shell structures. Tension stiffening is also addressed in this chapter. In addition, this chapter provides some examples of the application of this material model in some special states of stress pertinent to plate and shell structures. It gives some insight into the ability of the plasticity model to represent bi-axial tension, pure shear and some other particular states of stress.

Chapter 5 presents attempts at the analysis of plates and shells subjected to high transverse shear forces. It follows with a discussion of the results and some remarks on

the accuracy and reliability of the finite element model in zones of high transverse shear forces.

Chapter 6 summarizes the work and presents a conclusion of the accomplished study.

CHAPTER TWO

REFINED STRAIN FIELD IN THE REGIONS OF HIGH TRANSVERSE SHEAR FORCES *

2.1 Introduction and Literature Survey

The development of plate and shell elements started with elements based on the well known Love-Kirchhoff hypothesis which totally ignores the shear deformation of the element by assuming that a plane cross section that is normal to the mid-surface remains plane and normal to the mid-surface after deformation. Thus, the transverse shear strain is not included in the strain field description of these elements. This strain field consists only of the strain components corresponding to a plane state of stress with a linear variation across the thickness. Figure 2.1 illustrates the deformed side-view of a Love-Kirchhoff plate element and its strain field approximation. Most applications of such elements are restricted to small deformations and are generally plagued by the phenomenon of shear locking at increasing moment gradients. Therefore, using these elements in zones of high transverse shear forces is not recommended because in these regions the shear forces produce a significant out of plane shear strain which cannot be represented by strain field approximations of the Love-Kirchhoff model.

Plate and shell elements based on the Mindlin-Reissner hypothesis (Reissner 1945) were the next development in this area. These elements represent the shear deformation of the structure in an average sense by assuming plane sections remain plane but not necessarily normal to the mid-surface after deformation. Thus, in addition to the in-plane strain components as above this formulation allows a uniform distribution of transverse shear strains across the thickness as shown in Fig. 2.2. A comprehensive overview of the underlying assumptions in the mechanics of shells and also of the discrete finite element models of these structures is given by Wempner (1989).

* This chapter is, in some parts, directly quoted from papers co-written by the author (Ziyacifar and Elwi 1995, 1996-a and b)

Plate and shell elements are traditionally divided into two different groups, shell theory based elements and continuum based elements. The relationship between the two approaches was discussed by Buechter et al. (1992). The advantages of continuum based shell elements are their inherent generality compared to elements based on shell theories. Continuum based shell elements are able to account for all geometric nonlinearities in contrast to the two dimensional states implied in shell theories.

Degenerated shell elements, originally introduced by Ahmad et al. (1968), are formed from three dimensional continuum elements with a special isoparametric interpolation that in effect imposes the same kinematic constraints as those in the Mindlin-Reissner hypothesis. This element is formulated by applying two constraints on the three-dimensional isoparametric brick elements. The first constraint requires that a straight line normal to the mid-surface before deformation remains straight but not necessarily normal to the mid-surface after deformation. The second constraint requires that the extension of the line normal to the mid-surface be negligible, implying the transverse normal strain exists but is condensed out of the formulation, similar to plane stress problems. Because of the three dimensional nature of the formulation the full potential of Lagrangian approach to large deformation can be easily employed. Thus, the formulation allows for all ranges of large deformation and rotations but is restricted to small strains since the thickness cannot change due to the second constraint imposed on the displacement field.

Both of the Mindlin-Reissner and Love-Kirchhoff types of plate and shell elements were extensively used in the analysis of concrete plates and shells by using effective cross sectional properties (EI_{eff}) to account for tensile cracking. This method needs a pre-defined criteria for the value of EI_{eff} based on the propagation of damage in the structure. One of the earliest efforts in this area was reported by Jofriet (1971). Later application of plate-shell elements in the nonlinear analysis of concrete plate and shell structures made use of the layered model of plate-shell elements introduced by Clough (1968). Layered techniques were improved by Figueras et al. (1983), Hinton et al. (1984) and Scordelis et al. (1987). In these versions of shell elements, the element is actually

divided into a number of concrete layers throughout the thickness while the steel reinforcement is smeared into equivalent steel layers with unidirectional properties (Scanlon 1971, Hand et al. 1972 and Lin et al. 1975). With this elaboration, layered elements can represent the state of stress in each layer independently from other layers, allowing for material property variation through the thickness. Therefore, in the compression region of shells or plates, concrete layers might be in elastic, strain hardening or strain softening states while in the tension side concrete layers could be in elastic, or cracked situations. Figure 2.3 shows this element.

Applications of the layered versions of Mindlin-Reissner type of shell elements in the nonlinear analysis of shells and plates is quite common. This application even extends to the regions of high transverse shear forces (Abbasi et al. 1993). The uniform distribution of shear strain across the thickness, although not ideal, is in an average sense a reasonable approximation. Nevertheless, to address zones of high shear forces properly, this approximation is not accurate enough. The assumption of plane cross sections in Mindlin-Reissner hypothesis is not valid in the presence of high transverse shear forces. It leads to a uniform shear strain distribution across the thickness that is not realistic even when the material is elastic. Moreover, it is too far from the true distribution of strain in concrete shells and plates after cracking. Taking into account the fact that in finite element analysis recovery of shear stress is always much poorer than that of normal stress, a more realistic distribution of shear strain is necessary.

The deficiency of layered Mindlin-Reissner elements in these circumstances was addressed by several researchers (Cervera et al. 1987 and Noguchi et al. 1993). As the last alternative they proposed to make use of three dimensional elements in the regions of high transverse shear forces.

Three dimensional elements are ideal elements when the problem is in the three dimensional state of strain. An example of this application was shown by Cervera and Hinton (1986). But in plate and shell structures the neighborhood in which a rigorous three dimensional state of strain exists, is limited only to the zone of high transverse shear

force. In the remaining part of the structure the assumptions utilized in the ordinary plate and shell elements are valid enough to represent the state of strain in the structure.

Using several layers of three dimensional elements in the thickness directions for a large part of the structure is quite expensive in finite element analysis. A remedy to this problem is to use three dimensional elements only in the vicinity of high transverse shear forces and ordinary shell-plate elements in the other parts of the structure. This elaboration needs a transitional element as an interface between the two elements (three dimensional and shell elements). One example of these elements is proposed by Liao et al. (1988). The element called Solid-Shell element and it is in one side a solid element and in the other side a shell element. Figure 2.4 illustrates this element.

Conducting this kind of finite element modelling is not straight forward in many cases. In concrete plates and shells, due to the extension of tensile cracking through most of the thickness, shear rigidity of the cross section becomes small and in the mean time very sensitive to the crack opening displacement or its strain component counterpart (Cedolin et al. 1977, Owen et al. 1984 and Damjanic et al. 1984). As a result, even in the absence of high shear forces there might be some large shear deformations in the structure and refinement of the strain field by three dimensional elements has to be extended further.

An alternative to this approach is to refine the strain field of plate and shell elements. A realistic distribution of shear strain across the thickness requires relaxation of the assumptions utilized in bending hypotheses for plates and shells.

2.1.1 Refined Shell Elements

Refined shell elements relax the constraint that the cross section remains plane after deformation in the Mindlin-Reissner hypothesis. This means that the cross section can warp to comply with a more realistic distribution of strain across the thickness. These kinds of elements are developed based on the so called, higher order theories. For example to represent a parabolic shear strain distribution across the thickness which is the case in elastic structures, a third order variation of inplane displacements is required. This

approach is called third order shear deformation theory (Reddy 1984-a and b). In contrast, the Mindlin-Reissner approach which requires only a linear variation of the inplane displacement across the thickness is called a first order shear deformation theory. Figure 2.5 Shows the inplane displacement across the thickness and its associated strain field for the third order shear deformation theory.

Application of shell elements based on third order shear deformation theories are mostly concentrated on the analysis of composite multi-layered shell structures in aerospace industries. The inter-laminar shear stress and strain is the crucial parameters in the design of these structures and the objective of the refinement is to provide the required insight into this problem. In order to have a continuous shear stress distribution across the thickness, considering different material properties in each layer, a discontinuous shear strain distribution is required (Reddy 1989). This concept is depicted in Fig. 2.6. In concrete shells and plates, however, the refinement objective is different. Initiation of tensile cracking at a point causes reduction of shear rigidity in that part of the cross section (Damjanic et al. 1984) followed by an increase in the normal tensile strain and also transverse shear strain of the cross section at that point. Because of the sensitivity of the shear rigidity to the level of the normal strain after cracking (Owen et al. 1984) estimation of shear deformation of the structure depends on the accuracy of strain approximation. Thus the target in refinement is to simulate the strain field representation of the cross section as closely as possible. It helps to capture the actual behavior of the structure and find out if it is in a brittle or ductile mode. Figure 2.7 shows in-plane and shear strain distributions across the thickness in this situation.

In reinforced concrete structures there are a few examples in which some sort of refinement techniques in shell elements are used in order to solve the problem more accurately. Two examples in this area are the work done by Klein (1986) and Barzegar (1988). Both of them used the layering concept proposed by Mawenya et al. (1974) in which each layer has independent rotational degrees of freedom but the translational degrees of freedom for all layers are connected to each other. Thus it can easily represent

non-symmetrical distributions of shear strain across the thickness in concrete plate and shells after initiation of tensile cracking.

Higher order theories are applied in numerous ways in the refinement of plate and shell elements. These approaches are categorized and discussed by Noor and Burton (1989). Most of these higher order elements were formulated based on the shell theory model. Except for few multi-layered continuum based elements such as the one proposed by Owen et al. (1987) and Li et al. (1989), nothing much has been done to refine the strain field in the continuum based class of elements. In their work a continuum based refined shell element for laminated shells was introduced in which a static condensation technique was used to reduce the computational efforts.

In this thesis the formulation of the continuum based three dimensional degenerated plate-shell element is extended to accommodate the required refinement in the strain field approximation of the element for general applications. The formulation is also extended to the geometrically nonlinear range of behavior using a Lagrangian approach. The refined element is shown to have an adjustable refined strain field suitable for different types of refinement purposes.

2.2 Adjustable Refined Bending Theory for Shells

Based on the shell theory approach a number of refined shell elements have been developed in the last decade. Among those the work by Reddy (1984-a and b) is particularly well known. In his third order theory the constraint that plane cross sections remain plane, which implies a linear variation of the longitudinal displacements through the thickness, is replaced by a third order polynomial defined as:

$$u(z) = u_0 + \alpha z + \beta z^2 + \lambda z^3 \quad (2.1)$$

in which z is the coordinate in the thickness direction, u is the normal displacement of the cross section and α , β and λ are coefficients to be determined. In the case of a symmetric shear strain distribution across the thickness, that is expected with linear isotropic

material models, the term βz^2 automatically disappears. The longitudinal displacement component associated with transverse shear strain is measured from the line normal to the neutral axis as shown in Fig. 2.5 and can be expressed as:

$$u_y(z) = u_0 + (\partial w / \partial x) z - u(z) \quad (2.2)$$

Substituting for $u(z)$ from Eq. 2.1 and taking the derivative of the above equation with respect to z , the shear strain distribution across the thickness is obtained as :

$$\gamma_{xz}(z) = \partial u_y(z) / \partial z = (\partial w / \partial x - \alpha) - 3\lambda z^2 \quad (2.3)$$

Requiring zero transverse shear strain conditions at the top and bottom surfaces yields the longitudinal displacement field across the thickness:

$$u(z) = u_0 + \alpha z + [4(\partial w / \partial x - \alpha) / 3h^2] z^3 \quad (2.4)$$

in which h is the thickness of the structure. The shear strain distribution based on such a displacement field would be a parabola, as shown in Fig. 2.5, which is the ideal case for homogenous elastic material models.

The independent displacement parameters in the case of shell structures considering a two dimensional surface would, thus, be five:

$$u_0, v_0, w_0, \alpha_x \text{ and } \alpha_y$$

These are three translations and two, so called, refined independent variables. Thus, Reddy's approach requires additional independent variables, α_x and α_y , two more than is required by classical shell formulations based on the Love-Kirchhoff hypothesis. In this method, the third term on the right hand side of Eq. 2.4, imposes a strict constraint on the parabolic shear strain distribution and satisfies zero shear strain requirements at the top and bottom surfaces of the element.

Finite element formulations based on such a constraint (third order theory) require a C^1 continuity of the displacement field due to the existence of the partial derivatives of the lateral displacement in the formulation (Eq. 2.4). Similar requirements are existed in the classical shell elements based on the Love-Kirchhoff hypothesis. In this process the partial derivatives of the lateral displacement, w , must be invoked as degrees of freedom in the formulation. In fact for a consistent refined shell element based on third order theory the number of degrees of freedom is eight degree per node. not all independent, however.

$$u_0, v_0, w_0, \alpha_x, \alpha_y, \frac{\partial w}{\partial x}, \frac{\partial w}{\partial y}, \frac{\partial^2 w}{\partial x \partial y}$$

Here the number of independent variables is only five at each node (Reddy 1989 and Averill et al. 1992). In this approach, involvement of the second partial derivative of the first order displacement term, w , represents the continuity of twisting curvature which is numerically inconvenient in finite element method.

Instead of using the above approach, Basar (1993) kept the fourth component of the displacement field in Eq. 2.1 intact, and introduced a new independent variable λ .

$$u(z) = u_0 + \alpha z + \lambda z^3 \quad (2.5)$$

As before, the third component of the displacement field (βz^2) vanishes. In this case the number of independent displacement variables in the shell element becomes seven:

$$u_0, v_0, w_0, \alpha_x, \alpha_y, \lambda_x \text{ and } \lambda_y.$$

This implies that the partial derivative of the displacement, w , in the third order theory is eliminated at the expense of introducing additional independent variables. This also may be viewed as a potential source of problems because a zero transverse shear strain condition at the top and bottom surfaces of the element is not directly required in this formulation. This issue will be addressed later.

Conceptually this approach is similar to the Mindlin-Reissner formulation in which rotation of the cross section is used as an independent variable. This reduces the continuity requirement of the displacement field from C^1 to C^0 and also relaxes the constraint of classical plate theory in which cross sections remain perpendicular to the neutral axes after deformation. Introducing the new independent variables λ_x and λ_y keeps the C^0 continuity in the displacement field while removing the constraint that cross-sections remain plane in the Mindlin-Reissner elements. In the above treatment, the total number of degrees of freedom per node is equal to the number of independent variables, seven per node.

Expressing the longitudinal displacement of the cross section in the form of a third order polynomial allows the cross section to warp in order to comply with the actual strain field in the element. But this is not a general approach to account for all required refinements in shell structures.

2.3 Proposed Refined Strain Field in This Study

In the present study, instead of using a third order polynomial and an independent displacement variable for each of its terms, a shape function attributed to each new independent displacement variable is defined. In this way there is the flexibility to introduce any type of refinement on the displacement field across the thickness, no matter if it is a smooth function such as "z or z³" or a zigzag broken line function as shown in Fig. 2.8. This ability is necessary if a special type of refinement is required. In fact some cases dictate a unique pattern of the displacement field across the thickness that is hard to represent by a polynomial. A laminated plate is an example. In this case a continuous transverse shear stress distribution across the thickness is necessary to keep the equilibrium condition between layers. This requires a discontinuous shear strain distribution because of varying material properties in each layer. Figure 2.6 shows the shape of the longitudinal displacement of the cross section necessary to accommodate such shear strain distribution across the thickness.

Applying the above concept, the longitudinal displacement field throughout the thickness can be represented as:

$$u(z) = u_0 + \alpha f(z) + \beta g(z) + \lambda k(z) + \eta l(z) + \dots \quad (2.6)$$

in which $f(z)$, $g(z)$, $k(z)$, $l(z)$, ... are shape functions and their coefficients α , β , λ , η , ... are independent displacement variables that are similar to the actual degrees of freedom in this approach. Each of these independent variables has two components in the x and y directions. The number of shape functions depends on the complexity of the displacement field. Figure 2.8 illustrates some possible shape functions.

It should be noted that, choosing a shape function must be based on some preliminary knowledge of the displacement field in the structure. Except for the first and second terms which denote translation and ordinary rotations of the middle surface, selection of the other functions is arbitrary as far as the concept of shape function is concerned. In fact, these functions are invoked only to refine the strain field in the structure. When there is no similarity between the strain field in the structure and that represented by a shape function, the independent variable which stands for the coefficient of that shape function (β , λ , η , ...) should assume a near zero value in the analysis process.

2.4 Refined Degenerated Shell Elements

In this section the concept of Adjustable Refined Bending Theory for Shells developed in the previous section is implemented into the degenerated shell elements. Because in this element independent displacement variables for rotations of the cross section are used, the first shape function, $f(z)$, is inherent in the original formulation.

In fact the first shape function is a linear displacement function (i.e. $f(z)=z$) and its independent variable α is simply the angle of rotation of the cross section. In other words to obtain the displacement of a point through the thickness, a simple multiplication of the angle of rotation by the distance from origin, z , is performed. The new independent

variables ($\beta, \lambda, \eta, \dots$) are similar to the rotational degrees of freedom but instead of being multiplied by a linear function z , other types of functions such as $g(z), k(z), l(z), \dots$ are to be used. To highlight this analogy to angles of rotation, these independent variables are, herein, called *generalized rotations*.

The concept of degenerated shell (Ahmad et al. 1968 and Ramm 1976-1977) is based on a three dimensional continuum representation of the strain field in which an isoparametric interpolation imposes kinematic constraints similar to those in the first order shear deformation theory (i.e. Mindlin--Reissner theory). In other words, independent isoparametric interpolation is carried out for translational and rotational degrees of freedom of each node. Figure 2.2 shows the deformed elevation of a degenerated plate-shell element.

Using the same interpolation shape function over the middle surface of the element for all degrees of freedom including generalized rotations, leads to the following displacement field for the element :

$$\begin{Bmatrix} u_1(z) \\ u_2(z) \\ u_3(z) \end{Bmatrix} = \sum_{n=1}^I [N]_n \left\{ \begin{Bmatrix} u_1(0)_n \\ u_2(0)_n \\ u_3(0)_n \end{Bmatrix} + f(z) [F_n(\psi_1, \psi_2)] \begin{Bmatrix} \alpha_{1n} \\ \alpha_{2n} \end{Bmatrix} + g(z) [F_n(\psi_1, \psi_2)] \begin{Bmatrix} \beta_{1n} \\ \beta_{2n} \end{Bmatrix} + \right. \\ \left. k(z) [F_n(\psi_1, \psi_2)] \begin{Bmatrix} \lambda_{1n} \\ \lambda_{2n} \end{Bmatrix} + \dots \right\} \quad (2.7)$$

Here $u_i(0)$ are the displacements of the middle surface. The expression $[F_n(\psi_1, \psi_2)]$ is a 3x2 geometrical transformation matrix proposed by Ramm (1976) to convert the rotation of the cross section to longitudinal displacements. Parameters ψ_1 and ψ_2 are the angles that represent the orientation of the cross section with respect to the global frame of reference. In fact the rotational degrees of freedom α_1 and α_2 are small changes to these angles. The shape of such a transformation depends on the definition of these degrees of freedom and it is similar for all rotational degrees of freedom including generalized rotations. This transformation will be discussed later. The node number n

varies from 1 to l , the number of nodes in an element. and $[N]_n$ is the interpolation sub-matrix at node n . Each shape function in the above formulation (i.e. $g(z)$, $k(z)$,...) can be represented by a simple mathematical expression. The above relationship is merely an extension of the displacement field which was used by Ramm (1976-1977) for ordinary degenerated shell elements. The finite element formulation of the new element is also a modification of the plate shell element published by the same author.

In this work the uniform distribution of out of plane shear strain of the ordinary degenerated plate shell elements is extended to a nonlinear unsymmetric distribution through two additional sets of shape functions. The first shape function, $g(z)$, is provided to represent the parabolic shear strain distribution, yielding zero shear strain at the top and bottom surfaces of the shell. This function is illustrated in Fig. 2.8 and is written as:

$$g(z) = 4z^3 / h^2 \quad (2.8)$$

In the case of anisotropy, elasto-plastic behavior or material models where the behavior in tension is different from that in compression, an unsymmetric shear strain distribution across the thickness may follow. These strain fields can be better represented by introducing more sophisticated shape functions in the same way as above. The second shape function, $k(z)$, is thus, deliberately chosen to introduce an unsymmetric shear strain distribution across the thickness, but in the mean time it should preserve a zero shear strain at the top and bottom fibers of the shell. In this work a **new shape function** is added to the longitudinal displacement distribution across the thickness. This function complies with zero transverse shear strain conditions on the top and bottom surface of the shell and introduces an anti-symmetric distribution of shear strain in the thickness direction. Figure 2.8 shows the desired function and its contribution to the transverse shear strain distribution across the thickness. This new shape function is constructed from spline functions and is written as:

$$k(z) = 6z^2 / h - 8z^3 \text{sign}(z) / h^2 \quad (2.9)$$

At the beginning of loading, while the material is still homogenous elastic, a zero value for the coefficient λ of the function $k(z)$ results which means no unsymmetric shear strain distribution exists across the thickness. When the material in the tension (or compression) side of the plate experiences inelastic softening, the material response to shear deformation is no longer homogeneous across the thickness, which automatically triggers the second component of refinement, $k(z)$. Depending on the severity of softening, the coefficient of this shape function, λ , becomes larger and plays a major role in the displacement field of the element.

It is convenient to give the new displacement shape functions, the same extreme value as that of the rotational degree of freedom at top and bottom of the cross section. This has no effect on the formulation because these additional components will be treated as shape functions. The intention is only to provide the ability to standardize the relative contributions of each component.

The longitudinal displacement at any point on a particular cross section can be written as a function of the local coordinate in the thickness direction, t , as:

$$\begin{aligned} u(t) &= u_0 + u_\alpha(t) + u_\rho(t) + u_\lambda(t) \\ t &= 2z / h \quad -1 \leq t \leq 1. \end{aligned} \quad (2.10-a)$$

in which

$$\begin{aligned} u_\alpha(t) &= \alpha f(t) \\ u_\rho(t) &= \beta g(t) \\ u_\lambda(t) &= \lambda k(t) \end{aligned} \quad (2.10-b)$$

and

$$\begin{aligned} f(t) &= ht / 2 \\ g(t) &= ht^3 / 2 \\ k(t) &= ht^2 / 2 - ht^3 \text{sign}(t) \end{aligned} \quad (2.10-c)$$

Here $f(t)$, $g(t)$ and $k(t)$ are shape functions in the local coordinate.

The concept of shape functions that was used in the above representation can be easily expanded to the other types of refinements in the shell, particularly in multi-layered shell elements. This can be achieved by introducing a piecewise linear shape function across the thickness as a broken line. This function can accommodate the discontinuity of transverse shear strain across the thickness to provide the required continuity of shear force between layers. An example of this function $l(z)$, is depicted in Fig. 2.8. The substitution of such a function instead of $g(t)$ or $k(t)$ does not need any special elaboration in the formulation.

2.4.1 Large Deformation Formulation

In expanding the formulation of the degenerated shell element, the notation used by Ramm (1976 and 1977), is used with minor changes. In the original element the degrees of freedom at each node are three translations ${}^m u_1, {}^m u_2, {}^m u_3$ and two rotations, ${}^m \alpha_1$ and ${}^m \alpha_2$. The translations take place at the middle surface and are defined with respect to the global axes of reference. The rotational degrees of freedom, ${}^m \alpha_1$ and ${}^m \alpha_2$, are defined as changes in the angles, ψ , the normal to the middle surface described with respect to the global frame of reference. Thus, ${}^m \alpha_1$ and ${}^m \alpha_2$ are defined as

$${}^m \alpha_1 = ({}^m \psi_1 - {}^o \psi_1) \quad \text{and} \quad {}^m \alpha_2 = ({}^m \psi_2 - {}^o \psi_2) \quad (2.11)$$

in which $({}^m)$ denotes the current configuration and $({}^o)$ denotes the original undeformed configuration. Figure 2.9 shows the definition of these angles.

The four new degrees of freedom, ${}^m \beta_1, {}^m \beta_2, {}^m \lambda_1$ and ${}^m \lambda_2$ introduced in this work are naturally similar to and are modeled after the rotational degrees of freedom ${}^m \alpha_1$ and ${}^m \alpha_2$. There are, however, two main differences. The new degrees of freedom have zero values in the original configuration (in contrast to the nonzero values of ${}^o \psi_1$ and ${}^o \psi_2$ for rotational degrees of freedom). More importantly, since they have the magnitude of shear strain values, they are not likely to have extremely large values. Therefore, they are treated as small displacement changes. This is in contrast to the contribution of formal

changes in the angles of normal to the middle surface ${}^m\psi_1$ and ${}^m\psi_2$ (or ${}^m\alpha_1$ and ${}^m\alpha_2$), which existed in the original formulation. and can be as large as necessary.

2.4.1.1 Geometric Transformation

Ramm (1976-1977) describes the mapping of a vector of length L along the normal to the middle surface in the current configuration that undergoes small changes in the angle's ${}^m\psi_1$ and ${}^m\psi_2$. The magnitudes of these small changes are α_1 and α_2 . The quantities α_1 and α_2 are thus the incremental changes in angles ${}^m\psi_1$ and ${}^m\psi_2$. The translations of the tip of the vector relative to the global frame of reference are thus:

$$\begin{Bmatrix} \Delta {}^m x_1 \\ \Delta {}^m x_2 \\ \Delta {}^m x_3 \end{Bmatrix} = \begin{bmatrix} 0 & -\sin({}^m\psi_1) \\ -\sin({}^m\psi_1)\sin({}^m\psi_2) & \cos({}^m\psi_1)\cos({}^m\psi_2) \\ \sin({}^m\psi_1)\cos({}^m\psi_2) & \cos({}^m\psi_1)\sin({}^m\psi_2) \end{bmatrix} \begin{Bmatrix} \alpha_1 \\ \alpha_2 \end{Bmatrix} L \quad (2.12-a)$$

$$\{\Delta {}^m x\} = [F({}^m\psi_1, {}^m\psi_2)]\{\alpha\} \quad (\text{symbolically}) \quad (2.12-b)$$

If the changes in the original rotational degrees of freedom are small from one step to the next, the form of Eq. 2.12-b can be used to obtain the corresponding contribution of the new degrees of freedom to the displacement field. The matrix $[F_n(\psi_1, \psi_2)]$ is the transformation matrix introduced in Eq. 2.7.

2.4.1.2 Finite Element Displacement Field

The full large deformation displacement field of a point on the cross section of an element at position t along the normal to the middle surface is described as:

$$\begin{aligned}
\begin{Bmatrix} {}^m u_1(t) \\ {}^m u_2(t) \\ {}^m u_3(t) \end{Bmatrix} &= \begin{Bmatrix} {}^m u_1(0) \\ {}^m u_2(0) \\ {}^m u_3(0) \end{Bmatrix} + \frac{ht}{2} \begin{Bmatrix} \cos({}^m \psi_1) - \cos({}^o \psi_1) \\ \sin({}^m \psi_1) \cos({}^m \psi_2) - \sin({}^o \psi_1) \cos({}^o \psi_2) \\ \sin({}^m \psi_1) \sin({}^m \psi_2) - \sin({}^o \psi_1) \sin({}^o \psi_2) \end{Bmatrix} \\
&+ g(t) [F({}^m \psi_1, {}^m \psi_2)] \begin{Bmatrix} {}^m \beta_1 \\ {}^m \beta_2 \end{Bmatrix} + k(t) [F({}^m \psi_1, {}^m \psi_2)] \begin{Bmatrix} {}^m \lambda_1 \\ {}^m \lambda_2 \end{Bmatrix}
\end{aligned} \quad (2.13)$$

To obtain the increment of displacement field, one notes the corresponding increments in the rotational degrees of freedom are also small enough to be represented by a transformation based on Eq. 2.12-b. If the same interpolation shape functions are used over the middle surface of the element, the incremental displacement field is written in terms of the nodal degrees of freedom as:

$$\begin{Bmatrix} u_1(t) \\ u_2(t) \\ u_3(t) \end{Bmatrix} = \sum_{n=1}^I [N]_n \left\{ \begin{Bmatrix} u_1(0)_n \\ u_2(0)_n \\ u_3(0)_n \end{Bmatrix} + \frac{ht}{2} [F_n({}^m \psi_1, {}^m \psi_2)] \begin{Bmatrix} \alpha_{1n} \\ \alpha_{2n} \end{Bmatrix} + \right. \\
\left. g(t) [F_n({}^m \psi_1, {}^m \psi_2)] \begin{Bmatrix} \beta_{1n} \\ \beta_{2n} \end{Bmatrix} + k(t) [F_n({}^m \psi_1, {}^m \psi_2)] \begin{Bmatrix} \lambda_{1n} \\ \lambda_{2n} \end{Bmatrix} \right\} \quad (2.14)$$

Which is again Eq. 2.7 written in the natural coordinate t .

Here, β_1 , β_2 , λ_1 and λ_2 are increments in the degrees of freedom ${}^m \beta_1$, ${}^m \beta_2$, ${}^m \lambda_1$ and ${}^m \lambda_2$ respectively. The node number n varies from 1 to the total number of nodes in an element, I and $[N]_n$ is the interpolation submatrix at node n .

2.5 Finite Element Formulation

2.5.1 Field Equations

In the following, the element formulation is presented in the context of the incremental principle of virtual work. A Total Lagrangian approach is followed and material nonlinearities are allowed. Assuming that the response is linear in the increment between configurations m and $m+1$, the principle is written as:

$$\int_V e_{ij} C_{ijkl} \delta e_{kl} dV + \int_V {}^m S_{ij} \delta \eta_{ij} dV = \int_A {}^{m+1} t_k \delta u_k dA + \int_V {}^{m+1} f_k \delta u_k dV - \int_V {}^m S_{ij} \delta e_{ij} dV \quad (2.15)$$

Here e is the linear part of the increment of Green Lagrange strain tensor, η is the nonlinear part, S is the second Piola Kirchhoff stress tensor, C is the constitutive tensor, t is the vector of surface tractions and f is the vector of body forces per unit volume. The tensors e and η are defined in terms of the displacement derivatives and its incremental values as:

$$\begin{aligned} e_{ij} &= \frac{1}{2} (u_{i,j} + u_{j,i} + {}^m u_{k,i} u_{k,j} + {}^m u_{k,j} u_{k,i}) \\ \eta_{ij} &= \frac{1}{2} u_{k,i} u_{k,j} \end{aligned} \quad (2.16)$$

At a point within the element defined by ζ and η on the middle surface and t across the thickness, the strain tensor, e , and increment of displacement gradient, $u_{i,j}$, are written in matrix form in terms of the nodal displacement increments as:

$$\{e\} = \sum_{n=1}^l [{}^m B_L]_n \{u_n\} \quad (2.17-a)$$

$$\{\nabla u\} = \sum_{n=1}^l [{}^m B_{NL}]_n \{u_n\} \quad (2.17-b)$$

Here B_L and B_{NL} are shape function derivative operators evaluated at global frame of reference by using a transformation from local coordinate system ζ , η and t .

Substituting the strain tensor, e , and increment of displacement gradient, $u_{i,j}$ in Eq. 2.15 with the forms of Eq. 2.17 and recognizing the arbitrary variation of the displacement increment, the Eq. of equilibrium is recovered as:

$$[{}^m K_L + {}^m K_{NL}] \{u\} = \{ {}^{m+1} R - {}^m Q \} \quad (2.18)$$

in which the first two terms inside the square bracket on the left hand side represent the linear (tangent) and geometric stiffness matrices respectively, while the two terms on the right hand side represent the current level of loads and the internal equilibrating forces. The stiffness matrices and internal force vector are recovered as:

$$\begin{aligned} [{}^m K_L] &= \int_V [{}^m B_L]^T [C] [{}^m B_L] dV \\ [{}^m K_{NL}] &= \int_V [{}^m B_{NL}]^T [{}^m S] [{}^m B_{NL}] dV \\ \{ {}^m Q \} &= \int_V [{}^m B_L]^T \{ {}^m \hat{S} \} dV \end{aligned} \quad (2.19)$$

In the following the forms of the matrices on the right hand side of Eqs. 2.17 and 2.19 are defined.

2.5.2 Derivation of The Strain Displacement Matrix

The third and fourth terms of Eq. 2.16 involve products of the increment of displacement gradient and the displacement gradient tensor in configuration (m). Thus the final representation of strain-displacement derivatives can be written as:

$$\{e\} = [{}^m H] \{\nabla u\} \quad (2.20)$$

in which $[{}^m H]$ contains a template of the current displacement gradient while $\{\nabla u\}$ is the gradient of the increment of displacement. Equation 2.20 in full matrix form would be written as:

$$\begin{Bmatrix} e_{11} \\ e_{22} \\ e_{33} \\ 2e_{12} \\ 2e_{13} \\ 2e_{23} \end{Bmatrix} = \begin{bmatrix} 1+m_{1h,1} & 0 & 0 & m_{1t,1} & 0 & 0 & m_{1b,1} & 0 & 0 \\ 0 & m_{1h,2} & 0 & 0 & 1+m_{1t,2} & 0 & 0 & m_{1b,2} & 0 \\ 0 & 0 & m_{1h,3} & 0 & 0 & m_{1t,3} & 0 & 0 & 1+m_{1b,3} \\ m_{1h,2} & 1+m_{1h,1} & 0 & 1+m_{1t,2} & m_{1t,1} & 0 & m_{1b,2} & m_{1b,1} & 0 \\ m_{1h,3} & 0 & 1+m_{1h,1} & m_{1t,3} & 0 & m_{1t,1} & 1+m_{1b,3} & 0 & m_{1b,1} \\ 0 & m_{1h,3} & m_{1h,2} & 0 & m_{1t,3} & 1+m_{1t,2} & 0 & 1+m_{1b,3} & m_{1b,2} \end{bmatrix} \begin{Bmatrix} 1h,1 \\ 1h,2 \\ 1h,3 \\ 1t,1 \\ 1t,2 \\ 1t,3 \\ 1b,1 \\ 1b,2 \\ 1b,3 \end{Bmatrix} \quad (2.21)$$

Components of the gradient of the increment of displacement vector are obtained using the form of Eq. 2.17-b. Thus, the first step is the calculation of the displacement derivatives matrix $[B_{NL}]$. Displacement derivatives must be first interpolated from nodal degrees of freedom in the natural local coordinate system (ζ, η, t) and then transformed to the global coordinates.

For example, in order to evaluate the gradient of the increment of displacement vector, one must first evaluate the gradient with respect to the local coordinates:

$$\{u_{i,\xi}\}_n = [{}^m N'(\zeta, \eta, t)]_n \{u\}_n \quad i = 1, 2, 3 \quad \text{and} \quad \xi = \zeta, \eta, t \quad (2.22)$$

in which the subscript $(_n)$ denotes the submatrices (vectors) of one node in the element. Here the matrix $[N']$ holds the shape function derivatives with respect to the natural local coordinates of node n evaluated at the current integration point with coordinates ζ, η and t . The vector $\{u\}_n$ holds the displacement increments at node n (remember we have here nine degrees of freedom per node).

The next step is to transform the displacement gradient from the local to the global frame of reference.

$$\{u_{i,j}\} = \sum_{n=1} [J]^{-1} \{u_{i,\xi}\}_n \quad (2.23)$$

In which $[J]^{-1}$ is the inverse of the Jacobian of the geometric transformation. In the “*Total Lagrangian*” approach the Jacobian is derived by interpolating the geometry of the

element from the nodal coordinates in the undeformed configuration. Therefore, the Jacobian remains unchanged in all time steps, because it always refers to the original configuration. But in the “*Updated Lagrangian*” approach, the Jacobian must be derived for each time step on the basis of the displacement field defined in Eq. 2.13.

Combining Eqs. 2.22 and 2.23 and comparing to Eq. 2.17-b the displacement gradient is obtained in the form:

$$\{\nabla u\} = \sum_{n=1}^I [J]^{-1} \left[{}^m N'(\zeta, \eta, t) \right]_n \{u\}_n = \sum_{n=1}^I \left[{}^m B_{NL} \right]_n \{u\}_n \quad (2.24)$$

The vector on the right hand side represents the displacement degrees of freedom of node n , while $\left[{}^m B_{NL} \right]_n$ stands for node n submatrix. The matrix has the form.

$$\left[{}^m B_{NL} \right]_n = \begin{bmatrix} \phi_{\alpha,1}^n & 0 & 0 & \phi_{\alpha,1}^n F_{11}^n & \phi_{\alpha,1}^n F_{12}^n & \phi_{\beta,1}^n F_{11}^n & \phi_{\beta,1}^n F_{12}^n & \phi_{\lambda,1}^n F_{11}^n & \phi_{\lambda,1}^n F_{12}^n \\ 0 & \phi_{\alpha,2}^n & 0 & \phi_{\alpha,2}^n F_{21}^n & \phi_{\alpha,2}^n F_{22}^n & \phi_{\beta,2}^n F_{21}^n & \phi_{\beta,2}^n F_{22}^n & \phi_{\lambda,2}^n F_{21}^n & \phi_{\lambda,2}^n F_{22}^n \\ 0 & 0 & \phi_{\alpha,3}^n & \phi_{\alpha,3}^n F_{31}^n & \phi_{\alpha,3}^n F_{32}^n & \phi_{\beta,3}^n F_{31}^n & \phi_{\beta,3}^n F_{32}^n & \phi_{\lambda,3}^n F_{31}^n & \phi_{\lambda,3}^n F_{32}^n \\ \phi_{\alpha,2}^n & 0 & 0 & \phi_{\alpha,2}^n F_{11}^n & \phi_{\alpha,2}^n F_{12}^n & \phi_{\beta,2}^n F_{11}^n & \phi_{\beta,2}^n F_{12}^n & \phi_{\lambda,2}^n F_{11}^n & \phi_{\lambda,2}^n F_{12}^n \\ 0 & \phi_{\alpha,1}^n & 0 & \phi_{\alpha,1}^n F_{21}^n & \phi_{\alpha,1}^n F_{22}^n & \phi_{\beta,1}^n F_{21}^n & \phi_{\beta,1}^n F_{22}^n & \phi_{\lambda,1}^n F_{21}^n & \phi_{\lambda,1}^n F_{22}^n \\ \phi_{\alpha,3}^n & 0 & 0 & \phi_{\alpha,3}^n F_{11}^n & \phi_{\alpha,3}^n F_{12}^n & \phi_{\beta,3}^n F_{11}^n & \phi_{\beta,3}^n F_{12}^n & \phi_{\lambda,3}^n F_{11}^n & \phi_{\lambda,3}^n F_{12}^n \\ 0 & 0 & \phi_{\alpha,1}^n & \phi_{\alpha,1}^n F_{31}^n & \phi_{\alpha,1}^n F_{32}^n & \phi_{\beta,1}^n F_{31}^n & \phi_{\beta,1}^n F_{32}^n & \phi_{\lambda,1}^n F_{31}^n & \phi_{\lambda,1}^n F_{32}^n \\ 0 & \phi_{\alpha,3}^n & 0 & \phi_{\alpha,3}^n F_{21}^n & \phi_{\alpha,3}^n F_{22}^n & \phi_{\beta,3}^n F_{21}^n & \phi_{\beta,3}^n F_{22}^n & \phi_{\lambda,3}^n F_{21}^n & \phi_{\lambda,3}^n F_{22}^n \\ 0 & 0 & \phi_{\alpha,2}^n & \phi_{\alpha,2}^n F_{31}^n & \phi_{\alpha,2}^n F_{32}^n & \phi_{\beta,2}^n F_{31}^n & \phi_{\beta,2}^n F_{32}^n & \phi_{\lambda,2}^n F_{31}^n & \phi_{\lambda,2}^n F_{32}^n \end{bmatrix} \quad (2.25)$$

In this Matrix F_{ij}^n are the components of the transformation matrix defined in Eq. 2.12, while the shape function derivatives are defined as:

$$\begin{aligned} \phi_{,\xi}^n &= \left[j_{11}^{-1} \phi_{,\xi}^n + j_{12}^{-1} \phi_{,\eta}^n \right] \\ \phi_{\alpha,i}^n &= \left[\frac{h t}{2} \phi_{,i}^n + \frac{h}{2} j_{i3}^{-1} \phi^n \right] \\ \phi_{\beta,i}^n &= \left[g(t) \phi_{,i}^n + g'(t) j_{i3}^{-1} \phi^n \right] \\ \phi_{\lambda,i}^n &= \left[k(t) \phi_{,i}^n + k'(t) j_{i3}^{-1} \phi^n \right] \end{aligned} \quad (2.26-a)$$

In the above expressions the functions $g'(t)$ and $k'(t)$ are simple derivatives of the functions $g(t)$ and $k(t)$ in terms of the natural coordinate t . These shape functions are defined in Eq. 2.10-c. and their derivatives are written as:

$$\begin{aligned} g'(t) &= 3ht^2/2 \\ k'(t) &= 3ht - 3ht^2 \text{sign}(t) \end{aligned} \quad (2.26-b)$$

The strain displacement matrix operator $[{}^m B_L]_n$ is obtained by pre-multiplying matrix $[{}^m B_{NL}]_n$ by $[{}^m H]$ and the strain increment of Eq. 2.17-a is finally obtained as:

$$\{e_{ij}\} = \sum_{n=1}^L [{}^m B_L]_n \{u_n\} = \sum_{n=1}^L [{}^m H] [{}^m B_{NL}]_n \{u_n\} \quad (2.27)$$

The final result is shown on the following page as:

$$\begin{aligned}
& \left[{}^m B_L \right]_n = \begin{bmatrix}
\begin{aligned}
& (1+{}^m u_{1,1})\phi_{,1}^n & {}^m u_{2,1}\phi_{,1}^n & {}^m u_{3,1}\phi_{,1}^n & D_{11}^n\phi_{\alpha,1}^n & D_{21}^n\phi_{\alpha,1}^n & D_{11}^n\phi_{\beta,1}^n & D_{21}^n\phi_{\beta,1}^n & D_{11}^n\phi_{\lambda,1}^n & D_{21}^n\phi_{\lambda,1}^n
\end{aligned} \\
\begin{aligned}
& {}^m u_{1,2}\phi_{,2}^n & (1+{}^m u_{2,2})\phi_{,2}^n & {}^m u_{1,1}\phi_{,2}^n & D_{12}^n\phi_{\alpha,2}^n & D_{22}^n\phi_{\alpha,2}^n & D_{12}^n\phi_{\beta,2}^n & D_{22}^n\phi_{\beta,2}^n & D_{12}^n\phi_{\lambda,2}^n & D_{22}^n\phi_{\lambda,2}^n
\end{aligned} \\
\begin{aligned}
& {}^m u_{1,3}\phi_{,3}^n & {}^m u_{2,3}\phi_{,3}^n & (1+{}^m u_{3,3})\phi_{,3}^n & D_{13}^n\phi_{\alpha,3}^n & D_{23}^n\phi_{\alpha,3}^n & D_{13}^n\phi_{\beta,3}^n & D_{23}^n\phi_{\beta,3}^n & D_{13}^n\phi_{\lambda,3}^n & D_{23}^n\phi_{\lambda,3}^n
\end{aligned} \\
\begin{aligned}
& {}^m u_{1,2}\phi_{,1}^n + (1+{}^m u_{1,1})\phi_{,2}^n & {}^m u_{2,1}\phi_{,2}^n + (1+{}^m u_{2,2})\phi_{,1}^n & {}^m u_{3,2}\phi_{,1}^n + {}^m u_{3,1}\phi_{,2}^n & D_{12}^n\phi_{\alpha,1}^n + D_{11}^n\phi_{\alpha,2}^n & D_{22}^n\phi_{\alpha,1}^n + D_{21}^n\phi_{\alpha,2}^n & D_{12}^n\phi_{\beta,1}^n + D_{11}^n\phi_{\beta,2}^n & D_{22}^n\phi_{\beta,1}^n + D_{21}^n\phi_{\beta,2}^n & D_{12}^n\phi_{\lambda,1}^n + D_{11}^n\phi_{\lambda,2}^n & D_{22}^n\phi_{\lambda,1}^n + D_{21}^n\phi_{\lambda,2}^n
\end{aligned} \\
\begin{aligned}
& {}^m u_{1,3}\phi_{,1}^n + (1+{}^m u_{1,1})\phi_{,3}^n & {}^m u_{2,3}\phi_{,1}^n + {}^m u_{2,1}\phi_{,3}^n & {}^m u_{3,1}\phi_{,3}^n + (1+{}^m u_{3,3})\phi_{,1}^n & D_{13}^n\phi_{\alpha,1}^n + D_{11}^n\phi_{\alpha,3}^n & D_{23}^n\phi_{\alpha,1}^n + D_{21}^n\phi_{\alpha,3}^n & D_{13}^n\phi_{\beta,1}^n + D_{11}^n\phi_{\beta,3}^n & D_{23}^n\phi_{\beta,1}^n + D_{21}^n\phi_{\beta,3}^n & D_{13}^n\phi_{\lambda,1}^n + D_{11}^n\phi_{\lambda,3}^n & D_{23}^n\phi_{\lambda,1}^n + D_{21}^n\phi_{\lambda,3}^n
\end{aligned} \\
\begin{aligned}
& {}^m u_{1,3}\phi_{,2}^n + {}^m u_{1,2}\phi_{,3}^n & {}^m u_{2,3}\phi_{,2}^n + (1+{}^m u_{2,2})\phi_{,3}^n & {}^m u_{2,3}\phi_{,3}^n + (1+{}^m u_{3,3})\phi_{,2}^n & D_{13}^n\phi_{\alpha,2}^n + D_{12}^n\phi_{\alpha,3}^n & D_{23}^n\phi_{\alpha,2}^n + D_{22}^n\phi_{\alpha,3}^n & D_{13}^n\phi_{\beta,2}^n + D_{12}^n\phi_{\beta,3}^n & D_{23}^n\phi_{\beta,2}^n + D_{22}^n\phi_{\beta,3}^n & D_{13}^n\phi_{\lambda,2}^n + D_{12}^n\phi_{\lambda,3}^n & D_{23}^n\phi_{\lambda,2}^n + D_{22}^n\phi_{\lambda,3}^n
\end{aligned}
\end{bmatrix} \quad (2.28)
\end{aligned}$$

The following expressions were used for the sake of simplicity:

$$\begin{aligned}
D_{11}^n &= (1 + {}^m u_{1,1}) F_{11}^n + {}^m u_{2,1} F_{21}^n + {}^m u_{3,1} F_{31}^n \\
D_{21}^n &= (1 + {}^m u_{1,1}) F_{21}^n + {}^m u_{2,1} F_{22}^n + {}^m u_{3,1} F_{32}^n \\
D_{12}^n &= (1 + {}^m u_{2,2}) F_{21}^n + {}^m u_{1,2} F_{11}^n + {}^m u_{3,2} F_{31}^n \\
D_{22}^n &= (1 + {}^m u_{2,2}) F_{22}^n + {}^m u_{1,2} F_{12}^n + {}^m u_{3,2} F_{32}^n \\
D_{13}^n &= (1 + {}^m u_{3,3}) F_{31}^n + {}^m u_{1,3} F_{11}^n + {}^m u_{2,3} F_{21}^n \\
D_{23}^n &= (1 + {}^m u_{3,3}) F_{32}^n + {}^m u_{1,3} F_{12}^n + {}^m u_{2,3} F_{22}^n
\end{aligned} \tag{2.29}$$

The gradient of the total displacement, $\{ {}^m u_{ij} \}$ has yet to be determined. The procedure is similar to that used for the increment of displacement gradient, Eq. 2.24, except that here, possible large values for rotations have to be considered:

$$\{ {}^m u_{i,j} \}_{9 \times 1} = \sum_{n=1}^l [J]^{-1} [{}^m \tilde{N}'(\zeta, \eta, t)]_{9 \times 10}^n \{ {}^m \tilde{u} \}_{10 \times 1}^n = \sum_{n=1}^l [{}^m \tilde{B}_{,NL}]_{9 \times 10}^n \{ {}^m \tilde{u} \}_{10 \times 1}^n \tag{2.30}$$

The dimension of matrices $[{}^m \tilde{N}']$ and $[{}^m \tilde{B}_{,NL}]$ as well as the vector $\{ {}^m \tilde{u} \}$ are slightly different from those used with their counterparts in forming the gradient of the displacement increment in Eq. 2.24 because of the large rotational characteristics of the total displacements. In such a case, due to the complicated trigonometric relationship between the two rotational degrees of freedom ψ_1 and ψ_2 , it is convenient to use three equations for the two degrees of freedom instead of two separate complicated expressions. The detailed description of Eq. 2.30 in matrix form is shown on the next page as:

$$\left\{ \begin{array}{l} {}^m u_{1,1} \\ {}^m u_{2,2} \\ {}^m u_{3,3} \\ {}^m u_{1,2} \\ {}^m u_{2,1} \\ {}^m u_{1,3} \\ {}^m u_{3,1} \\ {}^m u_{2,3} \\ {}^m u_{3,2} \end{array} \right\} = \sum_{n=1}^I \left[\begin{array}{cccccccc} \phi_{\alpha,1}^n & 0 & 0 & \phi_{\alpha,1}^n & 0 & \phi_{\beta,1}^n F_{11}^n & \phi_{\beta,1}^n F_{12}^n & \phi_{\lambda,1}^n F_{11}^n & \phi_{\lambda,1}^n F_{12}^n \\ 0 & \phi_{\alpha,2}^n & 0 & 0 & \phi_{\alpha,2}^n & \phi_{\beta,2}^n F_{21}^n & \phi_{\beta,2}^n F_{22}^n & \phi_{\lambda,2}^n F_{21}^n & \phi_{\lambda,2}^n F_{22}^n \\ 0 & 0 & \phi_{\alpha,3}^n & 0 & \phi_{\alpha,3}^n & \phi_{\beta,3}^n F_{31}^n & \phi_{\beta,3}^n F_{32}^n & \phi_{\lambda,3}^n F_{31}^n & \phi_{\lambda,3}^n F_{32}^n \\ \phi_{\alpha,1}^n & 0 & 0 & \phi_{\alpha,2}^n & 0 & \phi_{\beta,1}^n F_{11}^n & \phi_{\beta,1}^n F_{12}^n & \phi_{\lambda,1}^n F_{11}^n & \phi_{\lambda,1}^n F_{12}^n \\ 0 & \phi_{\alpha,2}^n & 0 & 0 & \phi_{\alpha,2}^n & \phi_{\beta,2}^n F_{21}^n & \phi_{\beta,2}^n F_{22}^n & \phi_{\lambda,2}^n F_{21}^n & \phi_{\lambda,2}^n F_{22}^n \\ \phi_{\alpha,3}^n & 0 & 0 & \phi_{\alpha,3}^n & 0 & \phi_{\beta,3}^n F_{31}^n & \phi_{\beta,3}^n F_{32}^n & \phi_{\lambda,3}^n F_{31}^n & \phi_{\lambda,3}^n F_{32}^n \\ \phi_{\alpha,1}^n & 0 & 0 & \phi_{\alpha,2}^n & 0 & \phi_{\beta,1}^n F_{11}^n & \phi_{\beta,1}^n F_{12}^n & \phi_{\lambda,1}^n F_{11}^n & \phi_{\lambda,1}^n F_{12}^n \\ 0 & 0 & \phi_{\alpha,3}^n & 0 & \phi_{\alpha,3}^n & \phi_{\beta,3}^n F_{31}^n & \phi_{\beta,3}^n F_{32}^n & \phi_{\lambda,3}^n F_{31}^n & \phi_{\lambda,3}^n F_{32}^n \\ 0 & \phi_{\alpha,1}^n & 0 & 0 & \phi_{\alpha,1}^n & \phi_{\beta,1}^n F_{11}^n & \phi_{\beta,1}^n F_{12}^n & \phi_{\lambda,1}^n F_{11}^n & \phi_{\lambda,1}^n F_{12}^n \\ 0 & 0 & 0 & 0 & 0 & \phi_{\beta,2}^n F_{21}^n & \phi_{\beta,2}^n F_{22}^n & \phi_{\lambda,2}^n F_{21}^n & \phi_{\lambda,2}^n F_{22}^n \\ 0 & 0 & 0 & 0 & 0 & \phi_{\beta,3}^n F_{31}^n & \phi_{\beta,3}^n F_{32}^n & \phi_{\lambda,3}^n F_{31}^n & \phi_{\lambda,3}^n F_{32}^n \end{array} \right] \left\{ \begin{array}{l} {}^m u_1^n \\ {}^m u_2^n \\ {}^m u_3^n \\ \cos^m \psi_1^n - \cos^0 \psi_1^n \\ \sin^m \psi_1^n \cos^m \psi_2^n - \sin^0 \psi_1^n \cos^0 \psi_2^n \\ \sin^m \psi_1^n \sin^m \psi_2^n - \sin^0 \psi_1^n \sin^0 \psi_2^n \\ {}^m \beta_1 \\ {}^m \beta_2 \\ {}^m \lambda_1 \\ {}^m \lambda_2 \end{array} \right\} \quad (2.31)$$

2.5.3 Stress State Matrix and Vector $[{}^mS]$ and $\{{}^m\hat{S}\}$

There are only six components of stress state all together, but to comply with matrix multiplication requirements, they have to be manipulated into a square matrix form:

$$[{}^mS] = \begin{bmatrix} {}^mS_{11} & 0 & 0 & 0 & 0 & 0 \\ 0 & {}^mS_{22} & 0 & 0 & 0 & 0 \\ 0 & 0 & {}^mS_{33} & 0 & 0 & 0 \\ {}^mS_{12} & 0 & 0 & {}^mS_{22} & 0 & 0 \\ 0 & {}^mS_{21} & 0 & 0 & {}^mS_{11} & 0 \\ {}^mS_{13} & 0 & 0 & {}^mS_{23} & 0 & {}^mS_{33} \\ 0 & 0 & {}^mS_{31} & 0 & 0 & 0 \\ 0 & {}^mS_{23} & 0 & 0 & {}^mS_{13} & 0 \\ 0 & 0 & {}^mS_{32} & 0 & 0 & 0 \\ 0 & 0 & 0 & {}^mS_{12} & 0 & {}^mS_{22} \end{bmatrix} \quad (2.32)$$

The stress state vector $\{{}^m\hat{S}\}$, takes the traditional form:

$$\{{}^m\hat{S}\}^T = \langle {}^mS_{11} \quad {}^mS_{22} \quad {}^mS_{33} \quad {}^mS_{12} \quad {}^mS_{13} \quad {}^mS_{23} \rangle \quad (2.33)$$

2.6 Boundary Conditions

Boundary conditions are constraints on certain force or displacement components. Simple constraints take the form of prescribed displacements or forces. The new degrees of freedom introduced herein cannot have nonzero prescribed displacements or forces. Thus the associated nodal forces for these degrees of freedom are always zero, regardless of the loading condition on the structure. The major concern herein, is to determine, for different cases, whether to suppress these degrees of freedom at certain locations.

In the presence of transverse shear forces, the third displacement component in Eq. 2.10-a, $u_\beta(t)$, is directly proportional to the shear strain at the neutral axis, β_θ . This component and its associated shear strain distribution are included in Fig. 2.10. The second component of displacement in Eq. 2.10-a is representative of the rotational degree of freedom. Its derivative in the longitudinal direction provides the normal flexural

stresses associated with bending moments also its derivative in the thickness direction provides a constant shear strain contribution. The shape of the full shear strain distribution is a combination of the two contributions and is depicted in Fig 2.10.

It is noted here that there is no strict constraint that imposes a perfect parabolic restraint on the shear strain distribution across the thickness, similar to that in the third order shear deformation theory. Since each component of longitudinal displacement across the thickness having a contribution to the out of plane shear strain distribution is a totally independent degree of freedom, there is no assurance of a zero shear strain at the top and bottom fibers. Everything is relegated to the self adjustment capability of the finite element formulation. On the basis of the field described in Eq. 2.10-a. the structure has two different channels to move into, second and third component of displacement $u_\alpha(t)$ and $u_\beta(t)$, for the case of a symmetric distribution of shear strain. Its share from each of those, is inherited from the basic concept of finite element. In other words, the structure would choose a combination from both of those channels of deformations in which the resulting strain distribution satisfies equilibrium and simulates the actual strain field. Moreover, the new components contribute to the longitudinal normal strains as well as the transverse shear strains.

The new refined degrees of freedom also interact with ordinary degrees of freedom. The parabolic shear degrees of freedom β_1 and β_2 not only contribute to the shear strain distributions, but also to the rotations and, thus, indirectly to the bending moment field. Therefore, an interaction with the rotational degrees of freedom α_1 and α_2 would be expected. Similarly, the unsymmetric shear degrees of freedom λ_1 and λ_2 interact with the axial deformations. As a starting point it would be necessary to switch off the interaction phenomena at certain points to avoid undesirable strain fields.

The parabolic shear strain degrees of freedom β_1 and β_2 are similar to rotational degrees of freedom. Thus, if a fixed rotational boundary condition is required, these degrees of freedom should be suppressed along with the ordinary rotational degrees of freedom α_1 and α_2 . The same reasoning, however, cannot be used for the unsymmetric

shear strain degrees of freedom λ_1 and λ_2 . Although the latter degrees of freedom can represent axial deformations as well as unsymmetric shear strain distributions, the middle surface of the element is not affected by these degrees of freedom. Thus, there is no need to suppress these degrees of freedom where the axial in-plane degrees of are suppressed.

The unsymmetric shear strain distribution is represented by the function $k(t)$ in Eq. 2.10-c. This shape function is symmetric and possesses a derivative with respect to the longitudinal coordinates that is also symmetric about the middle surface. Thus, it has no contribution to the flexural deformation of the cross section. On the other hand, close attention must be paid to its contribution to the axial deformation of the element, which is normally represented only by the translational degree of freedom u_n . This contribution is particularly pronounced at discontinuity locations of axial forces such as inplane point loads and support reactions.

Where a concentrated load is applied in the in-plane direction, the unsymmetric shear strain degrees of freedom λ_1 and λ_2 together with ordinary in-plane degrees of freedom u_1 , u_2 and u_3 can represent the pinching effect on the middle surface of the cross section. Thus, point load location might be a potential source of undesired pinching effect in structure. With no constraints on the λ degrees of freedom, a concentrated load that is assumed to be applied at the middle surface is distributed non-uniformly on the cross section. Therefore, the λ degrees of freedom must be restricted where a concentrated load on the in-plane direction is expected on the structure. Support reactions with components in the in-plane direction are an example of this case. A node at which a concentrated load is applied with a component in the in-plane direction, is another potential candidate for restricting these degrees of freedom. On the other hand, suppressing this degree of freedom removes one of the most desirable aspects of refinement in the shell element. Therefore, it should be done only at the nodes at which a high magnitude of concentrated in-plane force is expected.

The same phenomenon arises in the case of concentrated moments. In this situation there is strong interaction between the α and β degrees of freedom. Therefore,

the contribution of β to the final strain distribution across the thickness may not be proportional to the actual shear force. In this case the strain field may no longer be acceptable. A remedy for this problem is to suppress the parabolic shear strain distribution degrees of freedom at the point of concentrated moment. Again, one should keep in mind that this solution eliminates the contribution of refinement on parabolic shear strain distribution. Thus, it is advisable only in the presence of high concentrated moments.

There is another way to switch off the interaction between the new degrees of freedom and the original translational and rotational degrees of freedom based on changing the definition of the shape functions. For instance in the case of λ degrees of freedom, if the definition of shape function $k(z)$ could change so that, its integral across the thickness become zero (from $z = -h/2$ to $z = +h/2$), it can no longer have any contribution to the inplane displacement of the cross section. Such a function can easily be found by shifting the function $k(z)$ in Fig. 2.8-a. to the left side of the z axis. For β degrees of freedom, however, the first moment of the function $g(z)$ about an axis parallel to the neutral surface must be zero to remove its interaction with the rotational degrees of freedom.

2.7 Programming

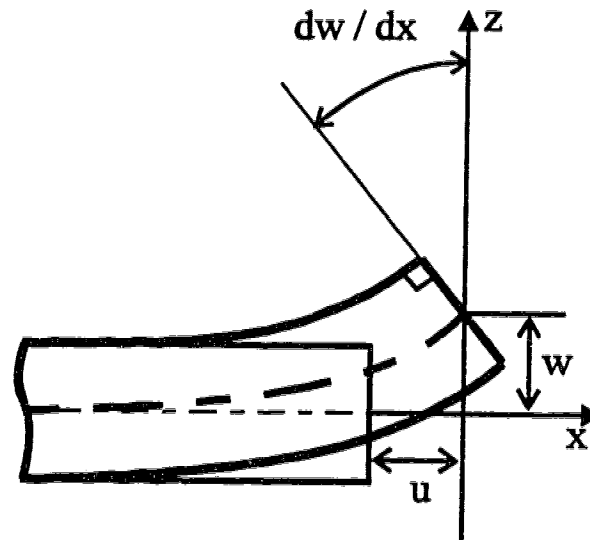
The model developed above was implemented into Program NISA-80 that was developed at the University of Stuttgart by Stegmüller et al. (1983). This program was written in FORTRAN77 and contains the three dimensional degenerated plate-shell elements developed by Ramm (1976-1977). The total number of lines added to this program to accommodate two sets of refined shape functions is less than 500.

Because of the similarity between the new degrees of freedom (or independent variables) and existing rotational degrees of freedom, the programming of the new shell element becomes easy. Besides, the computer program would be quite flexible because no matter what kind of shape function to be used, the program can accept or replace them

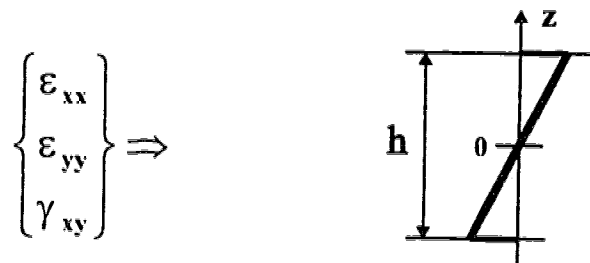
in an orderly manner without any special elaboration. The number of shape functions which can be used is not limited, but to reduce the computational effort it is preferred to employ only those functions which are likely to be effective in refinement of the strain field in the structure.

It should be noted that for each across-the-thickness shape function, one degree of freedom is added in each direction at each node. Thus, for the parabolic and anti-symmetric shear distributions, two additional degrees of freedom in each direction must be added to the ordinary five degrees of freedom at each node. The increase in computational effort is thus substantial. The use of the additional degrees of freedom should be based on the specific characteristics of each problem. For example if there is no possibility of having an unsymmetric behavior in the shell thickness, it is better to suppress the degrees of freedom related to this behavior in the finite element model or even remove the corresponding shape function from the formulation.

To implement any other types of refinement in the shell structure, the same computer program which was used for diffused material failure herein, can be employed without any special treatment. The only changes would be in the definition of $k(t)$ and/or $g(t)$ which must be written in a small separate subroutine and linked to the main program.

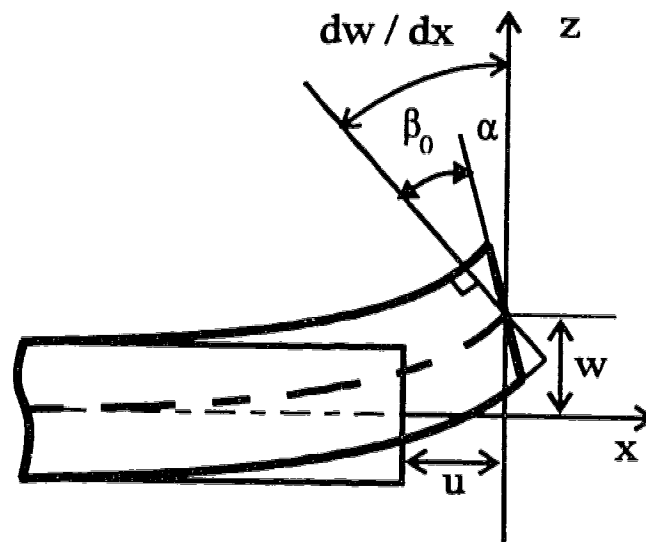


(a) - Deformed elevation

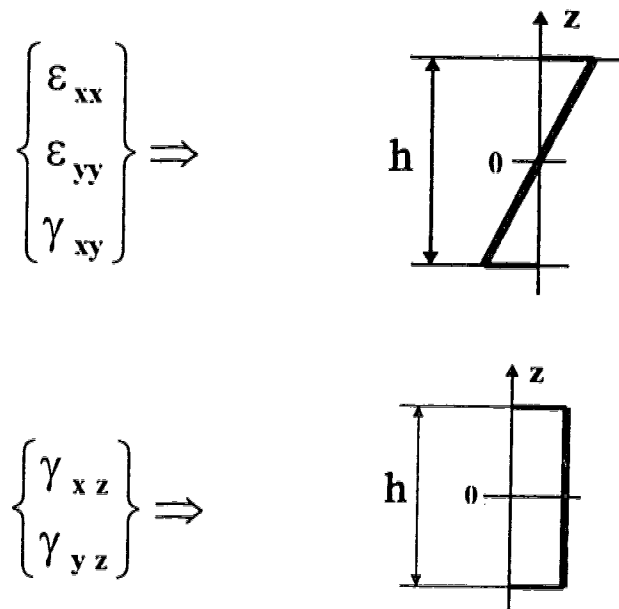


(b) - Strain distribution across the thickness

Figure 2.1 - Love-Kirchhoff hypothesis on bending

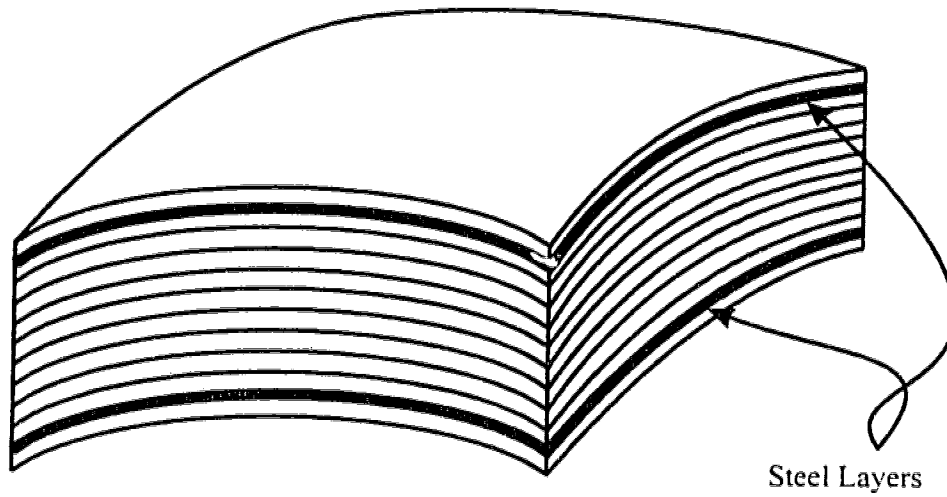


(a) - Deformed elevation

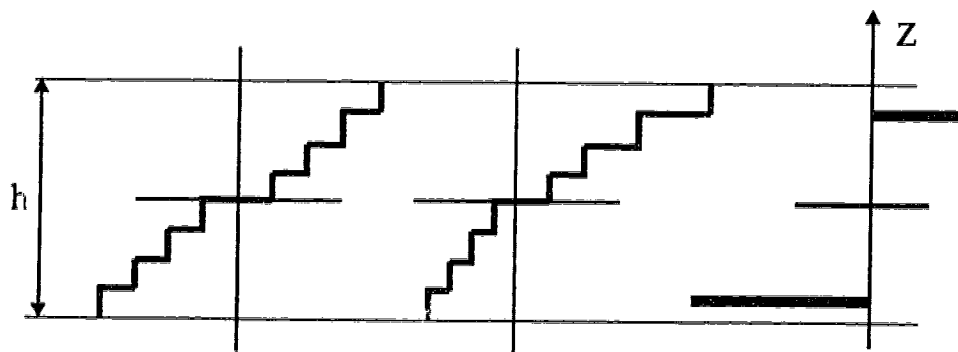


(b) - Strain distribution across the thickness

Figure 2.2 - Mindlin-Reissner hypothesis on bending



(a) - Layered shell element



(b) - Normal strain (c) - Stress in concrete (d) - Stress in steel

Figure 2.3 - Layered shell element

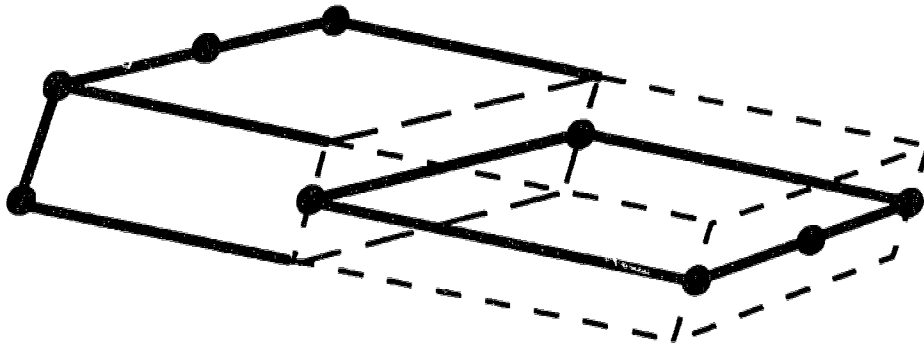
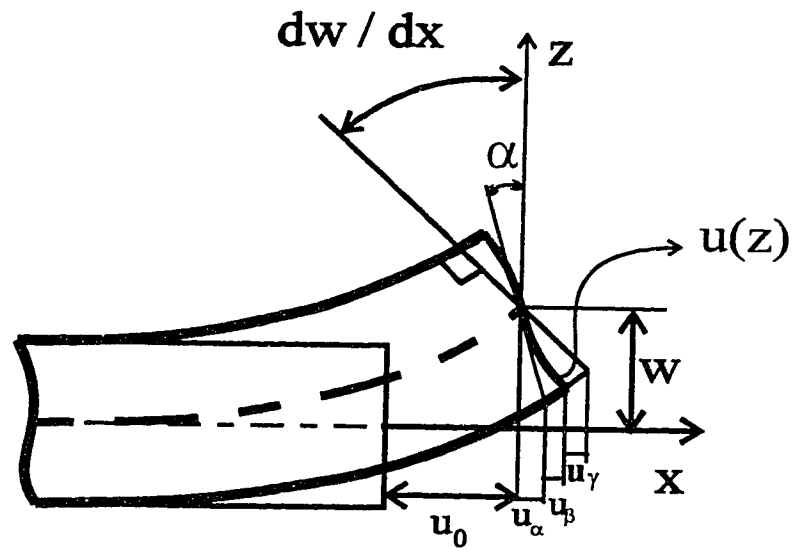


Figure 2.4 - Solid-shell element



(a) - Deformed elevation

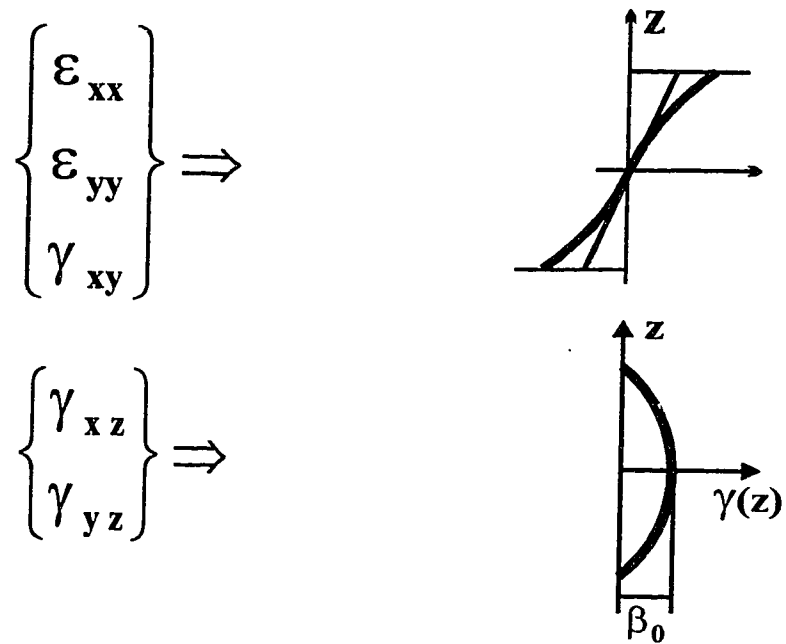
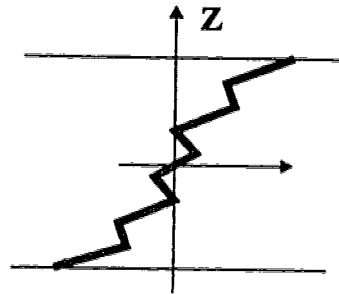
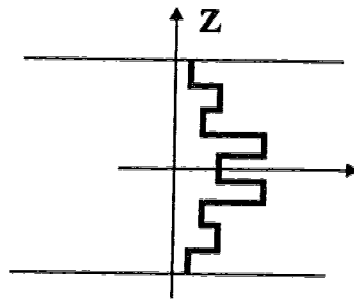


Figure 2.5 - Third order deformation theory

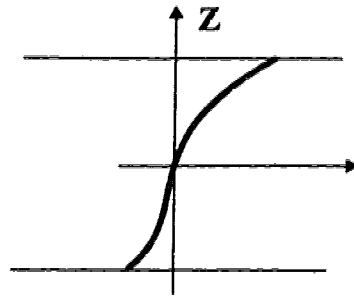


(a) - Displacement across the thickness

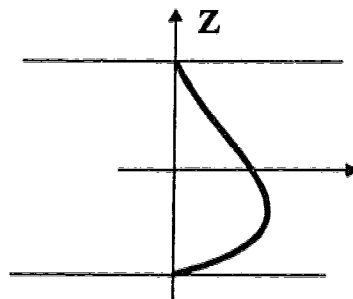


(b) - Discontinuous shear strain across the thickness

Figure 2.6 - Multi-layered shell

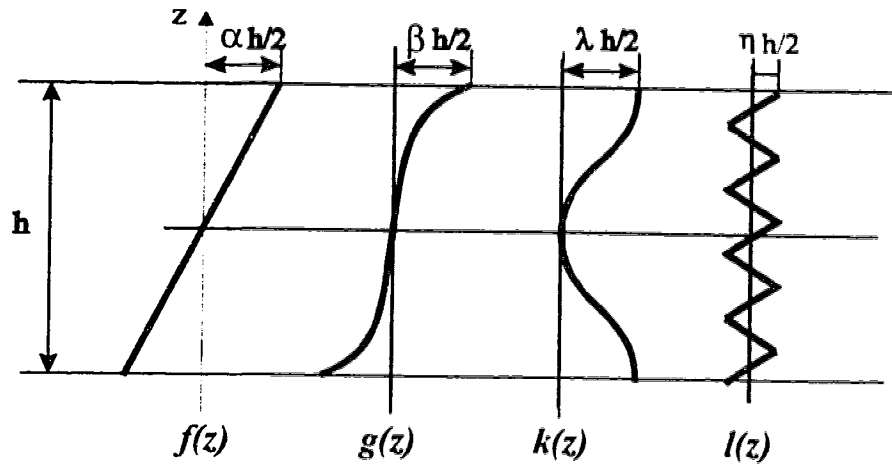


(a) - Inplane strain distribution across the thickness

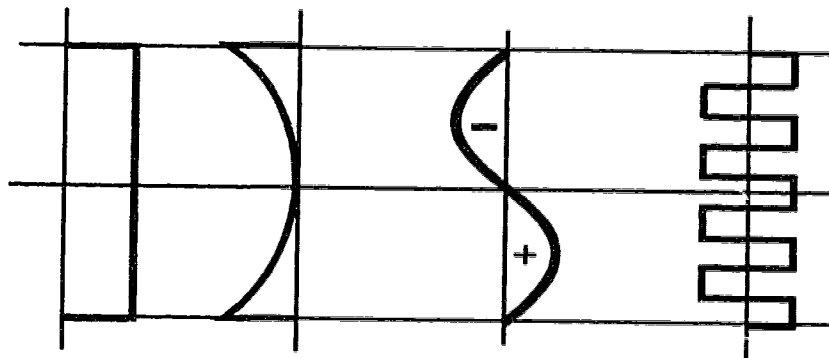


(b) - Shear strain distribution across the thickness

Figure 2.7 - Strain distribution in the case of diffused material failure



(a) - Shape functions for cross section displacement



(b) - Shear strain contribution of the shape functions

Figure 2.8 - Shape function across the thickness

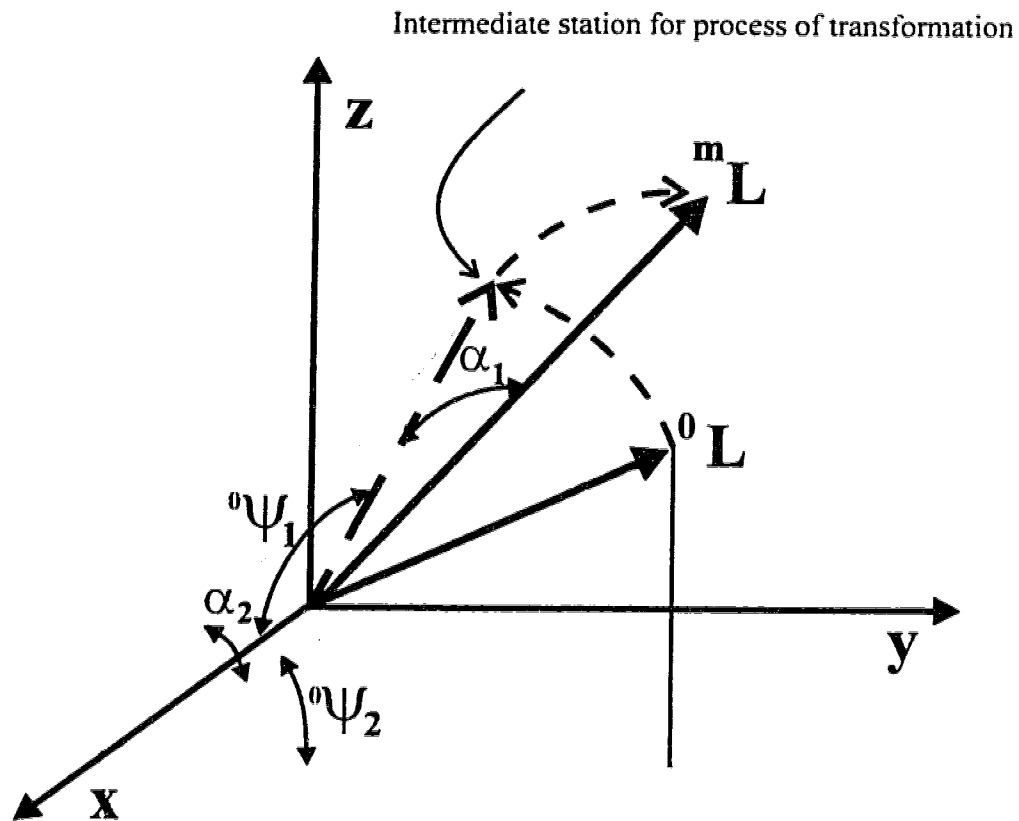


Figure 2.9 - Definition of rotational degrees of freedom

Note:

- ψ_1 is the angle between normal to middle surface L and x -axis
- ψ_2 is the angle between the x - L plane and x - y plane
- α_1 is the changes in ψ_1
- α_2 is the changes in ψ_2

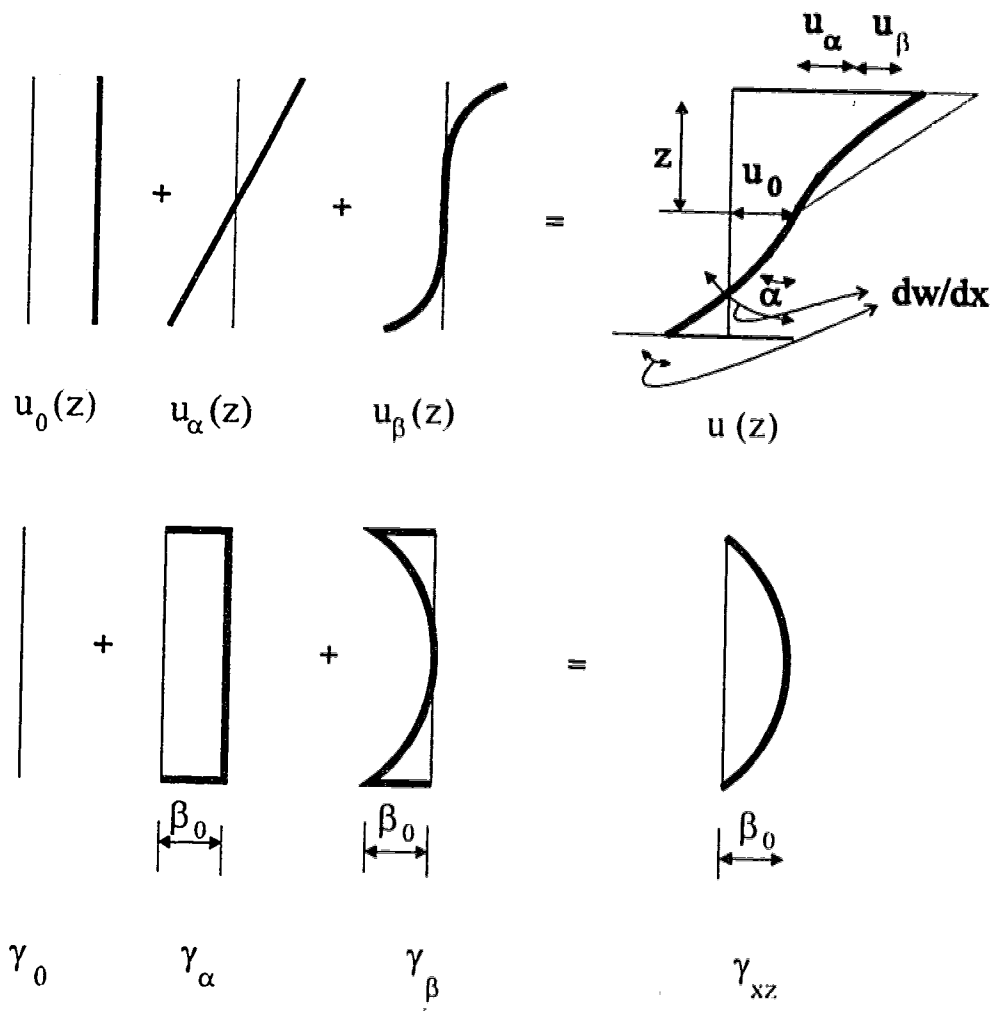


Figure 2.10 - Displacement and shear strain distribution across the thickness

CHAPTER THREE

VERIFICATION OF THE REFINED ELEMENT

3.1 Introduction

In order to verify the performance of the refined element, a number of problems were solved and the solutions compared to those obtained from the original degenerated plate-shell element, hereinafter called the “ordinary element”, and other solutions. The examples include a shell structure, two square plates and two beams. The integration algorithm adopted in all the examples in this chapter and the rest of this study is a full Gaussian integration (4x4 integration points for bi-cubic elements used in this study) in the plane parallel to the surface. Though sometimes it is not really necessary, an eleven point Simpson’s integration rule is adopted across the thickness for all the examples. In the following the examples are presented and the results discussed.

3.1. Elastic Behavior of Thin and Thick Shells

The first example is a shallow spherical shell supported on four corners and subjected to a uniform normal pressure loading. The material property is assumed to be isotropic linear elastic. The consequences of using the refined element are manifested in the flexibility of the structure and the stress distribution. Both effects are thickness dependent. Therefore, this example has been solved with two thickness units ($t=200$ and 2000 mm). The extreme thickness values have been used deliberately to bring out an exaggerated response that can be seen clearly.

Figure 3.1 shows the load versus vertical deflection response of point B for both the ordinary element and the refined element in the case of the thin shell ($t=200$. mm). The two solutions are almost identical, but the one with refined elements is slightly more flexible than the other one. This flexibility which might not be seen in that figure due to

its small scale, comes from the higher number of degrees of freedom in the refined model.

Figure 3.2 illustrates the normal and shear stress distributions at point A that is close to a support. Note that the difference in the normal stress distribution between the solutions of the ordinary element and the refined element is clear and in contrast to the shear stress distribution, is highly thickness dependent as is shown in Fig. 3.3 for the case of the thick shell structure ($t=2000$ mm). This is expected since plane sections do not remain plane in the presence of high shear gradients in the refined element. The ratio of the shear stresses to the normal stresses in the thick shell at this location is much higher than that in the thin shell at the same location.

3.2. Elastic-Plastic Analysis of a Plate

The next example consists of a square plate supported at four corners and subjected to a uniform pressure. The material has a yield strength of 240 MPa and is modeled with an elastic perfectly plastic Von Mises constitutive relation. The response of the refined element shows a different progression of yield in the structure from that of the ordinary element. The refined element predicts yield in the structure earlier and also in a different mode compared to the ordinary element. The onset of yield takes place at the middle of the cross section close to the support (point A in Fig. 3.4-a) due to the high shear stresses at that point (Fig. 3.4-b). This limits the load carrying capacity of the structure and constitutes a behavior approaching "punching" shear failure. On the other hand, when ordinary elements are used, the onset of yield is postponed to a higher level of load and it starts at the extreme fibers of the plate cross section due to a combination of out-of-plane shear stresses and in-plane normal and shear stresses. The structure then exhibits a gradually softening response. Punching shear may not be detected if a different mode of failure takes place elsewhere, such as at mid-span or at the free edge. The load deflection curve is shown in Fig. 3.5.

3.3. Plate with Unsymmetric Material Behavior Across the Thickness

The next example shows the case of unsymmetric material behavior across the thickness. This is provided by applying a bi-axial inplane normal force to a square plate supported at the central point. This represents the region of a flat slab around a column. The plate is subjected to a uniform transverse pressure. The vertical displacement of the four corners have been constrained to be equal by a boundary equation (an option in program NISA), to prevent rigid body modes of behavior in the structure. The material model used here is the same as that of the previous model. In this case, the onset of yield in the top and bottom fibers of the plate, takes place at different levels of transverse pressure. Figure 3.6 shows the normal and shear stress distributions at point *A* that clearly depicts the effect of the unsymmetric component of shear strain across the thickness.

3.4. Strain Distribution Close to the Point of Discontinuity of Shear Force

As mentioned in the previous chapter, both the parabolic shear strain components, β , and the rotational degrees of freedom, α , contribute to the shear and flexure deformation modes simultaneously. At a discontinuity in the transverse shear forces a combination of α and β could yield a non-zero transverse shear strain at the top and bottom of the plate surface. However, the integral of shear stresses across the thickness is always in total balance with the actual shear force on the cross section.

Under such circumstances the C^0 continuity of the interpolation functions for refined degrees of freedom, β , between elements (and higher orders of continuity for the nodes inside the element) exists. This does not allow the finite element model to imitate the discontinuity in the shear force properly. In this situation a combination of the degrees of freedom α and β gives a gradual but steep transition of shear strains over the discontinuity region. If a three dimensional model were to be used with the same constraints of plate or shell, the result of the strain field would be similar to that of the refined shell element. This phenomenon is illustrated in the last example.

In this last example, a beam supported at both ends and subjected to concentrated loads is analyzed. The beam is fairly thick to render the shear deformation mode dominant relative to the flexural mode. Two extreme cases in which a sharp discontinuity in the shear force exists in the beam are analyzed, one with two point loads applied at $L/4$ points of the span and one with a single mid-span load. These beams are shown in Fig. 3.7. Boundary conditions of plane stress are assumed in the width direction when refined elements are used (12 bi-cubic elements). The same beams were constructed from 256 two dimensional isoparametric 8-node plane stress elements also shown on the same figure. The large number of elements is necessary to examine the stress points as close as possible to the plane of shear force discontinuity. Figure 3.8-a shows the results for the mid-span load case compared to the plane stress solution at different points in the vicinity of the discontinuity. At points close to the discontinuity (for example at $L/290$ away from the discontinuity), the shear stress distributions from the plane stress and from the refined element solutions are rather flat. A short distance away from the point of discontinuity ($L/14$) both solutions become much more parabolic.

Figure 3.8-b shows the two point load solutions for both types of analysis. The points at $L/290$ and $L/14$ are in the pure moment region. However because of localized effects both solutions give a perturbation in the shear stress that is evident at $L/290$ and is negligible at $L/14$ from the load point in this region. The solutions at a distance of $L/40$ from the load point measured towards the support (nonzero shear force zone) are again almost identical and parabolic.

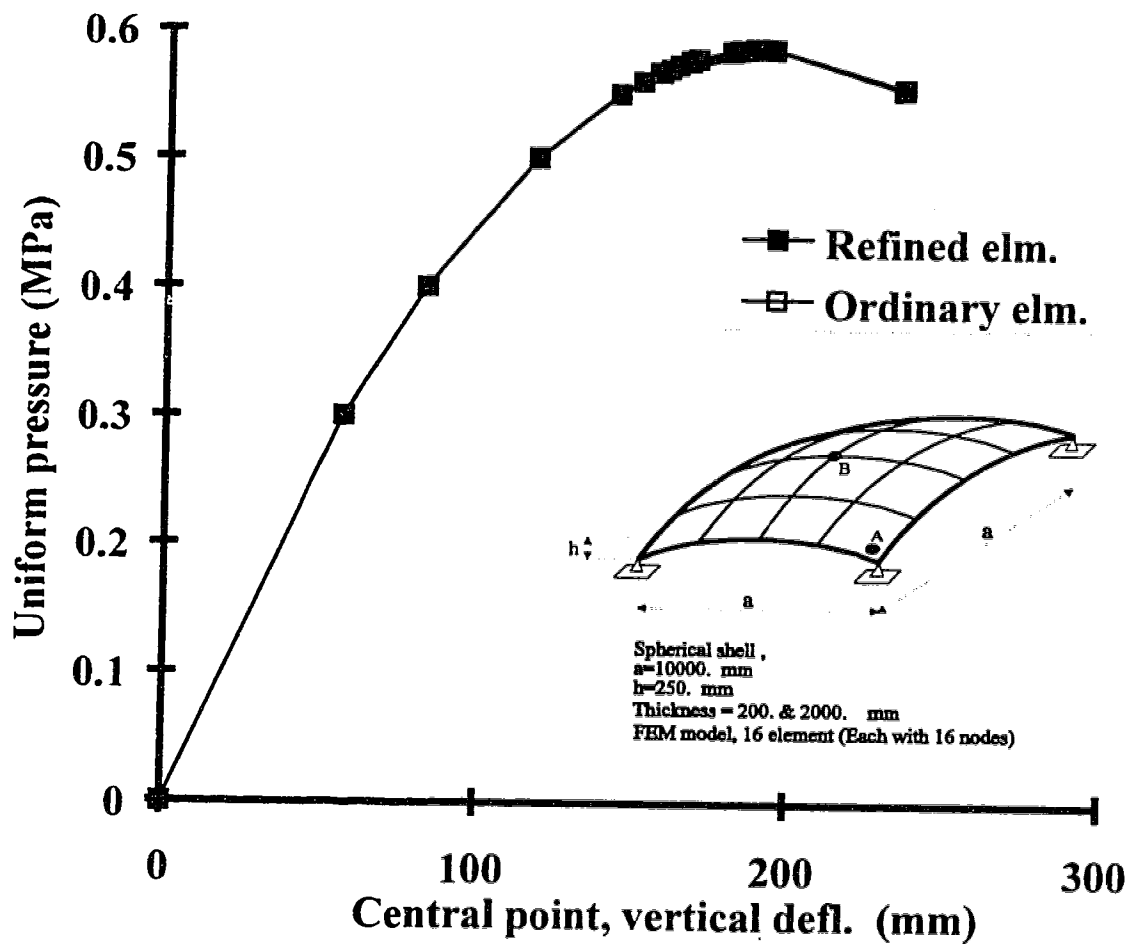


Figure 3.1 - Thin shell example, vertical deflection of central point

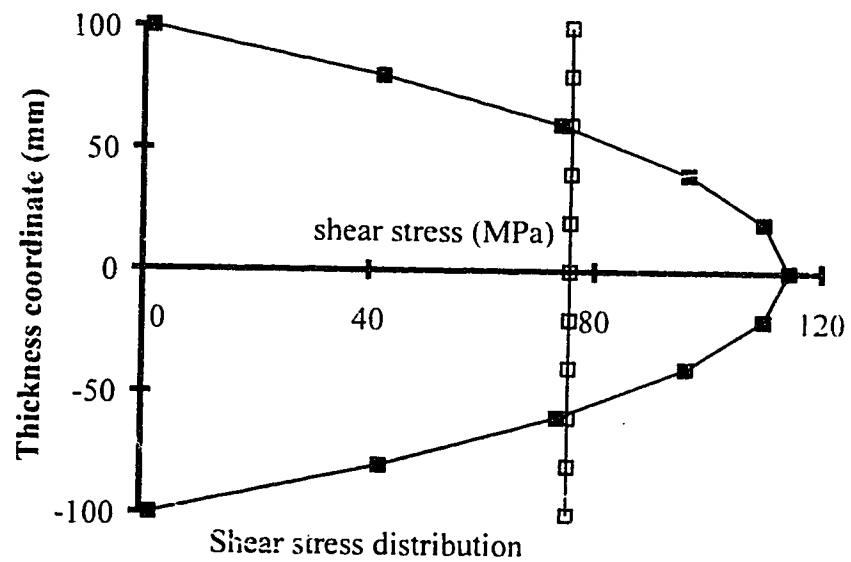
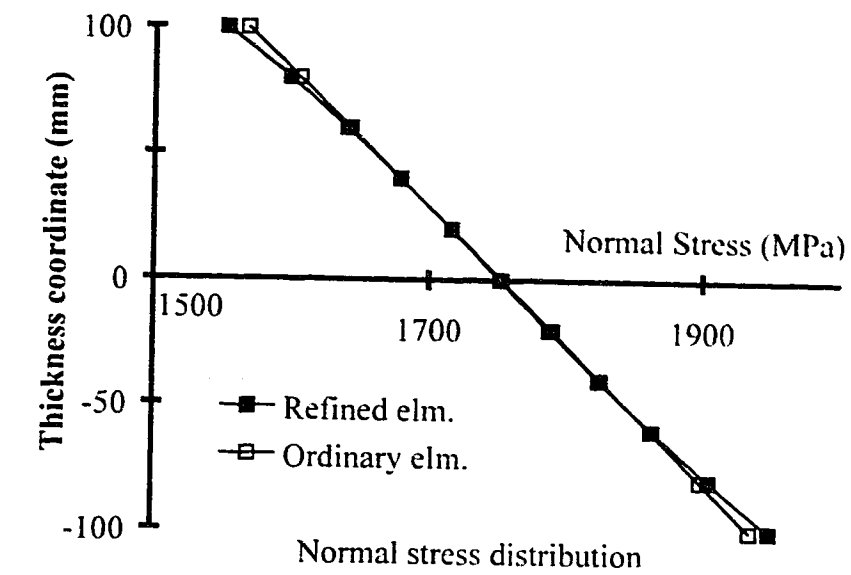


Figure 3.2 - Thin shell example, stress distribution at point A

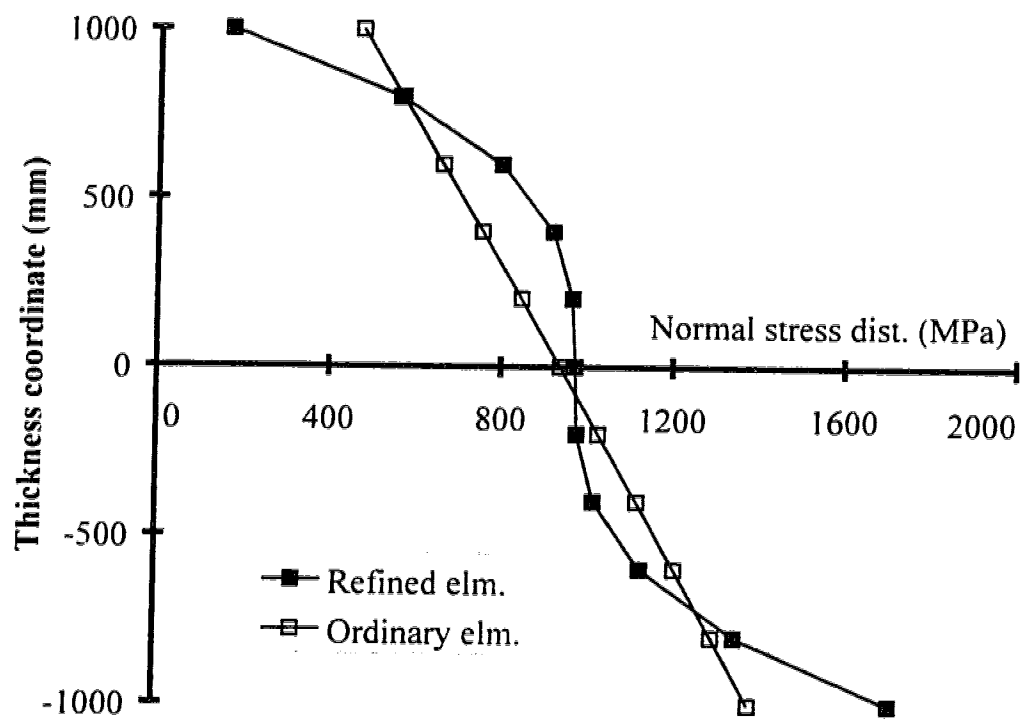


Figure 3.3 - Thick shell example, normal stress distribution at point A

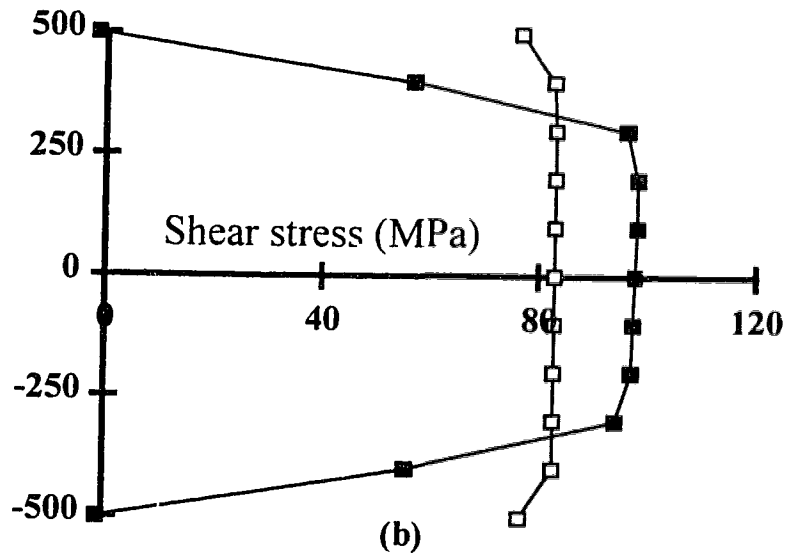
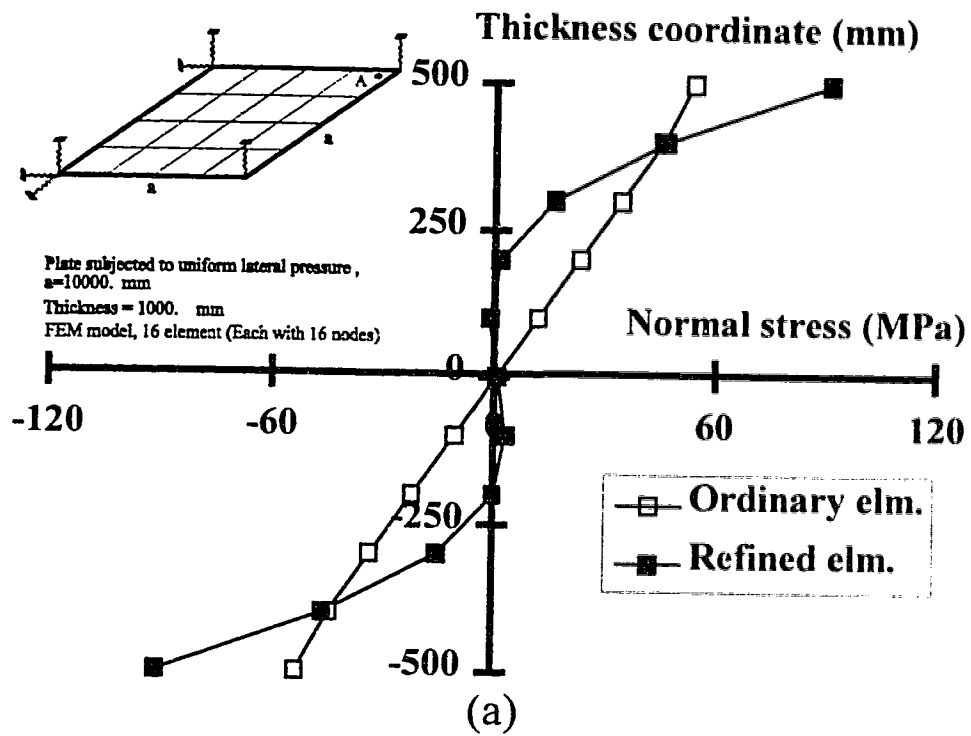


Figure 3.4 - Plate supported at corners, stress distribution at point A

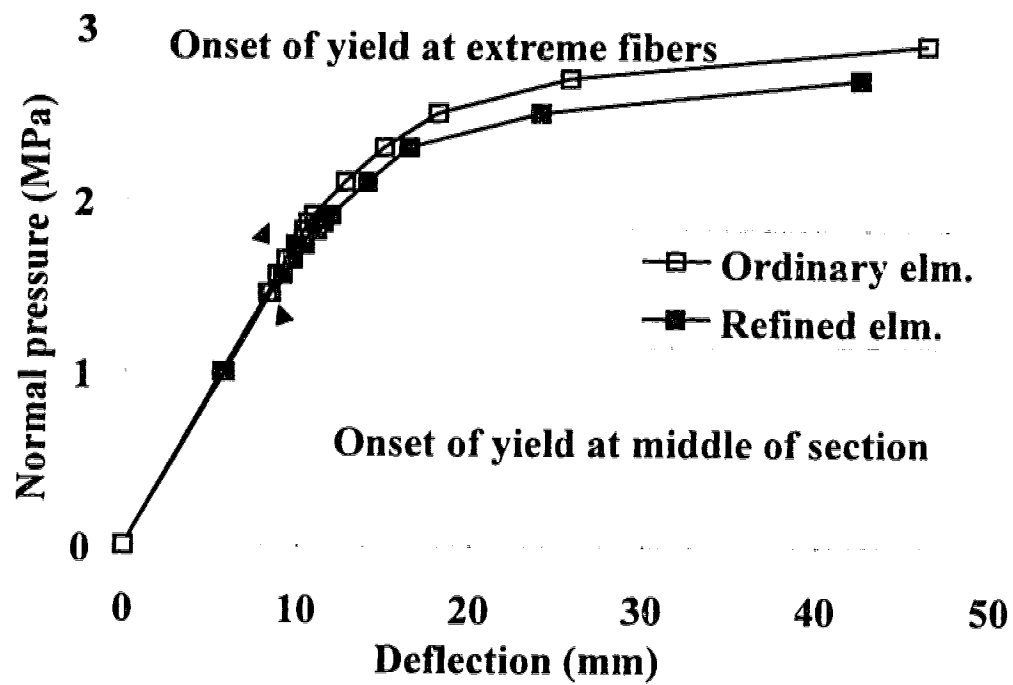
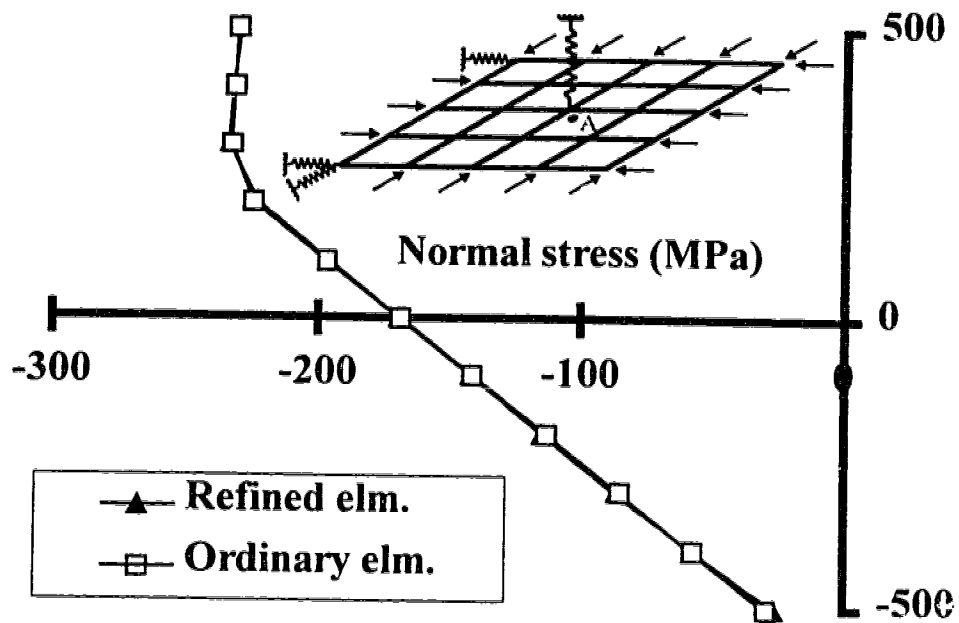
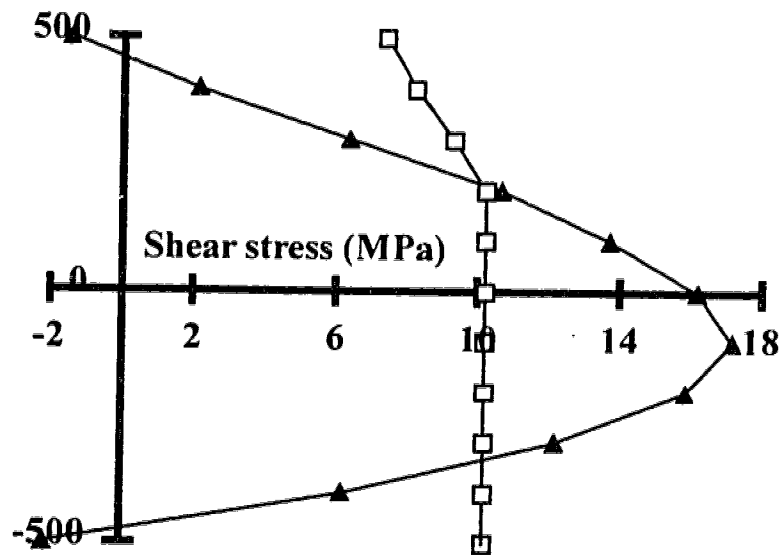


Figure 3.5 - Plate supported at corners, vertical deflection at point A

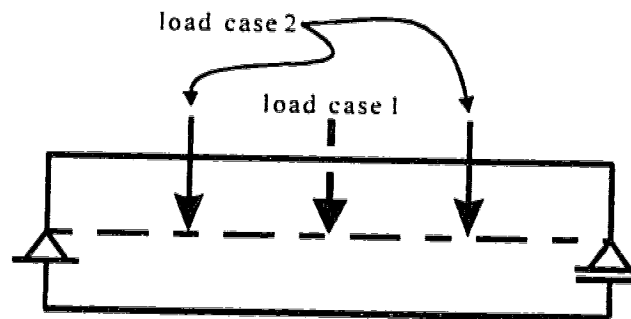


(a) - Normal Stresses



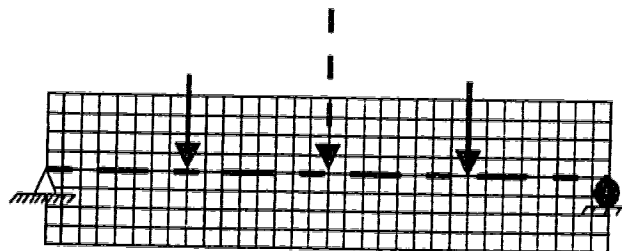
(b) - Shear stresses

Figure 3.6 - Plate supported at centre, stress distribution at point A



Load case 1; loading at mid-span

Load case 2; loading at 1/4 of span



FEM model, 256 plane stress element

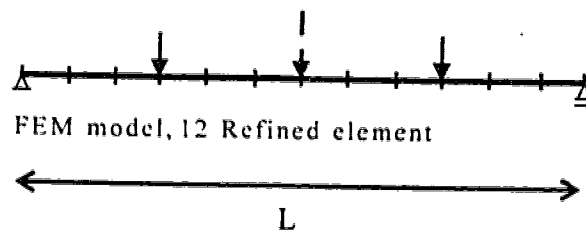
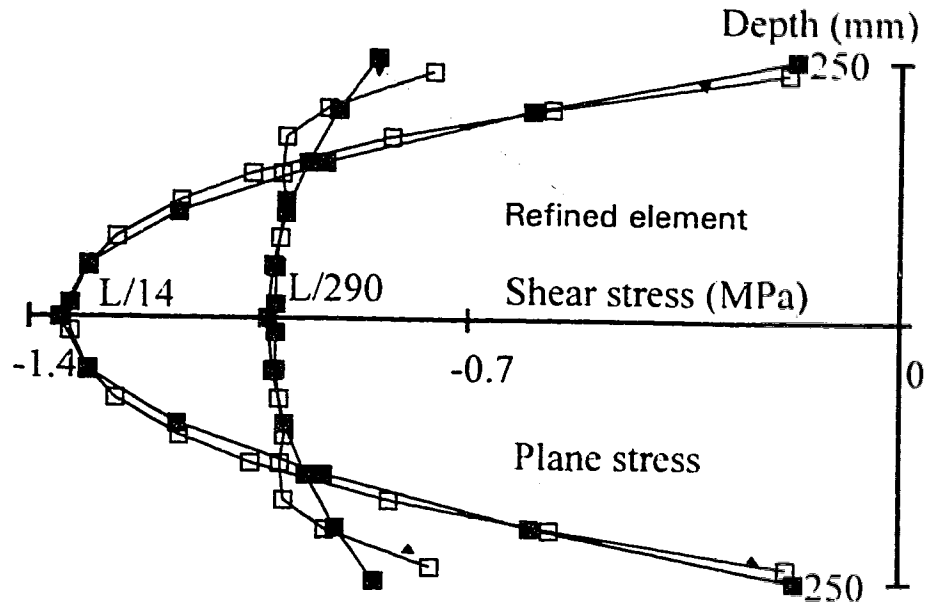
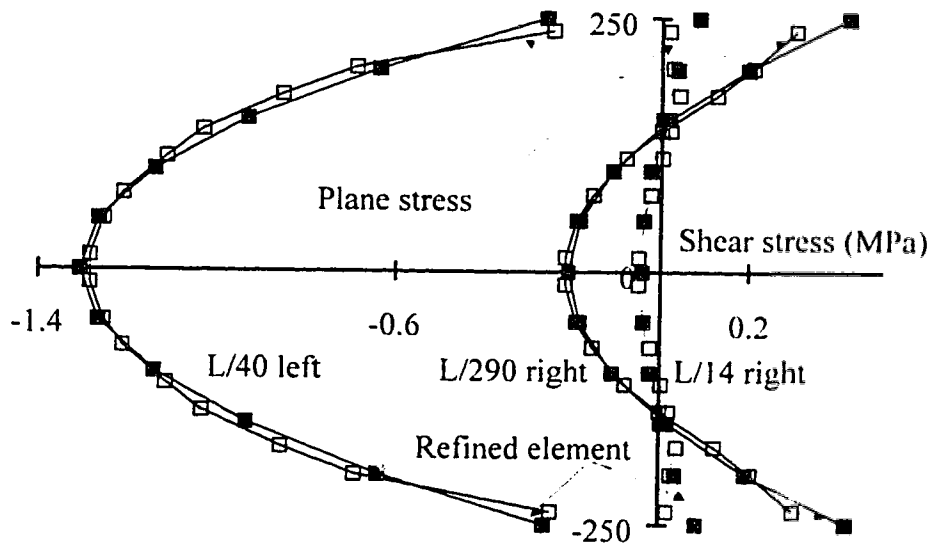


Figure 3.7 - Beams loaded at mid-span and at 1/4 of span



(a) - Load case 1



(b) - Load case 2

Figure 3.8 - Shear stress close to points of shear force discontinuity

CHAPTER FOUR

FINITE ELEMENT MODELLING OF CONCRETE SHELLS AND PLATES

4.1 Introduction

A primary motivation for the development of the refined formulation for shell elements discussed in chapter 2 and 3 was the desire to use these elements in the analysis of large reinforced concrete structures subjected to high shear forces. There are some major concerns about finite element modelling in the zones of high shear force in plates and shells. The formation and propagation of diffuse micro-cracks which coalesce into localized fracture zones usually dominates the response of reinforced concrete structures in that region. In fact the idea of smeared inclined cracking in the presence of high transverse shear forces is not actually supported by observations and/or experiments. This behavior invokes the old debate in finite element applications to concrete structures, regarding the use of discrete cracks versus smeared crack approaches.

This chapter reviews the concepts of single crack development and localization and other related issues such as mesh dependency. This is followed by a presentation of the concrete constitutive model used in this work and ends with verification of the behavior of material model in shear, compared to the test results from the literature.

4.2 Single Crack Development and Localization

From the beginning and in the earliest work on finite element analysis of concrete structures by Ngo et al. (1967) and Rashid (1968) the two different concept of discrete crack and smeared crack were essentially introduced. In the first one, each single crack causes change in the geometry of the structure by introducing discontinuity in the continuum. In the smeared crack approach, geometry is kept constant and cracks cause a distributed softening effect in the cracked region by means of the constitutive law.

To reconcile these two approaches, it is logical to argue that the smeared crack approach is suitable up to the development of a localized failure zone in the structure. Analysis then should be carried out by a discrete crack model that is suited to track down the behavior of the structure by considering the propagation of a localized failure zone or a single crack pattern through mesh changes. Until recently, conducting such an analysis is very difficult and in most cases not practical, particularly in three dimensional situations. In a large structure it is not possible to model each potential crack as an individual discrete crack. The large number of cracks adds tremendously to the complexity involved in changing the geometry of the structure in each time step. Recently, Adaptive meshing techniques have started to make progress in this area (Zienkiewicz and Zhu 1987). In this method, however, a sophisticated finite element model is needed to be able to represent the discrete crack development and progression of discontinuity in the structure. Much initial work is being carried out in the area on simulating strong discontinuities within elements (Simo et al. 1990). The object here is to identify the conditions necessary to generate a mesh change at any particular location as well as the optimum direction of change. In the meanwhile the smeared crack approach remains viable and practical in the analysis of large concrete structures.

The strain softening behavior of concrete is not actually a material property (Bazant 1976 and Van Mier 1984). It is in fact a structural property in the sense that softening can only be localized. Since each element in a fixed mesh represents a region and since within an element each integration point represents a weighted ratio of that region, a different mesh should produce different results for the same softening behavior. In other words, the constitutive response of the structure is strongly mesh dependent in the softening range of behavior. Therefore, the simplified smeared crack assumptions are valid only when micro-cracking is relatively well distributed in the structure. In the other cases either the material model has to compensate for this effect by taking the mesh into consideration or the strain field approximation must be able to account for localization in the structure.

4.2.1 Mesh Dependency

Mesh dependency comes into the picture when degradation of the material tends to localize in a line or a narrow zone. In some applications this zone may be viewed as representing a crack. In other applications it may be perceived as a slip surface called shear band. In these cases strains grow in that region of structure in a width governed by the finite element mesh size. Also localization normally tends to concentrate on a certain direction in the structure. This direction is also affected by the finite element mesh alignment.

The tendency of the strain field to localize in as narrow as possible volume of material comes from the necessity to satisfy the second law of thermodynamics. This is expressed particularly by Drucker's second stability postulate (see Drucker 1951 and 1959). It is necessary, however, to express it in a structural sense as described by Ottosen (1979). In finite element method the solution tends to choose the most efficient way to minimize the potential energy in the structure (e.g. Rayleigh-Ritz method). Considering the fact that material is in the softening range of behavior, concentration of strain in a small region or a narrow band is more energy efficient than dispersing that to the neighborhood, no matter if the band is much smaller than the actual localization band. This effect was first recognized by Hillerborg (1976 and 1978). Later it was established by many others in different applications, such as Willam et al. (1986) in his work on fracture process zones in concrete under direct tension.

Also the different levels of continuity of the displacement field inside the element and between the elements (C^1 class of continuity or higher inside the element and C^0 class of continuity between the elements), introduces a directional bias on the continuity of displacement field which forces the localization to take place parallel to element boundaries (see Steinmann and Willam 1991-a). In fact the C^0 continuity in the element boundaries allows a jump in the strain field, which attracts the localization effect. If the element boundaries are not originally oriented in the actual discontinuity line or surface,

it may lead to a very unrealistic prediction of structural response due to mesh locking (see Ortiz and Quigley, 1989 and 1991).

Thus, in the smeared crack approach and in the softening range of behavior, there are two sources of mesh dependency, mesh size and mesh orientation. Removing the mesh dependency at the structural level in the smeared crack approach needs a localization limiter to adjust for the size of the mesh. Also another arrangement is required at the level of displacement field continuity of the finite element model to avoid mesh alignment dependency. The former one could be achieved by the adoption of a mesh size limiter such as the characteristic length of Bazant et al. (1983) or by enhancement in the concrete constitutive law (see Willam et al. 1986). These issues will be discussed in the following section.

4.2.1.1 Mesh Size

Localization limiters are in most cases length parameters that govern the width of the strain localization zone. One of the earliest localization limiters is the crack band model introduced by Bazant et al. (1983) in which the minimum size of elements is a fixed parameter. The concept of localization limiter later developed into a more sophisticated form called "*Nonlocal Damage Model*" (see Bazant et al. 1988-a and b) in which the state variables that control strain softening are defined as nonlocal or average quantities throughout the continuum. In this method damage or localization cannot remain in a narrow region enforced by the size of the mesh. Another example in this area is the method called "*Consistent Characteristic Length*" proposed by Oliver (1989). In this method the length parameter is deduced from hypothesis governing the behavior in the crack band zone. By analysis of the energy dissipated inside of the band, the characteristic length emerges naturally as the ratio between the energy dissipated per unit surface area (fracture energy) and the energy dissipated per unit volume (specific energy) at each crack point. This elaboration requires a proper estimate of the fracture energy which is a function of the average crack spacing in the fracture zone.

There is another approach to implement the localization limiter in finite element model of concrete structures by integrating it into concrete material model. This method is based on the concept of fracture energy release rate of concrete in tension. In this approach the degradation of material is invariably expressed in terms of crack opening displacement rather than strain (see Willam et al. 1986). To calculate strain from crack opening displacement, the softening slope of the stress strain curve must be changed in order to keep the fracture energy release rate constant. Here the mesh size dependency comes into picture. Regardless of the size of the element, fracture energy release rate is only a function of the crack spacing in the real structure. Thus if the size of element is not as big as the crack spacing, it cannot accommodate the localization of strain softening alone and the strain disperses to the other elements in that neighborhood.

This method naturally fits into the Mode-*I* fracture (tensile fracture) but the concept was expanded implicitly to the case of multiple cracking in general case of stress condition by the means of a mixed fracture approach. This has been done for example by incorporating the ratio of fracture energy release rate in Mode-*II* fracture into the Mode-*I* fracture (see Willam et al. 1986 and Rots et al. 1987). Although this is a very useful approach, it suffers from lack of direct control on the crack spacing in the mixed mode of fracture.

4.2.1.2 Mesh Alignment

To eliminate the mesh dependency in the smeared crack approach, the bias of the finite element discretization in the continuity of displacement field should be removed. Different classes of continuity inside elements and between them need special treatment to capture the localization and single crack development in the structure. A very effective approach is to use mesh adaptivity and remeshing techniques to reconstruct the finite element mesh in order to align the element boundaries along the emerging discontinuities. In this way the smeared crack approach is becoming similar to the discrete crack method. The techniques of remeshing are derived from mesh generation concepts and error

estimating analysis (see, for example, Zienkiewicz and Zhu 1987, Ortiz et al. 1989 and Bicanic et al. 1991).

In recent years, however, a new family of elements have evolved in which some brand new enrichment strategies were used to capture jump conditions in the displacement continuity inside an element due to localization (see, for example, Simo et al. 1990 and Steinmann and Willam 1991-b). Applying these techniques could remove the necessity of remeshing in the finite element model. The new developments in this method of handling localization in the presence of strong discontinuity in solid mechanics are promising (see, for example, Simo, et al. 1993, Oliver et al. 1994 and Oliver 1995).

The above methods for mesh realignment or other methods for handling discontinuities in displacement fields have been demonstrated in two dimensional applications. For three dimensional problems still it is not possible to capture the localization surface reliably.

The analysis of shells and plates in regions of high shear forces is three dimensional in nature. In this situation, it is not easy to track down the development of a single crack pattern. To be precise, it needs a very fine mesh of three dimensional brick elements in several layers across the thickness direction with a powerful remeshing techniques to realign the element boundaries along the emerging crack pattern. The only affordable and/or available alternative is to reduce the mesh sensitivity of the finite element model by using a localization limiter. A material model with a built in localization limiter is the most convenient approach.

4.3 Concrete Material Model

The inadequacy of the concrete material model is the most important obstacle in the analysis of concrete structures (see, Bathe et al. 1989). Development of such models have been done through different approaches that can be categorized into three major groups, elasticity based models, plasticity based models and advanced models developed recently based on concepts of micro-mechanics of inelastic phenomenon in the material

micro-structure. Among the latter are the *Microplane* models proposed by Bazant (1984). In this approach a macro model for smeared constitutive relations would be based on simple traction relationships applied to a set of planes of various orientations. These planes called "*Microplanes*" and their responses are related to the macro-level through a probability function simply by integration over all of the spatial directions (Bazant et al. 1984, Bazant et al. 1988 and Carol et al. 1992). This approach is hampered by lack of understanding of the probability function and by the difficulty in carrying out the integration on a sphere around each material point.

Elasticity based models are divided into several groups. The most important one is the hypoelastic approach in which the material behavior is described in terms of the increments of the stress and strain. The constitutive law in this case is thought to be a tangent stiffness matrix dependent on the current state of stress. Thus, hypoelasticity is able to represent the deformation history dependency in concrete materials. Among the models developed in this category are the orthotropic models developed by Darwin and Pecknold (1977), Elwi and Murray (1979), Vecchio and Collins (1982) to mention a few. But this class of material models loses its accuracy in the highly nonlinear range of behavior due to the increasing level of anisotropy in the material. Theoretically, it is possible to push the hypoelastic model further in this range of behavior, but practically due to the large number of material constants to be defined in the anisotropic range, it is not usually recommended. In general, elasticity based models are mostly suitable for the range of small to moderate nonlinearity, before anisotropic behavior becomes significant. Beyond this, plasticity based models are preferred because they are thought to render more accuracy, generality and are also convenient in formulation.

In plasticity formulation, the robust theoretical background which was developed initially for metals, has been expanded to concrete and other geomaterials. A comprehensive overview of the earlier works in this area was reported by Chen (1982). Plasticity models proposed by Willam et al. (1975), Ottosen (1977 and 1979), Hsieh et al (1982) are well known among others. Development of more sophisticated plasticity

models for concrete is still a challenge. one of the latest is the model proposed by Menetrey and Willam (1995). Most of the classical plasticity models are problematic, particularly in the softening range of concrete behavior. This is natural because these models are directly derived from models originally proposed for metals. In the development of the plasticity models for concrete all the ingredients in the plastic theory of metals must be reinvented to incorporate the cohesive and frictional nature of cementitious materials like concrete as well as unique plastic volume change characteristics pertinent to the cracking and softening behavior of this material. Yield surfaces, hardening criteria, flow rules and failure envelopes are all affected. In addition, a softening criteria and a residual strength representative surface is necessary to cover the full range of behavior of these materials.

Some of the major problems in elasticity approach can be easily overcome in plasticity formulation. Among those, is the hydrostatic pressure sensitivity accompanied by limited volumetric expansion phenomenon in the highly nonlinear range of behavior which can be easily dealt with by incorporating a nonassociated flow rule in plasticity formulations. But the major concern in concrete material model is the requirement to cover the softening range of behavior. Since concrete exhibits a considerable residual strength after failure, concrete structures are usually able to attain the required ductility specified in the design rules. To capture this mode of behavior in the analysis process requires a sophisticated concrete material model to represent the strain softening range of this material.

The complexity in the softening range of behavior is predominantly due to the localization phenomenon which is in contrast to the smooth and distributed deformation in the hardening behavior (see Bazant 1976). Hence, constitutive relations for strain softening part of the material model are mostly derived from the concepts of fracture mechanics. Among the earliest version of this approach is the plastic fracture theory by Bazant et al. (1979). Naturally, this approach works fairly well in the cases dominated by a tension field in which the crack pattern can easily be classified experimentally. In the

general state of stress that is dominated by a compression field, localization is in the shape of a blunt shear band which can hardly represent a crack. Fracture energy based plasticity material model for concrete proposed by Paramono and Willam (1989) used the implicit approach developed originally by Willam et al. (1986) to by-pass this dilemma.

Program NISA-80 (Stegmuller et al. 1983) in which the refined plate shell element described in Chapters 2 and 3 has been implemented, already incorporates a two dimensional orthotropic failure model developed by Massicotte et al. (1988). This model is classified within the hypoelastcity based group. The current study is primarily concerned with the out of plane shear behavior of shell and plates. Such analysis requires full three dimensional concrete material model. It was not deemed possible to expand the Massicotte model to full three dimensions. On the other hand recent work by Xie et al. (1995) expands the two dimensional aforementioned Paramono and Willam (1989) plasticity based model to a full three dimensional application. That work was originally implemented in program ABAQUS (Hibbitt 1993) by Xie et al. (1995) . However, because of the successful application of this model in representing the behavior of the concrete columns, it was decided to try it in the context of thick shells subject to out of plane shear forces. This has been carried out by incorporating the Xie material model into the program NISA-80. The following sections present a short overview on the basic assumptions of this model.

4.3.1 Three Dimensional Constitutive Model

Conceptually most of the concrete nonlinearities depend on the three dimensional state of stress (see, for example, Gedlin et al. 1986), but some of the very successful concrete material models to date are based on a two dimensional approach. The extension of these models developed originally for plane stress or plane strain conditions to three dimensional state of stress is not easy because of the complexity involved in the formulation (due to problems like confinement and/or complicated crack pattern formation) and also because of the lack of experimental data in the three dimensional state of stress.

Two dimensional models can easily be used in study of beams in the zones of high shear force because all the components of stress field are located in the same plane. In plate and shell structures in the high transverse shear zone, stress field is strongly three dimensional because of the contribution of out of plane shear forces. If transverse shear force is not significant in that region, extending the formulation of two dimensional constitutive models to three dimensional one is legitimate. As an example, Massicotte et al. (1988 and 1990) have extended a two dimensional plane stress hypoelastic constitutive law to a three dimensional model for plate and shells. In this method a plane stress constitutive law for each layer of concrete in the thickness direction is used but the constitutive equation is artificially augmented to a three dimensional constitutive matrix. This augmentation takes place by assuming that out of plane shear rigidities G_{xz} and G_{yz} are equivalent to the inplane value of the shear rigidity G_{xy} . The logic behind this assumption is simple, degradation of shear rigidity is isotropic in concrete plate and shells. This argument conceptually is not valid in a three dimensional state of stress in concrete plate and shells, but it might be acceptable when the magnitude of shear stresses are small and structure is not exposed to large shear deformation or it is not susceptible to shear failure. Such circumstances require a true three dimensional constitutive model.

The fracture energy based plasticity model mentioned above is inherently a three dimensional model written in the space of principal stresses σ_1 and σ_3 . This formulation is adequate for two dimensional problems but to extend it to a three dimensional applications it must be transformed to the space of general stress tensor with 6 components of stress $\langle \sigma_{xx}, \sigma_{yy}, \sigma_{zz}, \tau_{xy}, \tau_{yz}, \tau_{xz} \rangle^T$. To have a three dimensional constitutive model, a transformation algorithm from the space of principal stresses to the state of general stress tensor is required. The algorithm described by Xie et al. (1994) is employed in the present study.

4.3.2 Fracture Energy Based Plasticity Model (Paramono et al. 1989)

This model is an isotropic hardening material law with a nonassociated flow rule in which after peak, an isotropic softening mechanism governed by fracture energy release rate is implemented.

4.3.2.1 Isotropic Hardening Model

In the initial stages of behavior the material remains elastic up to an initial value for hardening parameter k , (i.e. $k \leq k_0$). After that and until a strength envelope is reached, isotropic strain hardening behavior governs the state of material by a criterion in terms of principal stresses and hardening parameter ($k \leq k_p = 1$). In this approach the hardening parameter is defined as a function of plastic strain indicator $\tilde{\epsilon}_p$, which is a monotonic parameter that accumulates the Euclidean norm of increment in plastic strain tensor $\{\Delta\epsilon_p\}$, and a ductility parameter χ_p that stands for the effect of confinement on the hardening rule. The model uses the Leon tri-axial strength failure criterion (see Ramano 1969) as a strength envelope at which $k = k_p = 1$.

Close to failure surface when hardening parameter k , approaches $k_p=1$, material goes through volumetric expansion and it becomes hydrostatic pressure sensitive. In this case the direction of the principal strain and stress no longer coincide, indicating the existence of a high level of anisotropy in the material. A non-associated flow rule, adopted in this approach, can properly address this problem.

4.3.2.2 Isotroic Softening Model

After the state of stress reaches the failure surface, degradation of the material starts and it ends down at a residual strength envelope. To monitor the softening behavior of the material in this range the measure used is the equivalent tensile fracture strain indicator $\tilde{\epsilon}_f$. This parameter is similar to $\tilde{\epsilon}_p$, but is a function only of the tensile components of the strain tensor, $\{\Delta\epsilon_f\}$.

In fracture mechanics degradation of tensile strength is properly expressed in terms of crack opening displacement u_f instead of ε_f which renders a more physical sense. This behavior usually expresses in a very sharp descending function. Relating the degradation of tensile strength to the crack opening displacement for each individual crack removes the problem associated with the measuring length in strain measurement. The average strain in the specimen, therefore, would be proportional to the number of cracks or to the crack spacing in the structure.

$$\varepsilon_f = \frac{u_f}{h_t} \quad (4.1)$$

The symbol h_t in the above equation is the crack spacing in tension. It is easy to determine crack spacing in pure tension but in the general case, when the state of stress is not dominated by tension, some other elaboration is required to determine this parameter.

Localization or crack band in the general state of stress, dominated usually by compression, is actually in a kind of a shear band. Therefore, the shear mode of fracture (or Mode-II fracture) in this case must come into picture.

Fracture energy release rate in developing a single crack in tension is usually written as:

$$G'_f = \int_0^{u_f} \sigma_t du_f \quad (4.2)$$

This energy is for a unit area of crack surface ΔA_t . In Mode-II fracture also the fracture energy release rate G''_f can be written in the same way. Here it is assumed that failure in compression manifests also as a different form of failure in tension, say by cracks at a different orientation. The G''_f energy release rate again is for unit area of crack surface, in this case ΔA_c . In other words, fracture energy is proportional to the area of the crack surface because crack in a continuum is taking place in a line or on a surface

not in a volume and its energy releases on this surface not in the volume of material. Accepting this intuition, the density of energy release rate in terms of crack surface area should be equal for the fields dominated by tension or compression.

$$\frac{G'_f}{\Delta A_t} = \frac{G''_f}{\Delta A_c} \quad (4.3)$$

Considering the fact that the density of crack surface in a volume is proportional to the crack spacing in the smeared crack approach we can write:

$$\Delta A_t = \frac{\Delta V}{h_t} \quad \text{and} \quad \Delta A_c = \frac{\Delta V}{h_c} \quad (4.4)$$

In which h_c is an equivalent crack spacing in the compression dominated case. Now Eq. 4.3 can be written in the form:

$$G'_f h_t = G''_f h_c \quad (4.5)$$

In this way by incorporation of the ratio of the fracture energy release in Mode-II and Mode-I, an implicit relationship for crack spacing indicator, h_c , in the compression dominated state of stress is found.

More details about this approach and its implementation can be found in Paramono et al. (1989) and Xie et al. (1994). It should be noted, however, that since this model is based on a nonassociated flow rule it results in a non-symmetric incremental stress-strain relationship and consequently a nonsymmetric stiffness matrix. This means that a nonsymmetric solver has to be implemented into the program NISA. This program uses a skyline stiffness matrix to start with and, therefore, all assembly and storage routines are based on a skyline scheme. For the purposes of this thesis then a skyline nonsymmetric solver developed by Chan (1986) was implemented and the assembly and storage systems modified accordingly.

4.3.3 Implementation of 3D Material Model in Plate and Shell

The elastic constitutive equation of a three dimensional state of stress in an arbitrary frame of reference in plates and shells can be shown as follows:

$$\begin{Bmatrix} \sigma_{xx} \\ \sigma_{yy} \\ \sigma_{zz} \\ \tau_{xy} \\ \tau_{yz} \\ \tau_{xz} \end{Bmatrix} = \frac{E(1-\nu)}{(1+\nu)(1-2\nu)} \begin{bmatrix} 1 & \frac{\nu}{1-\nu} & \frac{\nu}{1-\nu} & 0 & 0 & 0 \\ & 1 & \frac{\nu}{1-\nu} & 0 & 0 & 0 \\ & & 1 & 0 & 0 & 0 \\ & & & \frac{1-2\nu}{2(1-\nu)} & 0 & 0 \\ & & & & \frac{1-2\nu}{2(1-\nu)} & 0 \\ & & & & & \frac{1-2\nu}{2(1-\nu)} \end{bmatrix} \begin{Bmatrix} \varepsilon_{xx} \\ \varepsilon_{yy} \\ \varepsilon_{zz} \\ \gamma_{xy} \\ \gamma_{yz} \\ \gamma_{xz} \end{Bmatrix} \quad (4.22)$$

But the same constitutive relationship for plates and shells with respect to the local coordinate system r, s and t has to satisfy the constraint of $\sigma_{tt} = 0$ (t is the local coordinate in the thickness direction). This implies that in three dimensional finite element formulation of plates and shells, the same as in the plane stress problem, the normal strain in the thickness direction must be condensed out of the formulation. Thus the actual number of the component of stress reduces to five $\langle \sigma_{rr}, \sigma_{ss}, \tau_{rs}, \tau_{st}, \tau_{rt} \rangle^T$.

In the local coordinate system. Applying the constraint of $\sigma_{tt} = 0$ can be done by static condensation of the three dimensional constitutive equation with respect to the ε_{tt} .

$$\begin{Bmatrix} \sigma \\ \sigma \\ \tau \\ \tau \\ \tau \end{Bmatrix}_{5 \times 1} = [D]_{5 \times 5} \begin{Bmatrix} \varepsilon \\ \varepsilon \\ \gamma \\ \gamma \\ \gamma \end{Bmatrix}_{5 \times 1} \Rightarrow \begin{Bmatrix} \sigma_{rr} \\ \sigma_{ss} \\ \tau_{rs} \\ \tau_{st} \\ \tau_{rt} \end{Bmatrix} = \frac{E}{(1-\nu^2)} \begin{bmatrix} 1 & \nu & 0 & 0 & 0 \\ & 1 & 0 & 0 & 0 \\ & & \frac{1-\nu}{2} & 0 & 0 \\ & & & \frac{1-\nu}{2} & 0 \\ & & & & \frac{1-\nu}{2} \end{bmatrix} \begin{Bmatrix} \varepsilon_{rr} \\ \varepsilon_{ss} \\ \gamma_{rs} \\ \gamma_{st} \\ \gamma_{rt} \end{Bmatrix} \quad (4.23)$$

The above treatment indicates that the ε_{rr} exist but its effect is condensed out of the solution. The material model is still three dimensional and no approximations have been made so far. The three dimensional constitutive matrix in the local coordinate system $[D]$ later must be augmented to a 6x6 matrix by adding zero values as its third column and third row to be able to use the standard transformation matrices for three dimensional space in global frame of reference.

4.3.4 Programming

Since the constitutive equation for concrete material model in the range of nonlinear behavior is not symmetric (due to the dilatancy effects in concrete material that is represented by nonassociated flow rule in the formulation), the stiffness matrix of the structure is not symmetric as well. Program NISA-80 has been equipped with a nonsymmetric solver developed by Chan (1986) to be able to address the problem. Although this elaboration seems quite simple, in the context of programming and alteration of an existing computer code, it is technically troublesome.

Program NISA uses a one dimensional array to store the stiffness matrix and some other variables and parameters in the program. This approach needs a very strict book keeping policy for the memory to distinguish between different variables and parameters stored in that array. The required memory to store a nonsymmetric stiffness matrix is obviously higher than that in the symmetric solver and the book keeping policy in the program has to be changed accordingly to account for the change in the size of the stiffness matrix in the one dimensional array.

The new program with nonsymmetric solver needs more memory and it also runs slower than the original program. The computational efforts to solve a nonsymmetric system of equation is certainly higher than that in a symmetric one, but in the nonlinear analysis of structures, this can not make a significant difference in the required CPU time for running the problem. In fact in most cases the solver algorithm is not consuming the major part of the computational efforts in the analysis. Numerical calculations are mostly

concentrated on re-evaluation of the state of stress on the integration points which has nothing to do with the solver algorithm.

4.4 Tension Stiffening

The above treatment deals specifically with concrete continua. Reinforcing steel bars embedded in concrete pose a different set of problems. In an uncracked reinforced concrete member subjected to tension, bond between the concrete and steel is represented by strain compatibility. In other words, the tensile force is resisted by both concrete and reinforcement, until the ultimate tensile strain in concrete is reached. At this stage, cracking initiates. At the crack only the steel reinforcement carries the tensile force but the concrete surrounding the reinforcement between consecutive tensile cracks can still transmit tensile stresses. This phenomenon results from the bond slip between reinforcing bars and surrounding concrete at the crack and it contributes to the stiffness of the structure by gradual release of stresses in the uncracked portions between the cracks. The phenomenon is called “tension stiffening” and it affects the service behavior of reinforced concrete members by increasing their tension and/or bending stiffness in the post cracking range of behavior.

Traditionally, there are two approaches to account for the tension stiffening effect in finite element analysis of concrete structures. In the first one an increase in the reinforcement stiffness is proposed to account for the concrete between the cracks (Gilbert et al. 1977). In the second the concrete stiffness is increased by changing the sharp slope of its descending softening branch to a more gentle and gradual softening slope as shown in Fig. 4.1 (Scanlon 1971, Lin et al. 1975 and Massicotte et al. 1990). However there is yet a third approach in which the effect of tension stiffening is indirectly integrated in the analysis by artificially increasing in the value of the fracture energy release rate of the plain concrete, G_f by ΔG_f (Rots 1988).

Formulation of tension stiffening in the case of uniaxial tensile force in the member is straight forward, but in the bi-axial tension field, as in the tension zone of

plate and shells, the interaction between reinforcement and concrete becomes more complicated. The main reason is that, the strain softening behavior of cracked concrete is dominant in the direction normal to the crack but tension stiffening is taking place along the reinforcement direction. The two directions may not be the same.

Tension stiffening is a phenomenon attributed to the cracked reinforced concrete. It initiates with the appearance of the first crack and its effect continues with every forthcoming crack until no more cracks can appear. This stage usually concludes with yielding of the reinforcement. Thus, most of the existing tension stiffening models are based on orthotropic elasticity concrete material models in which the concept of cracking is directly used. In these approaches once the orientation of the crack is determined, the behavior of concrete in the direction normal to the crack is known. A unique softening regime defined for the uniaxial tension case is mostly used in the direction normal to the crack.

By contrast, in plasticity based models in order to account for tension stiffening in a bi-axial stress field the approach must be different. Plasticity models use the concept of softening instead of crack which is not a directional criterion. Once the orientation of softening in the material is found (based on the principal tensile strain), although literally it resembles the crack line but the softening behavior in crack normal direction is not the same as that in the uniaxial tensile case. In fact in the plasticity models, hardening and softening rules are applied to a material point in every direction in a uniform manner. Therefore, there is not any clear distinction between the tensile crack dominated area and the compression one.

For instance, plasticity model proposed by Paramono et al. (1989) in the pure uniaxial tension case gives a strain-stress relationship for concrete exactly similar to that of the actual concrete with elastic behavior before f_t' and a sharp descending branch after that. But in a bi-axial stress field, existence of the principal compression stress in the material that could arise from the contribution of a shear stress, causes hardening and softening behavior somewhere between tension and compression as shown in the Fig. 4.2.

In other word there is not a unique softening regime. Developing a tension stiffening model in a plasticity approach needs some special modifications in the material model particularly in the tension dominated field to render a more unified representation of the tensile cracking behavior in the bi-axial stress domain.

In this thesis some preliminary attempts had been made to integrate the effect of tension stiffening into the finite element model of plates and shells but those attempts were not successful. It was decided later to discard the implementation of tension stiffening in this model. It was believed that, in the region of high transverse shear force of plate and shells, the contribution of the tension zone to the response of structure and its strength is not significant. This reduces the effect of tension stiffening in the problem and removes the necessity of implementation of this phenomenon into finite element model of plates and shells in the regions of high shear force.

4.5 Verification of The Concrete Material Model

Due to the complications involved in conducting experiments in three dimensional state of stress for concrete, verification of material model is usually carried out by using the two dimensional experimental results abundantly available in the literature. In this study a major objective was to determine the ability of the material model to represent concrete behavior whenever shear is the dominant component of stress. A well known experimental data source in this area is a series of panel tests reported by Vecchio and Collins (1982). These tests (called PV-Series) had targeted the inplane shear behavior of the concrete panels in different combination of reinforcement ratio and bi-axial inplane stresses. Vecchio and Collins tested 30 specimens altogether out of which 22 were merely in pure shear loading condition. Although the tests are two dimensional, the dominance of the shear force justifies their application in validating of the material model discussed in the previous sections.

4.5.1 Description of Specimens

In the PV-Series, each specimen is 890 x 890 x 70 mm, reinforced with two layers of welded wire mesh. Reinforcement bars are oriented parallel to the panel sides and inplane load and shear forces are applied to the concrete panel through a system specially designed to render a uniform distribution of shear and inplane forces to the panel sides. Figure 4.3 illustrates this mechanism (Vecchio and Collins 1982).

4.5.2 Finite Element Model for PV-Series

In this study five of the PV-Series specimens are chosen to investigate the performance of the material model and examine its characteristics. Three of these specimens are in pure shear loading condition (PV-4, PV-6 and PV-27) differing primarily in the level of reinforcement ratio. The remaining two (PV-23 and PV-28) are subjected to combined shear and inplane loading. The material properties of these specimens are listed in table 4.1.

In the finite element model of these specimens only one element is used to model each specimen. The sixteen node shell element used in these cases has not shown any zero energy mode and its bi-cubic displacement field provides enough accuracy to represent the uniform strain field in the specimen with one element. Figure 4.4 illustrates this finite element model.

4.5.3 Prediction of The PV-Panels Response

Comparison between the finite element predictions for response of the specimens and the actual test results help us to understand some of the basic aspects of the material model. The main concern herein, is to find out the characteristics of the plastic material model when the state of stress is predominantly originated from the shear force.

The state of stress after initiation of crack in concrete panel is different from that in pre-crack situation. For example in the case of pure shear forces before cracking, concrete is in shear and rebars are in zero stress condition. Initiation of crack puts rebars

in tension and causes a biaxial compression in concrete. The increases in the shear carrying capacity of concrete after cracking is in fact dominated by this compression field. In plasticity material model this phenomenon classifies as confined pressure. To investigate the ability of the material model to represent the effect of compression provided by rebars in changing the behavior of the structure after cracking, specimen PV-4 is chosen for some experimental finite element analysis. This specimen analyzed with the actual reinforcement ratio reported in the test and also with three other hypothetical ratios for steel rebars. The results of the analysis are shown in Fig. 4.5.

Without reinforcement, there is no confinement on the concrete after cracking and the cohesive-frictional nature of a classic cementitious material can be seen from the graph provided in Fig. 4.5. The lack of confinement in this case does not allow the frictional characteristics of the material to increase the shear strength of the specimen in any sense. Friction in this case provides a little ductility in the specimen before rupture similar to the slipping phenomenon between two rough surfaces.

In the next step steel rebars with a ratio equal to the actual value in the experiment are used in the model. A different mode of behavior is detected. After cracking, the confinement pressure provided by steel rebars causes an increase in the shear capacity of the specimen due to the contribution of frictional characteristics of the material model. This contribution exists until the strain in the rebar reaches the yield limit. Yielding of the rebars restricts the amount of the confinement on the material causing a constant value for the shear capacity of the specimen. The frictional characteristic of the material also provides a kind of ductility for the specimen as shown in Fig. 4.5.

To examine the effect of higher level of confinement in the specimen, the yield limit of the rebar hypothetically increased which practically make it elastic without yield limit. As shown in Fig. 4.5, the shear capacity of the specimen is increased considerably indicating the sensitivity of the material model to the confinement pressure.

In the final step the ratio of the steel rebars is also increased by 70 percent to amplify the effect of the confinement in the specimen (yield limit is still very high). The results show an increase in the shear capacity of the specimen as well as its shear stiffness. The response of the specimen in the analysis is very similar to the test result of the PV-27 shown in Fig. 4.8 which has the same amount of steel rebars.

This simple example shows the ability of the plasticity material model to represent the effect of compression field, produced by steel rebars after cracking, in the shear behavior of the concrete panels.

4.5.3.1 Response of The Specimens in Pure Shear

Comparison of the finite element response of the specimen PV- 4 and its actual test result are shown in Fig 4.6. Although the analysis gives a good agreement with test result in some parts, there are still two major difference between them.

First, the analysis shows a higher ultimate value for the shear stress in the specimen. In the analysis, the beginning of ductile behavior of the specimen is fairly matched with the yield strain of the rebars, but in the test results this is not the case. In other words, ductile behavior in the actual experiment starts before the average strain reaches the yield limit of rebars. This could happen when localized yielding occurs in the rebar, most probably at the weld points of the mesh. By contrast in another example, PV-6, the ductile behavior in the experiment starts exactly when the average strain in rebar reaches to the yield limit, as is shown in Fig. 4.7.

Second, analysis of the PV-4 specimen shows the observed ductility in the specimen but not to the extent captured in the experiment. This indicates the limitation of the plasticity material model in representing the state of material in the case of extensive cracking in concrete. In PV-6, the reinforcement ratio is 70 percent higher than that in PV-4 and again the same phenomenon exists. The analysis couldn't show the softening behavior of the specimen as was shown in the test. In this case initiation of yield in the rebars causes a jump in the strain field of the specimen which is hard to represent

accurately by the concrete material model in that highly stressed state of stress. This makes the solution unstable and program can not find an equilibrium position in that vicinity.

In specimen PV-27, the steel reinforcement ratio is the same as PV-6 but its yield limit is higher ($f_y = 442$ instead of 266 MPa). The specimen in the test didn't show any ductile behavior the same as that in PV-6 but its ultimate shear strength is almost 30 percent higher than that in the previous example even though the concrete in this specimen is much softer (f_c' of the concrete is 20.5 compared to the 29.8 MPa in PV-6). This indicates the effect of confinement provided by steel rebars. In the finite element analysis of the specimen, the same trend is predicted with some minor differences as shown in Fig. 4.8. After initiation of crack in the specimen the analysis shows a linear or close to linear relationship between shear stress and rebar strain (an indicator of the confinement on the concrete). This depicts thoroughly the cohesive and frictional nature of the plasticity material model. In the experiment there is a transition curve after cracking and before the constant slope of the curve. The same phenomenon exists in all the other examples with high confinement stresses. This indicates that although the material model can represent the frictional nature of concrete almost flawlessly, it is not as good when cohesion comes into the picture.

4.5.3.2 Response to Combined In-plane Normal and Shear Forces

In the PV-Series, there are only a few examples with combined inplane and shear forces, among those there is only one specimen with tension dominated inplane forces. However, according to these test results, the existence of the normal inplane forces does not change the mode of behavior of the reinforced shear panels. In fact, even without the normal forces, the inplane stresses will be generated by reinforcement after initiation of crack in the specimen. Thus, the mechanism of behavior described in the pure shear cases again appears in the presence of the inplane normal forces.

Finite element response and the actual test result for the specimen PV-23 is shown in Fig. 4.9. Behavior of this example is essentially the same as that of the PV-27 in previous case. Both specimens have the same amount of reinforcement and the same quality of concrete (f'_c for both is equal). In PV-23 the shear force is accompanied by a biaxial inplane compression force equal to 39 percent of its shear force. This force acts as another source of confined pressure (besides the confinement provided by the reinforcement) on the concrete and causes a shift in the behavior of the specimen compared to PV-27 as illustrated in Fig. 4.10.

In specimen PV-28 the shear force appears with a biaxial inplane tension force equal to 32 percent of the shear force magnitude. The specimen has the same amount of steel rebars compared to the previous examples and with almost the same concrete quality (f'_c is equal to 19. MPa instead of 20.5 MPa for PV-27). Finite element analysis and test results are shown in Fig. 4.11. In the test result there is no sign of transition curve before starting frictional behavior in the specimen, the same as that predicted by finite element. The ultimate value for the shear strength obtained in this analysis is about 30 percent less than the actual value in the experiment which indicates the sensitivity of the material model to the level of confinement provided by external inplane force and steel rebars. This phenomenon is described below.

Comparing the finite element response of the specimens PV-23, PV-27 and PV-28 shows that, inplane compression force in specimen PV-23 adds to the confinement provided by steel rebars and makes the plasticity material model so robust, it overshoots the experimental ultimate value for the shear strength (see Fig 4.9). However, the tensile inplane force in specimen PV-28 reduces the amount of the confinement provided by reinforcement and causes a lower estimate on the shear strength of the specimen in the analysis (as shown in Fig. 4.11). In the absence of the inplane normal forces (i.e., specimen PV-27), analysis still gives a lower estimate for shear strength compare to the test result but its prediction margin is much closer (see Fig. 4.8). The above observation shows the so called sensitivity of the material model to the confined pressure in

estimation of ultimate shear strength of the specimens but material model is still accurate enough to represent the general trend of the concrete behavior.

Sensitivity of the plasticity material model to confinement can be solved by calibrating it for each application depending on the level of confined pressure. This elaboration is not easy when the state of stress varies in different locations of the structure. Plate structures are typically in this category in which, state of stress changes from biaxial tension to biaxial compression through the thickness. In such problems, the accuracy of the analysis can not be improved considerably by calibration process on plasticity material model.

		Concrete		Reinforcement Transverse & Longitudinal		
		f'_c	ε'_c	f_y	ρ_t	ϕ
		(MPa)		(MPa)		(mm)
PV - 4	Pure shear	26.6	0.0025	242	0.01056	3.45
PV - 6	Pure shear	29.8	0.0025	266	0.01785	6.35
PV - 27	Pure shear	20.5	0.0019	442	0.01785	6.35
PV - 23	Shear & Compression	20.5	0.0020	518	0.01785	6.35
PV - 28	Shear & Tension	19	0.00185	483	0.01785	6.35

Table 4.1 - PV panels material properties

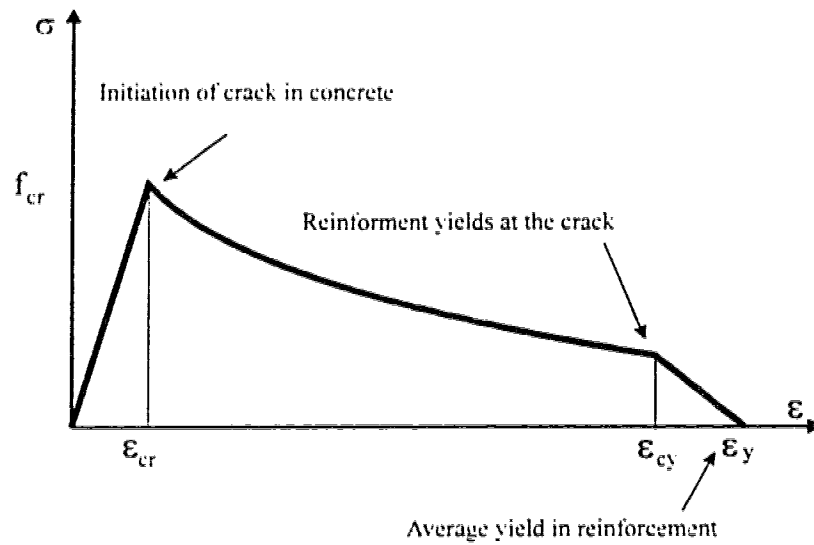


Figure 4.1 - Tension stiffening

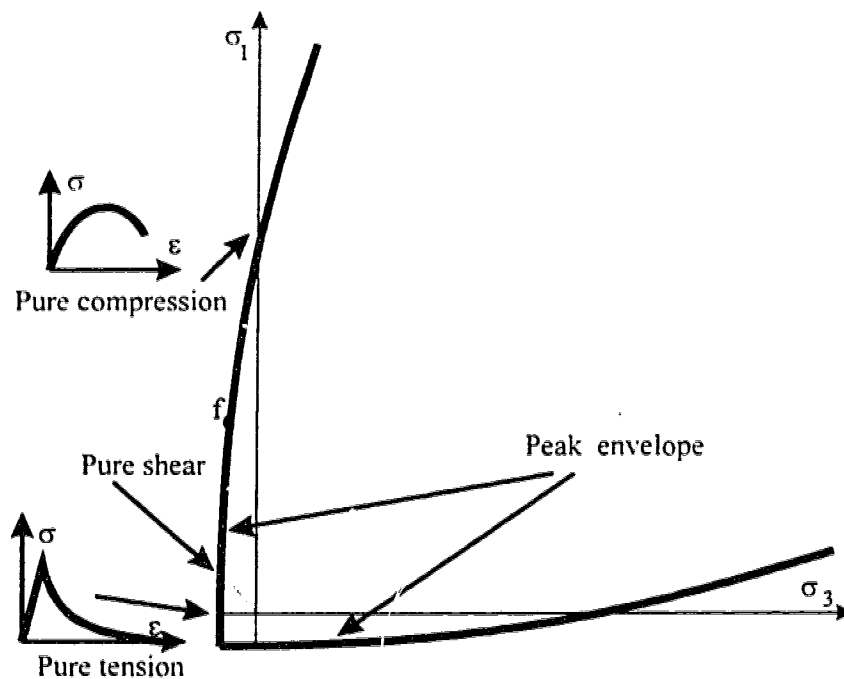


Figure 4.2 - Strain softening in different combination of bi-axial stress

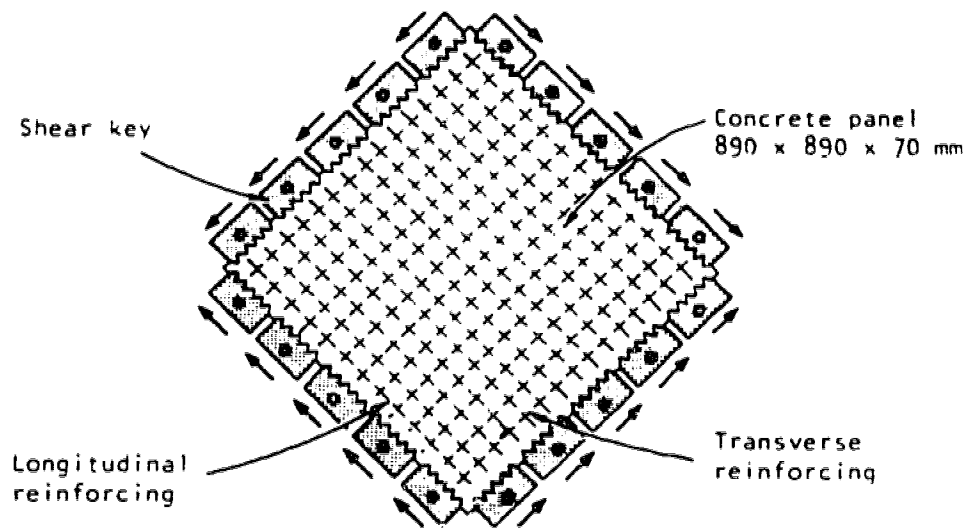


Figure 4.3 - Load application Mechanism on PV panels (Vecchio and Collins 1982)

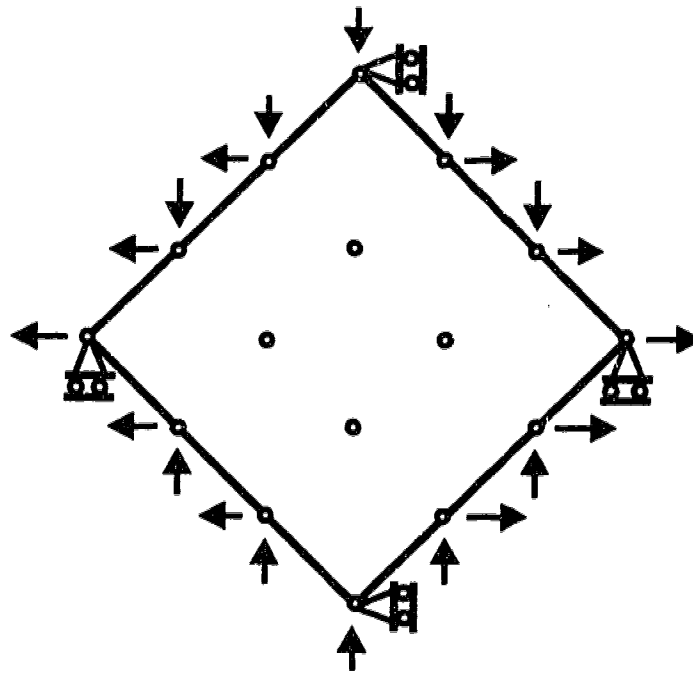


Figure 4.4 - Finite element model for PV series

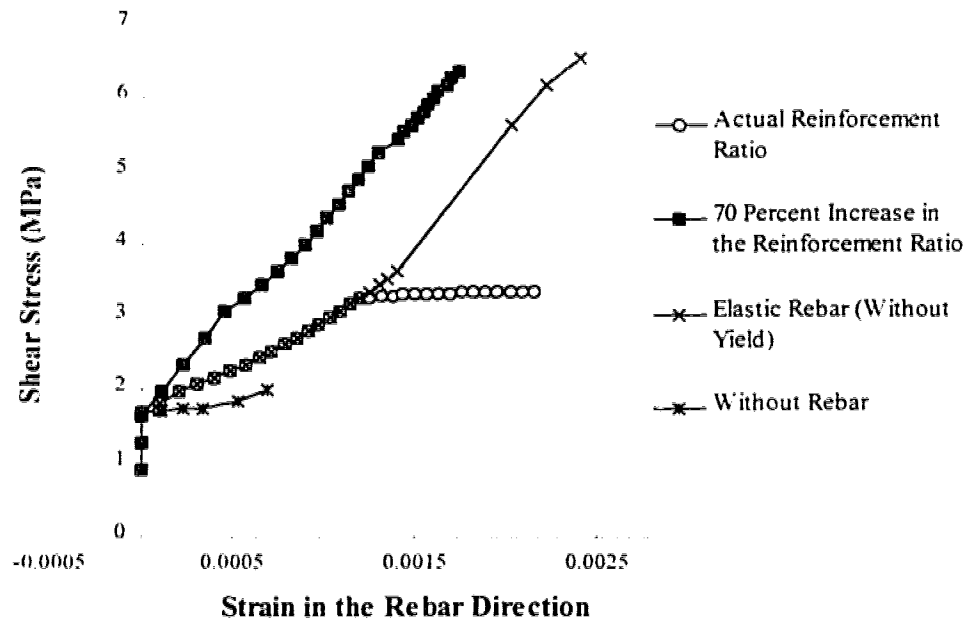


Figure 4.5 - Finite element analysis of PV-4 with different reinforcement ratio

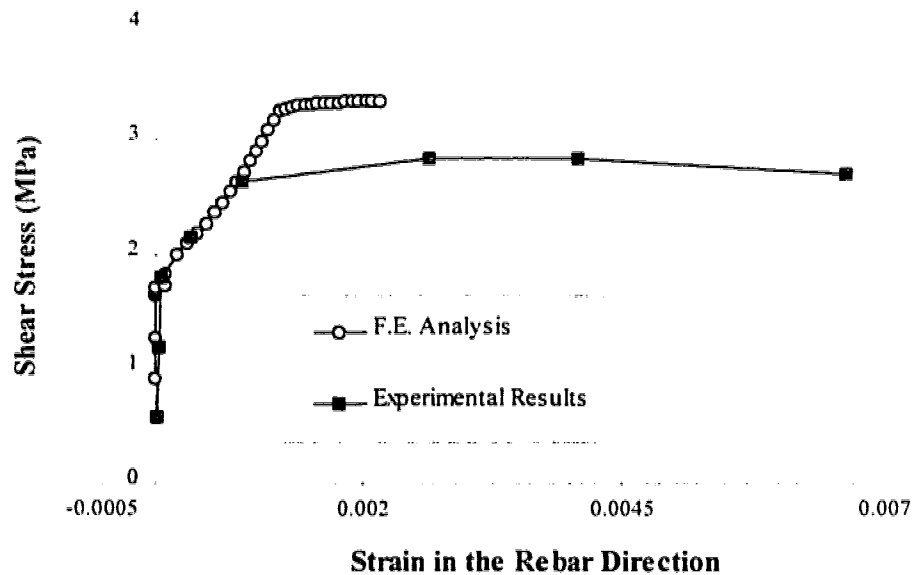


Figure 4.6 - Finite element analysis and experimental results for panel PV-4

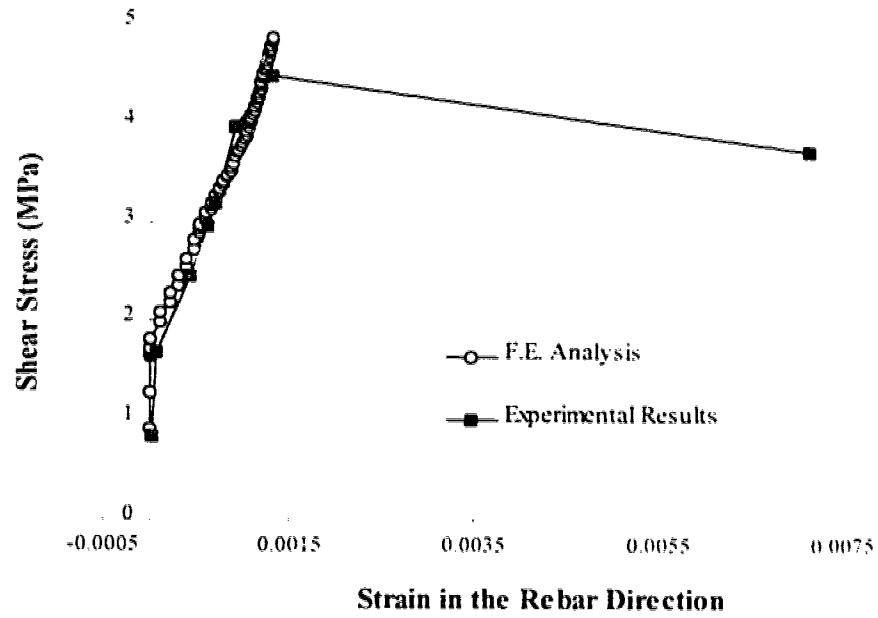


Figure 4.7 - Finite element analysis and experimental results for panel PV-6

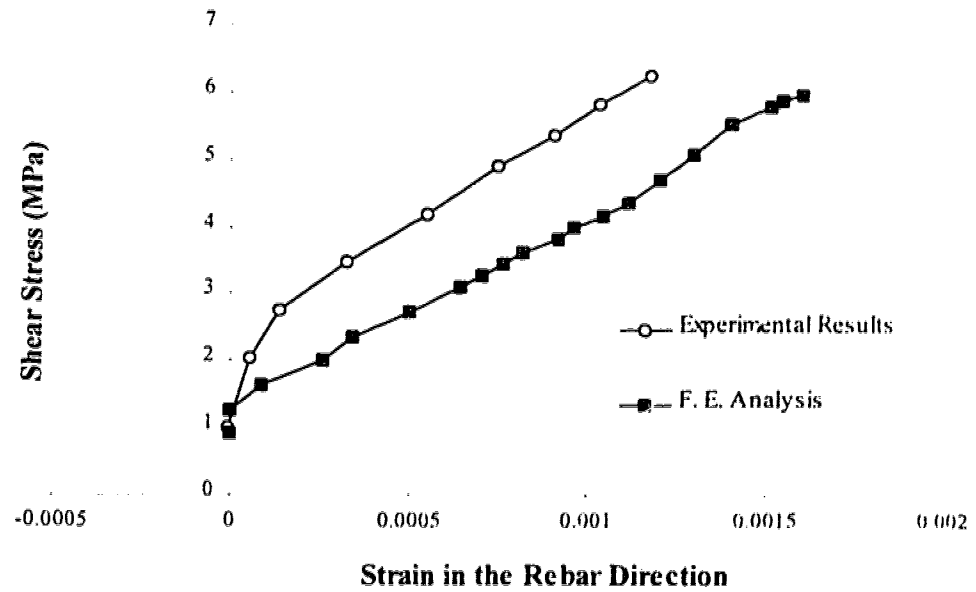


Figure 4.8 - Finite element analysis and experimental results for panel PV-27

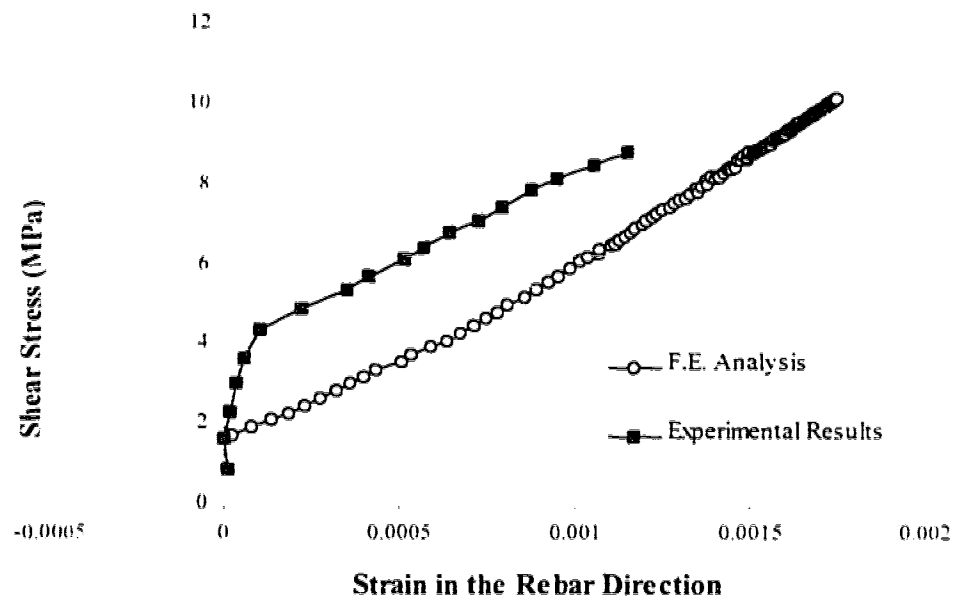


Figure 4.9 - Finite element analysis and experimental results for panel PV-23

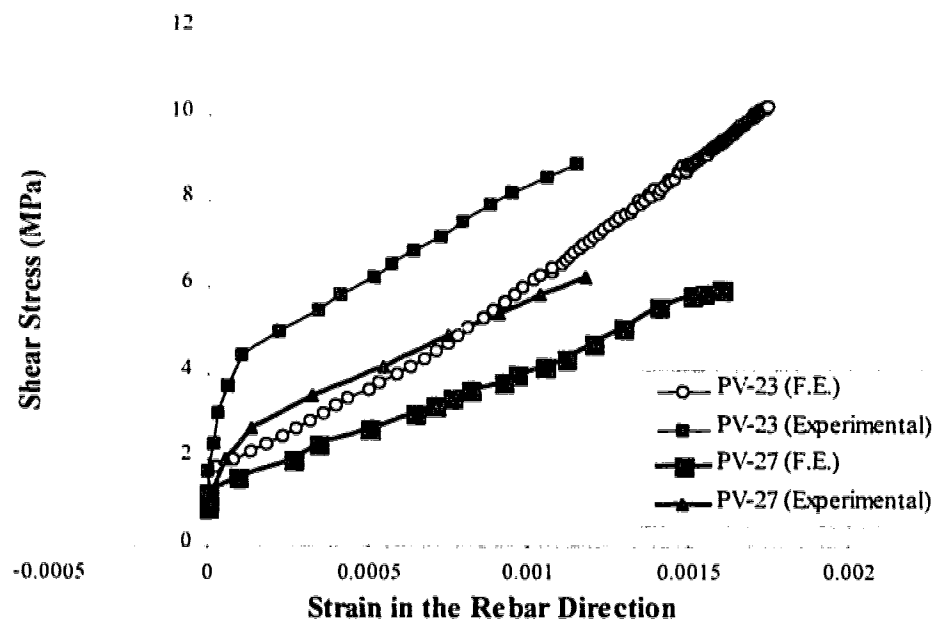


Figure 4.10 - Comparison between PV-23 and PV-27

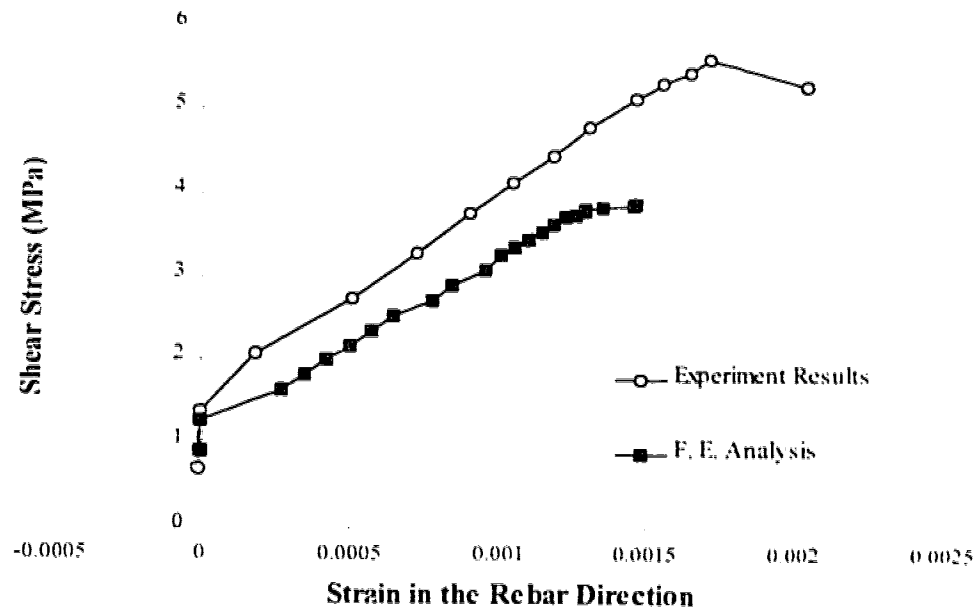


Figure 4.11 - Finite element analysis and experimental results for panel PV-28

CHAPTER FIVE

RESULTS AND DISCUSSION

5.1 Introduction

The behavior of concrete plates and shells in the region of high transverse shear forces depends on the thickness and reinforcement arrangement. The behavior ranges from a brittle mode of failure in short span thick structures to a more ductile behavior in long span lightly reinforced thin plates and shells. In most cases failure initiates by developing localized fracture zones in the shape of cracks followed by extensive crack opening displacement leading to yield of the reinforcement. In other situations crushing of the concrete in the unconfined regions of the concrete continuum takes place under high compressive stresses. The continuum nature of concrete structures is also lost when spalling of the concrete occurs. In other cases loss of bond (slip) between the concrete and the reinforcement is manifested as strain incompatibility between the two elements. The mechanism of failure in some of these cases has not yet been understood thoroughly. An example is punching shear of slab-column connections that is still one of the most controversial subjects in this area (Moe 1961, Regan et al. 1985, Moehle et al. 1988 and Alexander et al. 1992).

The finite element method is an approximate solution technique for continuum medium and in its state-of-the-art formulation, can hardly address the large discontinuities in the strain and displacement field of concrete plates and shells in localized fracture zone. In fact analysis of structure using shell elements cannot provide the required discontinuity in the strain field of the plates and shells to represent inclined single crack pattern in the structure in the high shear force region. This issue was discussed in the previous chapter. However, a qualitative numerical analysis is still

possible and it helps to understand the behavior of these structures and to detect the required ductility and other performance parameters of the structure.

In this chapter the performance of the finite element model developed in the previous chapters is examined in some special cases chosen from the recent literature. To investigate the brittle mode of transverse shear failure in thick and short span plates and shells, a shell specimen which failed in shear in the test process is chosen as the first example. A more recent reinforced concrete slab-column connection test that showed a more ductile behavior is also studied to examine the performance of the numerical model in punching shear problems where yielding of rebars occurs prior to shear failure. The two tests are deliberately chosen to verify the ability of the finite element model and to point out its limitations.

5.2 Description of Specimens

In this section specimens are described and their finite element models are explained.

5.2.1 Shear Failure in Thick Plates

The SP-Series specimens tested by Adebar and Collins (1989) are the first examples to be used in this study to validate the finite element model developed in the previous chapters. The SP-Series is a part of an experimental program carried out at the University of Toronto to investigate some of the characteristics of thick shells in high transverse shear zone. This series included testing of nine shell panels under different combination of transverse shear and in-plane forces. The specimens were of different thicknesses and reinforcement arrangements and were tested in a special test device called "Shell Element Tester" developed specifically for testing shell elements under controlled conditions. Two of these specimens, SP8 and SP3 are chosen in this study for analysis. The main objective is to analyze the SP3 specimen which is loaded solely by out-of -plane shear force. Specimen SP8 with a pure in-plane shear loading is also

analyzed to examine the performance of the finite element model in a uniform shear strain environment.

Both specimens have a standard size of 1524 x 1524 x 310 mm, reinforced in two orthogonal directions in-plane and also in the out-of-plane orientation. The amount of reinforcing steel in both in-plane directions is equal and almost the same for SP3 and SP8 (3.6% in both direction). Rebars are oriented at a 45 degree angle with respect to the side of the specimens. Out-of-plane reinforcement is $800 \text{ mm}^2/\text{m}^2$ and it is the same for both specimens. Figure 5.1 illustrate the cross section of the specimens and their reinforcement patterns. The loading mechanism for out-of-plane shear forces includes equilibrating bending moments applied at the edge of the specimen. Details concerning the material properties and loading of SP3 and SP8 are given in Table 5.1.

The finite element model of the specimens consists of one bicubic shell element for SP8 (distribution of strain is uniform) and four elements for SP3 (to account for bending curvature) as shown in Fig. 5.2. Two concentrated equilibrating moments applied in the same direction at both supports provide the uniform distribution of shear force and a linear distribution of flexural moment in the span direction for SP3 specimen. To generate a uniform in-plane shear stress in the SP8 specimen, in-plane forces are applied on the edge of the specimen. The applied loads and boundary conditions on the finite element model of the specimens are shown in Fig. 5.2.

5.2.2 Slab-Column Connection

A reinforced concrete slab-column connection test is the other example examined in this study. The test was carried out by Afhami, Alexander and Simmonds (1996) at the University of Alberta to study the mechanics of punching shear failure of concrete slab-column connections. This experiment was particularly oriented to investigate the plate-edge column connections. The test specimen consisted of a 10008 x 4270 mm, rectangular concrete slab, 152 mm, in thickness clamped in two 305 by 254 exterior columns and one 305 mm, square interior column. The two edge columns are located

adjacent to and centered along the two short edges of the slab while the interior column is centered exactly at the middle of the slab. The specimen is rotationally restrained along the two longer edges to represent a continuous slab in the width direction. The system and dimensions of the slab are shown in Fig. 5.3. The slab was loaded almost uniformly by spreading the concentrated jack loads on the slab through an articulating distributing mechanism.

To reduce the size of the numerical model of this specimen, the finite element analysis for each slab-column connection (interior and edge connections) was performed separately by applying the appropriate boundary conditions in the finite element model of each connection as shown in Fig. 5.3. The assumption of boundary condition of zero rotation in the width direction is based on the location of zero shear line in one way behavior. In the out of plane direction, the vertical displacement of nodes in the column are suppressed. The finite element model of each connection consists of 16 bicubic shell element as shown in Fig. 5.3. Utilizing symmetry about the longitudinal axis, only half of the connection is modeled. Element "1" in the finite element model is in the column. Imaginary values for material properties were assigned to this element (high rigidity and strength) to make its contribution to the model similar to that of the column. For all the other elements according to the test data, compressive strength of concrete f'_c considered as 34.8 MPa and yield stress of reinforcements f_y assumed as 420 MPa. The exterior edge-column connection is the main objective of this study. The different layers of the reinforcement arrangement for each element in this connection are listed in Table 5.2. The arrangement of reinforcement for elements in the interior connection is listed in Table 5.3.

5.3 Observations in The Analysis

Some of the characteristics of the finite element model developed in this study were identified in the analysis process of the above specimens. These characteristics are classified in two different groups. One relates to the refined shell element, the other relates to the concrete material model.

5.3.1 Refined Degenerated Shell Element in Concrete Structures

Application of the refined degenerated shell elements developed in this study to concrete structures illustrates some important characteristics and limitations of this new element. Simultaneous propagation of cracks in the tension side and softening of the material in the compression side of the cross section in concrete plates and shells reveals the outstanding strain field adjustability of the adopted refinement technique. The element, however, needs some modifications in its integration algorithm across the thickness to compensate for the effect of movement of the neutral axis and decrease in the height of the compression block. Also in nonlinear analysis of concrete plates and shells, the refined degrees of freedom demonstrate sensitivity to the convergence criteria and tolerances adopted for out of balance loads in the solution algorithm. These issue will be discussed in details.

5.3.1.1 Strain Field Idealization

The refined degenerated shell element is distinguished from the other shell elements by its superior strain field idealization, specially in high transverse shear force zones. Finite element analysis of specimen SP3 gives some insight into the mechanism of refinement adopted in this approach and its adjustability to the changing strain field of the structure.

The shear strain distribution at different load steps in SP3 specimen is plotted in Fig. 5.4 at two cross sections, one at the support, the other at one third of the span. These points are shown in Fig. 5.2. The term "*Average transfer shear stress*" in the figure substitutes the term for load level in the structure. Average shear stress indicates the total transfer shear force in the structure (which is constant everywhere in the structure in each load step) divided by the cross sectional area of the specimen. In the initial stage of loading, the concrete is in the elastic range of behavior and the strain distribution is exactly the same as that shown in Chapter 3 where a hypothetical elastic beam was analyzed. A parabolic distribution of shear strain exists at a distance from the support while close to the support, a more uniform distribution of strain prevails. The reason for

this uniformity is that, refined degrees of freedom for parabolic shear strain distribution β have been suppressed at the point of application of concentrated moments to switch off the interaction with the rotational degrees of freedom, as discussed in Chapter 3. From a practical point of view, it could be argued that the introduction of edge moments requires in practice that the top and bottom fibers be clamped or be built integral with some other element that will apply the moment imposing *de facto* that particular constraint at the support.

After initiation of cracks in the top fibers of the specimen, a softening behavior starts in this part of the cross section causing a non-symmetric shear strain distribution across the thickness. This phenomenon becomes more obvious when the crack grows in the depth of the specimen as shown in Fig. 5.4-b for a point far from the support. In a refined element this behavior must be captured by the second component of refinement, λ , introduced in Chapter 2, and represented by the shape function $k(\eta)$ in Eq. 2.10-c. In the analysis, however, this unsymmetric distribution of shear strain for the point close to support is accompanied with a huge nonzero shear strain at top and bottom fibers of the cross section as it is shown in Fig. 5.4-a. Such behavior seems in contrast with the argument in Chapters 2 and 3 that shear strain at the extreme fibers should be close to zero due to the contribution of parabolic shear strain component of refinement, β , represented by the shape function $g(\eta)$ in Eq. 2.10-c.

The involvement of the parabolic shear strain shape function in the solution, appears to be in the opposite direction of that that was expected. This behavior is triggered because of the strain hardening characteristics of concrete in the compression part of the cross section. Cracking of concrete in tension and strain hardening of concrete in compression part of the cross section causes a simultaneous softening response across the thickness from top and bottom while in the mid-cross section material is still stiff. Figure 5.5 visualize shear strain distribution of the cross section for such a case. The only refined shape function to address this characteristic is $g(\eta)$ which is originally meant to represent the parabolic shear strain distribution of the cross section. Nevertheless the

severity of the softening in both top and bottom of the cross section is much higher than the required zero shear strain condition at the top and bottom. As a result, the self adjustability of the finite element method causes a change in the sign of this shape function contributing in the solution, giving the best fit to the actual distribution of the shear strain across the thickness. Figure 5.6 illustrates this phenomenon.

By increasing the value of the material parameter k_0 that governs initiation of yield as defined in Chapter 4, strain hardening of material in the compression side of the cross section will be delayed and simultaneous softening of the cross section starts at a higher load level. Analysis of a simple hypothetical beam, the same as that in chapter 3, illustrates this phenomenon. Figure 5.7 shows the beam and its finite element model. Shear strain distribution of the cross section at a point close to mid-span using two different values for parameter k_0 is shown in Fig. 5.8. As shown in this figure, a higher value for k_0 postpones the simultaneous softening behavior of the cross section to a higher level of load.

Such phenomenon can be described based on the nature of the finite element method and the role of the independent variables. Although the strain field in this case does not satisfy the required zero shear strain at the top and bottom of the cross section, it describes the most accurate distribution of strain, considering the limited number of independent variables in the formulation.

To be able to represent simultaneously the zero shear strain at the extreme fibers and also the softening in both sides of the cross section, a new shape function would be required in the formulation of refined shell element. Figure 5.9 illustrates an example for this function. The function $q(t)$ would provide the shear strain distribution curve with two bumps at the top and bottom to represent the simultaneous softening behavior of the cross section in extreme fibers. The new shape function $q(t)$ relaxes the parabolic shear strain shape function $g(t)$ and allows zero shear strain at extreme fibers.

Another remedy to escape from the nonzero shear strain in top and bottom face of the cross section is to conceive of a hybrid approach in the finite element formulation for degenerated shell elements with a constraint on zero shear strain at top and bottom face of the cross section. Although this technique guarantees a zero shear strain in the extreme fibers in all circumstances, to be able to account for the strain field shown in Fig. 5.5 it still needs the additional shape function $q(t)$ to represent simultaneous softening in the extreme fibers.

5.3.1.2 Integration Across The Thickness

Degenerated shell elements are not necessarily layered. In program NISA-80 integration across the thickness is performed using a Simpson's rule at a user defined odd number of points equally spaced across the thickness. In the analysis of flexural reinforced concrete members, specially in the under-reinforced condition, the compression zone of the cross section could be very small compared to the tension zone. Specimen SP3 gives rise to this condition. Figure 5.10 shows the distribution of the normal strain across the thickness in different load steps in specimen SP3 at a point close to support (tension at the top, compression at the bottom). This distribution is plotted against the Simpson integration point number along the depth of the cross section. Here, obviously an 11 point rule is used. The figure illustrates the migration of the neutral axis towards the compression side of the cross section and the decrease in the depth of the compression block in each load step as the tension side softens (cracks). To have an accurate integration across the thickness, a small compression block is numerically inconvenient specially with the integration scheme adopted in this formulation.

If the number of integration points inside of the compression block becomes too small, the accuracy of the analysis will be affected considerably. The increasing number of integration points in the tension part of the cross section does not contribute to the accuracy of the analysis but is inevitable as a result of moving the neutral axis toward the compression side of the cross section. Since the number and location of the integration points are fixed in the integration algorithm, the decreasing number of integration points

in the compression block will yield an inaccurate estimate of the moment and axial force on the cross section. In some cases the number of integration points in the compression block reduced to two or even one point, causing instability in the solution procedure and renders it unable to reestablish equilibrium in an iterative sense.

As a remedy for this problem, it would be desirable to keep the number of the integration points constant in the compression block regardless of the position of the neutral axis. This elaboration raises two problems. The first one is to find the location of neutral axis and to define the compression block. The second is to realize that, keeping the number of integration points constant in the compression block requires changing the location of these points in each iteration in each load step. This in turn requires an algorithm that interpolates the history of the state variables of the material at the new locations of the integration points in the current load step from the existing information about the previous integration points in the last load step.

5.3.1.3 Sensitivity in The Analysis

The refined degrees of freedom are not the essential degrees of freedom in the structure to establish equilibrium and to find a solution. Their existence, however, helps to reach to a more accurate point in the solution space that is not far from the point reached if the refined degrees of freedom were excluded from the formulation. In other words equilibrium is not affected strongly by the new degrees of freedom and the sensitivity of the solution for them is lower than that for the other degrees of freedom. As a result, in the case of nonlinear analysis when iteration is required to reestablish the equilibrium in the structure, the contribution of the refined degrees of freedom can be invoked properly only if the solution is very close to the absolute equilibrium position. In fact if the convergence criteria and tolerances in the solution strategy is not strict enough to reestablish the equilibrium in each load step properly, the accuracy expected from the contribution of refined degrees of freedom will not be sustained in the analysis procedure.

5.3.2 Concrete Material Model for Plates and Shells

Although nonlinear analysis of concrete structures has been around for decades, there are a number of factors that have prevented wide application of this technique in common practice (Bathe et al. 1989). In fact nonlinear finite element analysis of concrete structures is usually very costly and in most cases requires considerable experience on the part of the user. The high cost of the analysis and the need for an experienced user is largely due to the difficulties encountered in the stability and convergence of the numerical solution procedure. Reliability of the results and accuracy of the solution is another issue that plagues analysts. Drift of the solution and lack of convergence are both rooted in the numerical model of concrete material. Hypoelastic (so called “orthotropic”) concrete models are perhaps less theoretically sound than would be desired, but are mathematically simple and, as a result, in most cases numerically stable. In turn, their accuracy in representing the concrete nonlinearities in the triaxial state of stress is not sufficient. Plasticity models are the other way around. In theory, they are able to represent material nonlinearities in the three dimensional state of stress and are mathematically sound. However, they are not numerically stable due to the complexity involved in implementations of the concrete nonlinearities.

Some of these difficulties in the performance of concrete plasticity material model used in this study are described in this section

5.3.2.1 Concrete Material Model in General State of Stress

There is no uniformity in the stress field of plate and shell structures. It changes from point to point across the thickness as well as in the plane of the element. In the thickness direction, the bending moment causes a tension dominated field on one side and a compression field on the other side of the cross section. The other components of stress, in-plane and out-of-plane shear stresses, also vary across the thickness. In the in-plane direction, close to free corners of the structure, large torsional moments cause large in-plane shear stresses, while close to point loads, out-of-plane shear stresses dominate the stress field. This variety of stress fields in the structure requires a versatile material

model to represent all these situations simultaneously with a unique set of calibration parameters.

Plasticity material model include some parameters that govern the hardening and softening range of behavior (size of the load and potential functions as well as the amount and direction of plastic flow). To determine the material constants that define the rate of change of the hardening and softening parameters a calibration technique must be adopted. Calibration is usually a process based on a well defined experiment in a controlled situation. These type of experiments are difficult to conduct for all ranges and possible combinations of the stress components in the concrete material. The few feasible test results available mostly target the compression dominated state of stress. However, even access to these parameters for different states of stress in the concrete is not practically helpful. In fact it is not easy to use the new parameters conveniently in the analysis because the state of stress in the structure varies from point to point and from step to step in the analysis.

Figures 5.11 and 5.12 illustrate this situation. In these figures, distribution of the transverse shear stress and normal stress across the thickness in specimen SP3 are shown at two integration points in the same element. As the level of load in the structure increases, the state of stress at the integration points across the thickness changes. Sometimes there is a sudden change from compression to tension for those integration points close to the neural axis. By comparing the two graphs (a and b) in each of Figs. 5.11 and 5.12, it is obvious that the state of stress would also be different at any two adjacent in-plane integration points in the same element and it changes from load step to load step. The large variation in the state of stress in a single element indicates that, calibration of the concrete material model for the different states of stress is not a simple matter in the analysis of plate and shell structures.

The nature of the material itself in the regions of tension compression is sensitive. Consider for example Fig. 4.2. in that region, the rapid change of the compressive branch with very little change in the tensile stress is obvious. Yet no test results exist in this

region. The literature contains only uniaxial tension and compression test results and high compression confined test results.

The sensitivity of the analysis to the calibration parameters was obvious in the analysis of almost all of the specimens in the current study. Any slight change meant a different behavior at certain points on the cross section. This in turn affected the accuracy of the result and restricted the application of the plasticity material model to plate and shell structures.

5.3.2.2 Extensive Cracking

High transverse shear forces in plates and shells are usually accompanied with large bending and/or torsional moments as exists in slab-column connections or at free edges. In these highly stressed locations, it happens most of the time that the steel rebars in one direction yield but due to the highly indeterminate nature of the structure, load could transfer to the other directions and the structure can withstand higher loads. In these situations, concrete experiences intensive cracking accompanied with shear stresses originating from the out-of-plane shear forces.

As described in Chapter 4, the concrete material model has some limitations in the case of extensive uniaxial cracking when shear stresses dominate the state of stress (see section 4.4.3.1). In the current study this phenomenon was observed in the analysis of slab-column connections mentioned in 5.2.2. In this case, after initiation of yield in the rebars, material model failed to represent the state of stress at the integration points close to the yielded rebars due to extensive cracking in the concrete. This model does not allow for tension stiffening and yield of the rebars resulted in high strains in the surrounding concrete. The material model reached the end of the effective fracture displacement, u_f and was unable to keep a zero state of stress thereafter. Convergence deteriorated and the analysis was terminated well before the ultimate load was reached.

In the analysis, where reinforcement in point B in Fig. 5.3 yielded, the fracture strain of the material ($\epsilon_f = u_f / h_t$ where h_t is the tensile crack spacing) was 1.16×10^{-3} ,

lower than yield strain in steel reinforcement ($\varepsilon_y = 2.1 \times 10^{-3}$). Wherever the uniaxial strain in concrete passed the limit of fracture strain, the material model representation of state of stress becomes problematic as it is shown in Fig. 5.13. In the last load step strain in steel layer exceeds the yield limit ($2.23 \times 10^{-3} > 2.1 \times 10^{-3}$ in a point between integration points 9 and 10, close to point 9). By proportion, strain in most part of the tension side of the cross section is passed over the fracture strain limit in concrete. Nevertheless, material model in the tension side of the cross section shows mostly compression instead of zero tension. To reestablish the equilibrium, the strain field in the structure changes in an iterative process. As a result, the compression side of the cross section in this integration point was incorrectly unloaded to account for equilibrium in the structure as shown in Fig. 5.13. Considering the rapid progress of the intensive cracked zone in that region, reestablishing the equilibrium in the structure is difficult and analysis could not proceed beyond this point.

5.3.2.3 Sensitivity to The Increment of Strain

Plasticity material models, similar to most other inelastic material models for solids, are history dependent. In other word, the response of the material model is related to the state of stress experienced by the material in previous load steps. In such a model, errors or inaccuracies in updating the state variables in each load step accumulate and become permanent features of the history of the material that cannot be corrected in forthcoming load steps. The Willam and Pramono plasticity model in this study show sensitivity to the increment of strain tensor probably caused by linearization process in tracing the plastic strain history. A rapid change in the strain level introduces inaccuracies in this model which grow in every load step and leads to instability and convergence problems in the analysis. Even a simple compression test in hardening range of behavior, which is known as insensitive case compared to the other possible states of stress, can show the problem. Analysis is carried out using the same shell element with the boundary conditions of pure uniaxial state of stress (only translational degrees of freedom in the plane are free) as shown in Fig. 5.14-a. Compression dominated field is a simple state of

stress and material model has been used successfully before in this range of behavior (see, Xie et al. 1994). The results of the analysis for four different load increments, shown in Fig. 5.14-b, indicates the sensitivity of the material model to the increment of strain. In high level of strain increment, the algorithm implemented in the plasticity material model (to satisfy the consistency provision and to find a new equilibrium position on the yield surface) led the model to a dead-lock. Analysis can not go any further even with a very small strain increment thereafter.

In analysis of plates and shells in high transverse shear force area, a highly stressed zone exists in which after initiation of damage or crack in concrete, strain growth rate increases rapidly. Due to the localized nature of this phenomenon, it is practically difficult to keep the rate of the change of the incremental strain tensor small enough at that special point to prevent inaccuracy in the analysis. Some models have incorporated strain sub-increment techniques that respond to these demands. However, there is really no rational basis in the literature for how small a strain increment should be. The model implemented in this study used a fixed number of strain sub-increments (ten) to trace the strain history at any point in the inelastic range of behavior. Changing that number to “one” did not show any effect indicating that a much larger number is perhaps needed. This was not deemed practical.

5.3.2.4 Numerical Instability

A very important aspect in the finite element modelling of concrete plates and shells is the ability to represent the progressive nature of damage across the thickness. To be able to represent such a phenomenon, a material model must be able to accept rapid changes in the state of stress from compression to tension dominated fields when damage passes through the integration point. In hypoelastic material models damage is based on a crack, its orientation and the concrete properties in the crack process zone. In this case, updating the state variables needs only a simple mathematical transformation. In plasticity models such a problem requires a rapid change in angle of similarity θ (sometimes more than 40 degrees) in π -plane in a single load step. To find a new position

of the yield surface satisfying the consistency provision, the return algorithm to the yield surface must be quite sophisticated (considering hardening, softening and nonassociated characteristics of the model) to accommodate such a big changes in the angle of similarity θ . The angle of similarity is a stress invariant defined as:

$$\theta = \frac{1}{3} \sin^{-1} \left[\frac{-3\sqrt{3} J_3}{2(J_2)^{3/2}} \right]$$

in which J_2 and J_3 are the second and third deviatoric invariants. In the Willam and Pramono model, θ varies from -30 to $+30$ degrees. The first limit corresponds to a tensile state of stress while the second limit to a compressive state of stress. A zero θ denotes a pure shear state of stress.

In finite element analysis of the above mentioned specimens, the shear stress distribution across the thickness was not a smooth function, similar to the strain distribution. As an example, consider the shear stress distribution of specimen SP3 at the point close to support shown in Fig. 5.11-a in comparison with the shear strain distribution shown in Fig. 5.4-a. The strain distribution is always a smooth function because it is constructed from smooth shape functions $f(t)$, $g(t)$ and $k(t)$ as described in Chapters 2 and 3. The stress distribution, however, is a product of two components, the strain distribution and the material properties. If the distribution of stress is not a smooth function across the thickness, material property is the only reason why. Hypoelastic concrete material models, similar to that developed by Massicotte et al. (1990), mostly render a smooth distribution of shear stress across the thickness compared to plasticity material models. In fact the simplicity in implementation of concrete nonlinearities in hypoelastic models removes the sensitivity of the material model to the rate of change in the strain tensor, resulting a gradual and mild rate of change in the state of stress.

The jagged shape of distribution of stress across the thickness in plasticity model becomes more severe when the level of load on the structure comes closer to the ultimate value as can be seen from Fig. 5.15 and 5.16. The state of stress sometimes jumps

suddenly to a new equilibrium point far from the previous position. Figures 5.17 and 5.18 show the distribution of stress across the thickness for consecutive load steps in two different cases. The strain distribution in these cases are still smooth functions and the jump in stress distribution comes only from material model.

The history of the angle of similarity has been traced in the π -plane at two cross sections for specimen SP3 as shown in Fig. 5.19. There are jumps and irregularities in the history of θ for some of the integration points across the thickness.

In the compression side of the cross section, integration point No. "1" for example, a very smooth and gradual change in the value of θ exists as shown in Fig. 5.19-a and b. Concrete in these integration points is in a compression dominated state of stress changing from elastic to strain hardening phase. In fact concrete has never reached to the softening phase in this analysis and this is the main reason why a smooth change in the value of the angle of similarity exists in these integration points. However in the tension side of the cross section, points No. "11" and "9" in Fig. 5.19-a and b, there is an irregular and zigzag behavior in the history of θ as shown in the figure. Initiation of crack in the plasticity material model can interpret as a sudden switch from elastic or hardening phase to the softening range of behavior. Material model obviously cannot sustain a smooth rate of convergence to stick to the shrinking yield surface in this range. Degradation of concrete in the softening range of behavior follows a very sharp descending slope which is hard to capture properly by the numerical algorithm implemented in the current version of the material model. The performance of the material model can be improved in the softening range of behavior by adopting a more sophisticated return algorithm to the yield surface. The new algorithm must be capable of handling large gradient of changes in the potential function representing the shrinking yield surface.

Integration points in the middle of the cross section are in a more complex state of stress, a combination of shear and normal stresses. By progression of damage in the tension side of the cross section, shear stress shifts upward to the compression side of the

cross section as shown in the integration points No. “4” and “5” in Fig. 5.19-a and b where the value of angle of similarity θ for these points get closer to the pure shear axis ($\theta=0$). The change of θ is smooth with a decided shift to the tension phase of the state of stress. In fact neutral axis is moving toward the compression side of the cross section and the state of stress in those points is changing to a tension dominated field accordingly. For the integration points located in the compression side of the cross section, reduction of compression by movement of the neutral axis means to shift from a confined compression dominated state of stress with a ductile hardening behavior to a tension-shear dominated field with a brittle softening behavior. When the state of material hits the failure surface in this case, a softening behavior starts which is not as smooth as the one in the hardening phase, the same as that described in the previous paragraph.

For integration points No. “4” and “5” in Fig. 5.19-b located in a point close to support, the dominance of tension stress is quite obvious after neutral axis passed them and they get into the tension side of the cross section. The irregularities in the history of θ in these points are similar to the integration points No. “9” and “11” in the tension side of the cross section as discussed before. However, integration points No. “4” and “5” in Fig. 5.19-a have shown big jumps in the value of θ which cannot consider as irregularities. Although the state of strain and stress in these two points are very close to each other before the jump, after the jump they behaved differently.

The difference between the behavior of the points at the 1/3 of span (Fig. 5.19-a) with the same points in location close to support (Fig. 5.19-b) is related to the proportion of normal stress in the combination of stress components. In the point at 1/3 of span, the dominant stress is shear and softening behavior starts very close to the pure shear state of stress. It seems that, material model in this case (softening in pure shear) not only can not sustain a gradual change in the angle of similarity but, it is in a very unstable condition. In fact, depending on a slight difference in the initial state of stress, material model discharge itself to a more stable situation in the compression or tension phase of behavior. The new stable point in the state of material physically can not happen in this structure as

shown in Fig. 5.16-b and 5.18-a and is an indication of numerical instability in the material model in the pure shear state of stress.

The error introduced in the material model because of the instability will remain in the history of the material in that integration point as shown in Fig. 5.20. This was one of the main reason of the convergence problem in the analysis as was observed in the analysis of SP3 specimen.

5.4 Prediction of The Response of The Specimens

In this section the performance of the finite element model in predicting the behavior of the specimens in the zone of high transverse shear forces is qualitatively investigated and compared with the actual test results.

5.4.1 Shear Failure in Thick Plates

The main objective in analysis of the SP-Series is to investigate the performance of finite element model where out-of-plane shear force is the main cause of failure. In the testing process of specimen SP3, a transverse shear failure occurred prior to yield in the longitudinal rebars, making the specimen desirable for the purpose of this study.

Although in the previous chapter panels subjected to pure in-plane shear were analyzed and their results were discussed, analysis of specimen SP8 loaded in pure in-plane shear forces is carried out in this chapter for the sake of comparison. The two specimen SP3 and SP8 are very similar and it is important to know if the finite element model with the same calibration parameters in material model can represent both in-plane and out-of-plane shear behavior of the structure.

In this study the effect of confinement provided by transverse reinforcement in the specimen has not been included in finite element model. The amount of confinement is restricted to the yield limit of transverse reinforcement. Transverse confinement in this case can build up to about 0.4 MPa which is not a significant amount of confinement, but

it might be the main reason why the numerical model for SP3 slightly underestimates the ultimate value of the failure load.

Analysis of SP8 specimen under pure in-plane shear forces yields an ultimate value for shear stress equal to 16.08 MPa very close to the actual test value of 16.8 MPa. Results indicate a good correlation with the test and justifies the calibration parameters used in material model of this example. The inplane shear stress versus principal strain in the specimen is compared with the actual test results in Fig 5.21. Although it seems that the numerical model could not grasp the actual behavior of the specimen, the analysis results is very similar to the PV-Series specimens (PV-4, PV-6 and PV-27) in the pervious chapter. In fact the method of application of inplane shear force to the SP8 is different from that in PV-Series specimens (as shown in Fig. 4.3 and Fig. 5.2) and the difference in the behavior of this specimen compared to PV-Series in the test is probably because of the load application problem. In finite element model, however, there is no difference between the method of application of inplane shear forces and both of them are exactly pronounced the same effect on the numerical model.

SP3 specimen is subjected to out-of -plane shear forces and its equilibrating bending moments as it is shown in Figs. 5.1 and 5.2. The crucial regions in this structure are the points close to the support where a large bending moment accompanies the shear force. The finite element model prediction for ultimate shear capacity of the specimen is 1.513 MPa compared to the actual test value of 1.72 MPa. In the analysis, long before any sign of flexural failure ($f_c^{max} = 34. < f_c' = 50$, and $f_s^{max} = 230. < f_y = 480$. MPa) the numerical model locked in the convergence problem and analysis couldn't proceed thereafter. In this case the numerical inaccuracy and instability described in 5.3.2.4 was the main cause of the termination of the analysis.

Figure 5.22-b shows the predicted load deformation response of the structure compared to the actual test result. The term “*Tangential Deviation*” in that figure is described in Fig. 5.22-a. The test shows almost a ductile behavior in the structure which is not the case in the analysis as it was discussed before. Also there is no other indication

in the test results to show ductility in the specimen before failure. In fact it is hard to imagine such a ductile behavior in a thick and short span structure. The flat part of the load deformation curve in the test result could be because of the localized effect of the grip mechanism on concrete at the edge of the specimen.

Although the prediction for average transverse shear stress was only about 1.5 MPa, the maximum local transverse shear stress at some of the integration points across the thickness was as high as 5. MPa as shown, for example, in Fig. 5.15-a. This value of shear stress is quite high for unconfined concrete in the thickness direction if, for example, it compares to the value suggested by CAN3-A23.3 M84 for average shear strength of concrete ($0.2\sqrt{f'_c} = 0.2\sqrt{50} = 1.4 \text{ MPa}$). The high value of localized shear stress across the thickness indicates that the analysis was terminated because of the shear failure and it automatically rules out the other possibilities for the failure mode in the structure. Considering the fact that, in the ultimate load level the stress in the longitudinal rebars and also normal stress in concrete was well below the yield or crushing limits, strengthening this argument.

For comparison, another analysis was carried out, using the orthotropic hypoelastic material model developed by Massicotte et al. (1990). In this case the finite element analysis estimation for failure load passed the actual value for the strength of the specimen by a wide margin (2.12 compared to 1.72 MPa.). The Massicotte model predicted a more ductile failure mode by giving 50% more strain in the longitudinal reinforcement compared to the analysis based on plasticity model. This is typical of all orthotropic material models in attempting to analyze shear critical reinforced concrete problems (Balakrishnan et al. 1988). The Massicotte model is two dimensional. Out-of-plane shear components do not enter the material model. Only the out-of-plane modules of rigidity is changed to match that of the in-plane shear value. This shows the invaluable importance of a three dimensional material model when a large out-of-plane shear stress exists in the structure.

5.4.2 Slab-Column Connection

Due to localization of stress and disintegration of the structure in the punching shear zone of slab-column connections, a reliable finite element analysis of punching shear in concrete slabs is very complicated and has not been conducted properly so far. In fact, the structure is not a continuum in the punching shear zone where damage in that region destroys the bond between steel and concrete and inclined single cracks propagate throughout the thickness. Finite element analysis is a continuum approach in nature and to be able to solve this problem, it needs a very significant modification as discussed in Chapter 4.

A finite element model of a slab column connection in its traditional form (smeared crack continuum approach) can be used to qualitatively analyze the punching shear problem. Using refined shell element to address the complicated strain field of the structure in that region is one of the improvements in this approach (see, for example, the work by Klein 1986). Another improvement in the traditional form of finite element analysis of this region is to use a three dimensional material model capable of representing the state of material in softening range of behavior. The finite element model developed in the previous chapters theoretically covers both of these two improvements in the analysis techniques and it was decided to try it in the slab-column test described in 5.2.2.

Nonlinear analysis of the specimen for the edge-column exterior connection and for the interior connection, proceeded with a constant rate of convergence up to the yield limit of the reinforcement. Beyond this limit, the analysis became unstable and couldn't go much further. Extensive cracking in the presence of high shear stresses in the vicinity of the yielded rebars is the main cause of the instability in the analysis as shown in 4.5.3.1 and discussed in 5.3.2.2. The upper limit value for load carrying capacity predicted in the analysis for exterior connection was 10 kPa, almost 55% of the actual test result. In the interior connection, however, a limit of 14 kPa was reached, about 78% of the test value. Figure 5.23 compares the predicted load deformation response of the

structure with the actual test result at point *C* in the slab (see Fig. 5.3). The analysis obviously could not show the most important part of the load deformation history of the structure but its results is comparable to the actual test results in the range of analysis.

Although there is not much to say about the performance of the finite element model in this study, it shows a good resemblance with some aspects of the test results, specially in the edge column connection.

The analysis of the edge column connection shows that, the shear force transfer to the edge strip (elements No. 2,3 and 4 shown in Fig. 5.3) is much less than shear force transfer to the interior strip (element No. 5,9 and 13 shown in the same figure) connecting edge column to the interior column. Adjacent to these strips, the resultant of the shear force intensity along the lines *MM'* and *NN'* (shown in Fig. 5.24-a) is given in Fig. 5.24-b for the last load step. According to the test results, only a fraction of shear force, about 10% , passes through edge strip to the column and the main shear carrying mechanism in the slab is via interior strip. This is in accordance with finite element analysis. The integral of shear intensity along line *NN'* between column face and point *N* on the center of column in Fig. 5.24-b represents the shear force transfer to the column by interior strip. This is considerably higher than the shear force transfer via edge strip (by integration of shear intensity along line *MM'* from point *M* to the column face) to the column.

In the test, a back calculation of torsional moment in the slab along the face of edge strip and interior strip (line *MM'* and *NN'* in Fig. 5.24-a up to column face) shows opposite sign for torsional moment in these strips. The intensity of torsional moment along these two lines (*MM'* and *NN'*) in the analysis, shown in Fig. 5.25, indicates the same result. In last load step (load level 10 kPa) integration of torsional moments intensity up to the face of column yields almost the same value of torsional moment for each direction but in different sign. In fact analysis shows the mechanism of the behavior of the structure in which torsion on the side face of the edge strip reduces the shear capacity of that strip compared to the interior strip in which torsion increases the capacity of the strip (Afhami, Alexander and Simmonds 1996).

In the test, the reinforcement parallel to and adjacent to the interior strip did not show considerable contribution in carrying the negative moment of the slab. The same concept observed in the analysis. Figure 5.26 shows stress in the outer layer of steel bars parallel to the interior strip in the elements on the edge strip (line NN' in Fig. 5.24-a). Analysis predicts yield of rebars in the interior strip(element No. 2) with a sharp decline in the stress level in reinforcement outside of that strip(element No. 6).

Although punching shear failure of the slab-column connection has not been adequately simulated in this numerical model, the mechanism of load transfer in the slab after initiation of crack and up to yield of the rebars has been identified in the analysis. Propagation of damage in the slab up to 55% of ultimate load, reduces the indeterminacy of the structure and the load path in the slab will not change considerably till punching shear failure.

For a point close to the column face, shear stress distribution in the slab at different load steps is shown in Fig. 5.27-a. The same structure was analyzed again, this time with ordinary shell elements (instead of refined version of the shell element). Figure 5.27-b illustrates the shear stress distribution for the same integration point in this analysis. Comparison between the two figures reveals the importance of application of refinement in strain field of concrete plates and shells in high shear zone. Shear stress distribution in the direction parallel to the interior strip for point A (shown in Fig. 5.3) is different in both analysis. First, a large nonzero value for shear stress exist in the compression side of the cross section in the analysis with the ordinary shell element. Second, analysis with the refined element exhibits a fast shear stress growth rate at the beginning of loading but this rate slowed down later in the analysis as shown in Fig. 5.27-a, comparing stress distribution in load level 1 and 4 kPa. with that of load levels 7 and 10 kPa. In the analysis with ordinary elements, however, the rate of change of the shear stress is different as illustrated in Fig. 5.27-b. In fact two different history for shear transfer in the structure was found in the analysis with refined elements and ordinary elements.

Analysis using refined elements terminates slightly sooner at a lower load level. In fact the estimate of stress becomes closer to the critical value in the material model (due to a more accurate strain field in the element) and causes material instability earlier than that in the application of ordinary shell element.

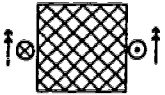
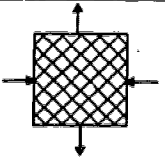
Specimen	Applied load	Concrete properties		In-Plane Reinforcement				Transverse Reinforcement		
		f_c' MPa	ϵ_c'	$\rho_x = \rho_y$	f_y MPa	f_u MPa	ϕ	ρ_z	f_y MPa	ϕ
SP3		50	0.0022	0.0358	480	660	20	0.0008	460	8
SP8		53	0.0021	0.0375	536	637	20	0.0008	460	8

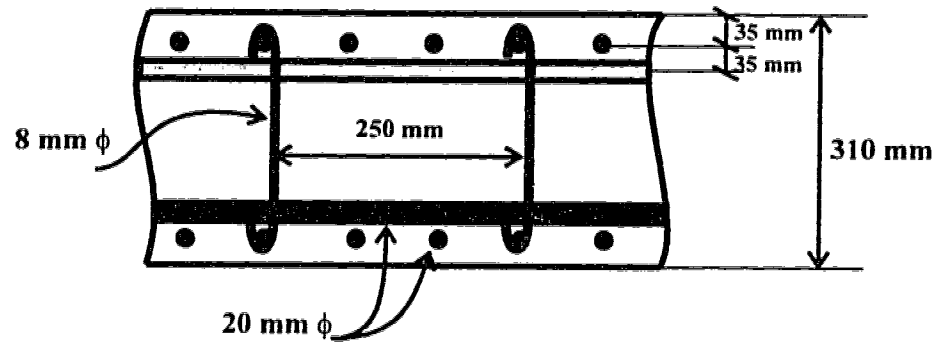
Table 5.1 - Material properties and loading mechanism of the SP panels

Top (W-E)		Top (N-S)		Bottom (W-E)		Bottom (N-S)	
Effective depth 106 mm		Effective depth 122 mm		Effective depth 113 mm		Effective depth 125 mm	
Element No.	Area (mm ²)	Element No.	Area (mm ²)	Element No.	Area (mm ²)	Element No.	Area (mm ²)
2,3	334	5,9	300	2,3,4	250	5,9,13	124
5,6,7	334	2,6,10	500	5,6,7,8	82	2,6,10,14	206
9,10,11	1202			9,10,11,12	293	3,7,11,15	620
				13,14,15,16	375	4,8,12,16	650
Total area of steel 1870 mm ²		Total area of steel 800 mm ²		Total area of steel 1000 mm ²		Total area = 1600 mm ²	

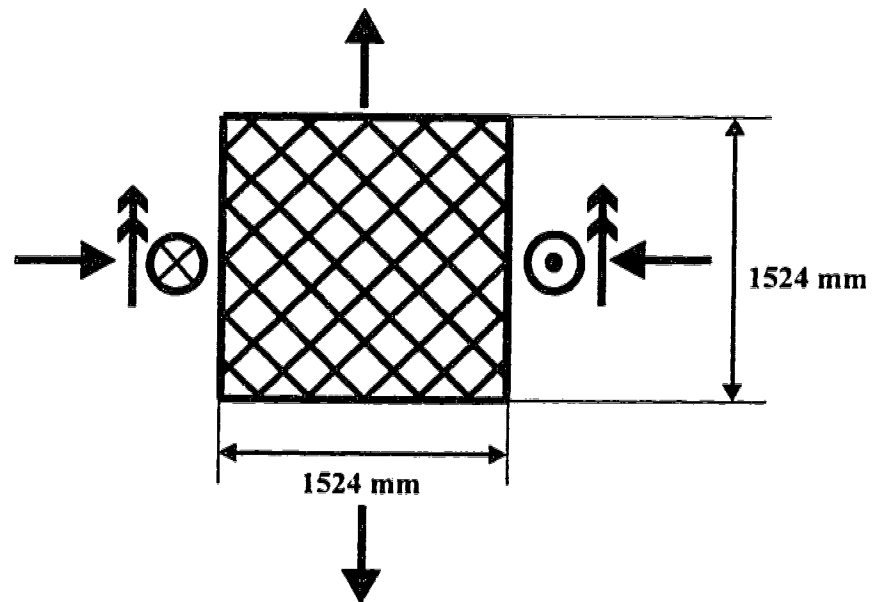
Table 5.2 - Reinforcement arrangement of the Afhami et al. edge slab-column connection

Top (W-E)		Top (N-S)		Bottom (W-E)		Bottom (N-S)	
Effective depth 106 mm		Effective depth 122 mm		Effective depth 113 mm		Effective depth 125 mm	
Element No.	Area (mm ²)	Element No.	Area (mm ²)	Element No.	Area (mm ²)	Element No.	Area (mm ²)
2,3	209	5,9	209	2,3,4	250	5,9,13	250
5,6,7	346	2,6,10	348	5,6,7,8	82	2,6,10,14	71
9,10,11	1245	3,7,11	1043	9,10,11,12	293	3,7,11,15	212
				13,14,15,16	375	4,8,12,16	367
Total area of steel 1800 mm ²		Total area of steel 1600 mm ²		Total area of steel 1000 mm ²		Total area = 900 mm ²	

Table 5.3 - Reinforcement arrangement of the Afhami et al. interior slab-column connection

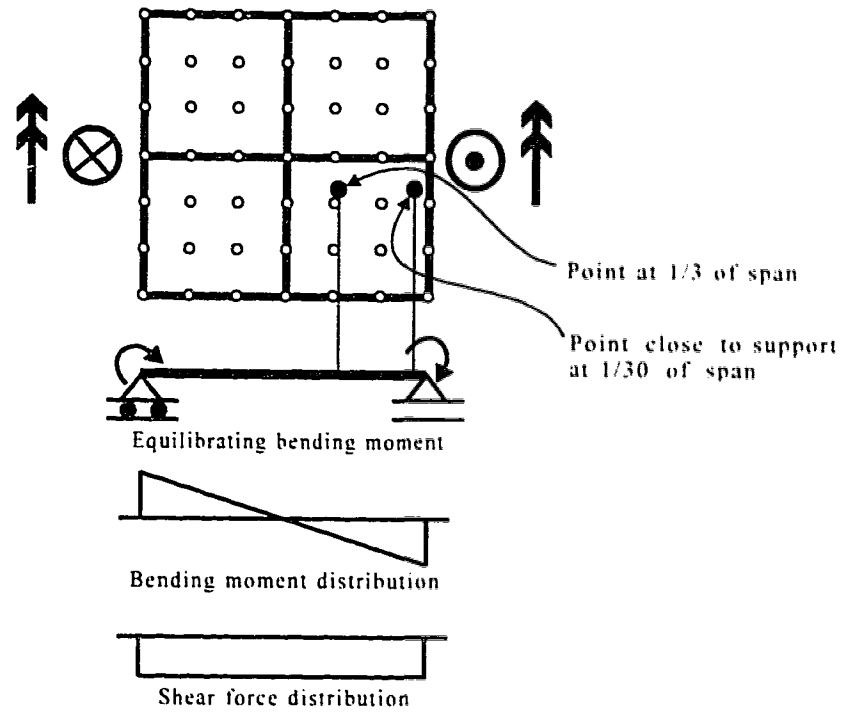


a- Cross section (SP3 and SP8)

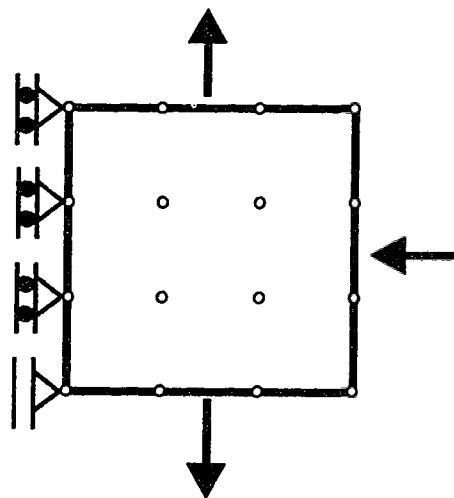


b- Reinforcement pattern and loading mechanism (SP3 and SP8)

Figure 5.1 Cross section and reinforcement pattern of the SP specimens



(a)- Finite element model for SP3



(b)- Finite element model for SP8

Figure 5.2 Finite element of SP-Series specimens and their loading mechanism

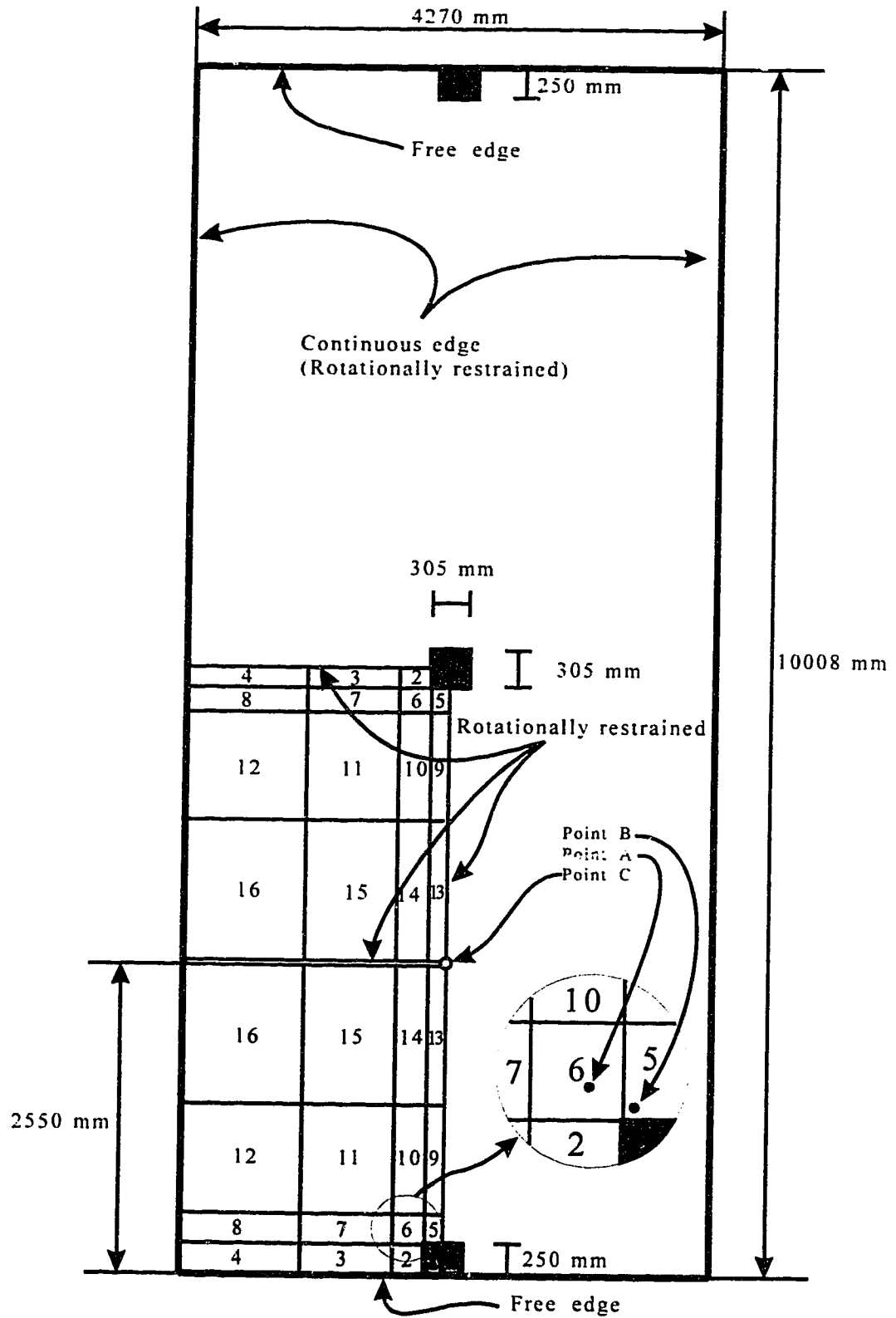
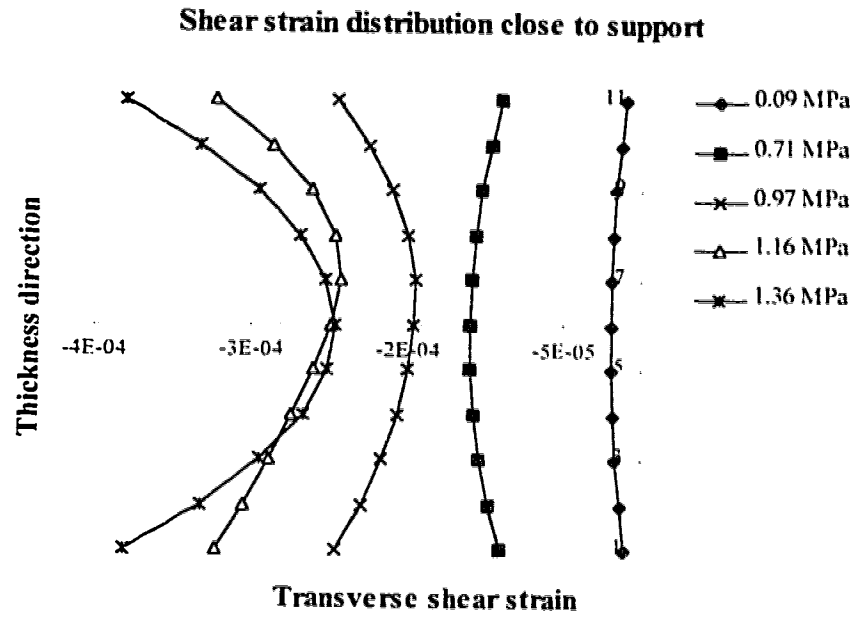
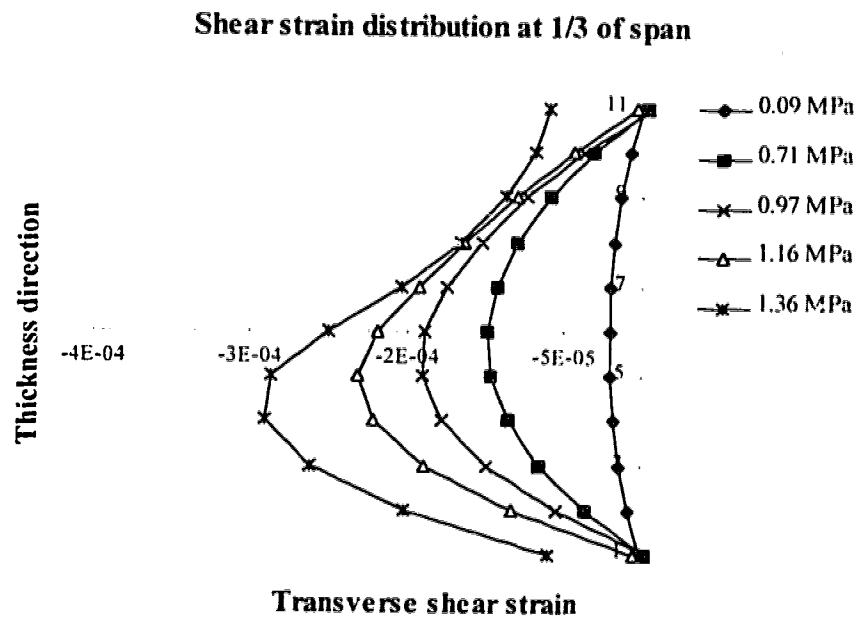


Figure 5.3 Finite element model of the Afhami et al. slab-column connection



(a)



(b)

Figure 5.4 Transverse shear strain distribution across the thickness in SP3
(legend describes average transverse shear stress)

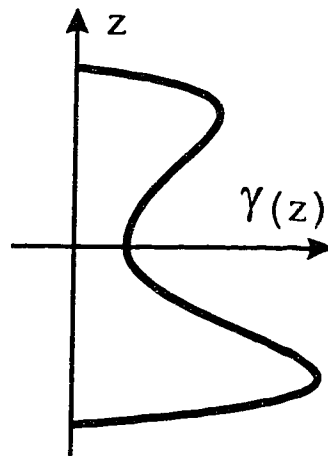


Figure 5.5 Shear strain distribution in the case of simultaneous softening of the cross section at top and bottom

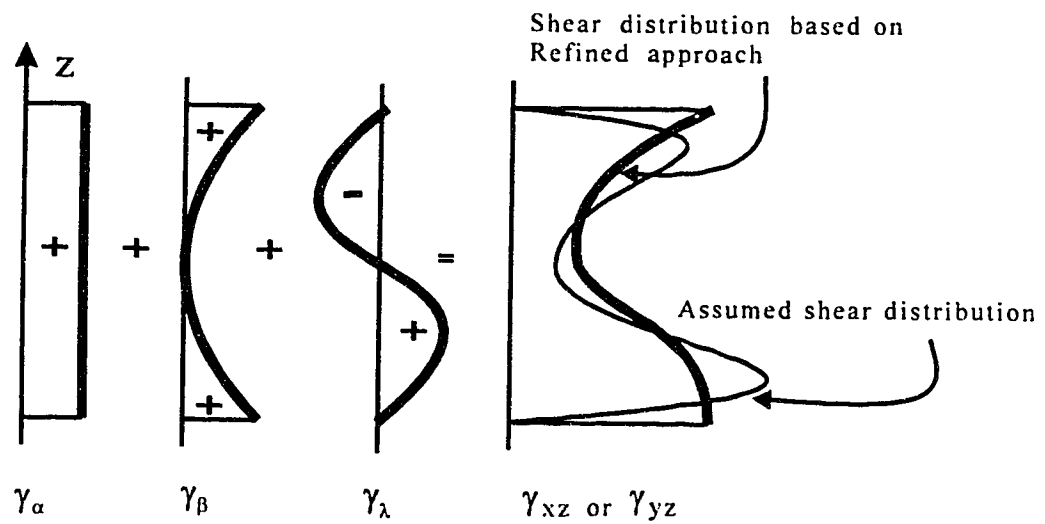
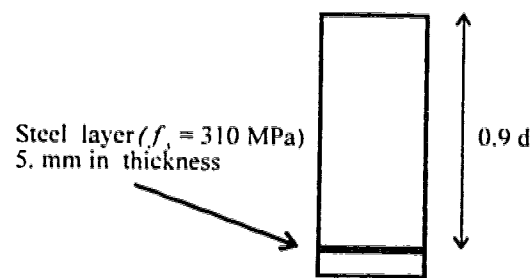
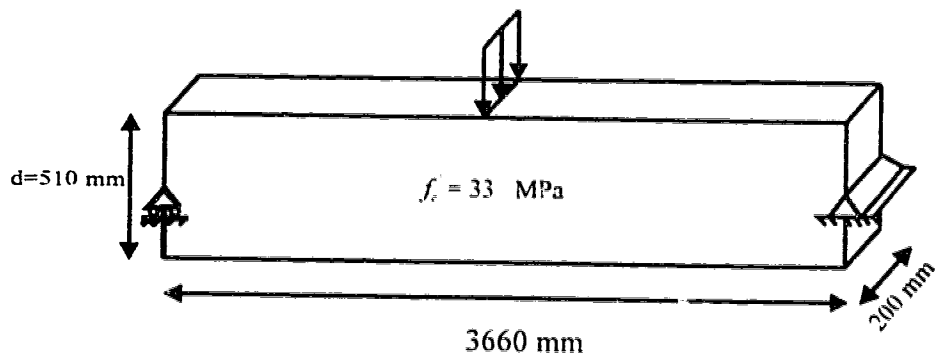
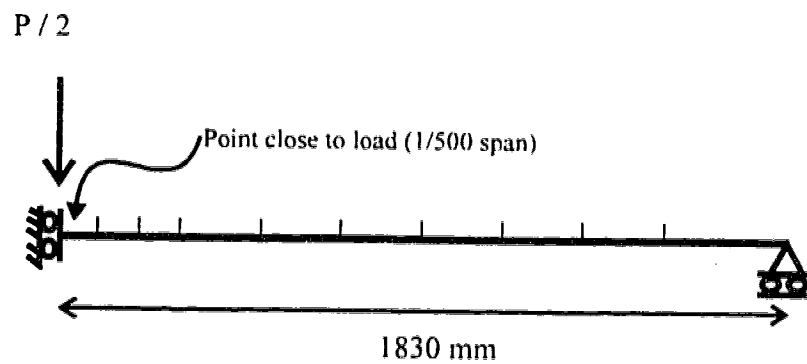


Figure 5.6 Shear strain distribution constructed based on refined approach

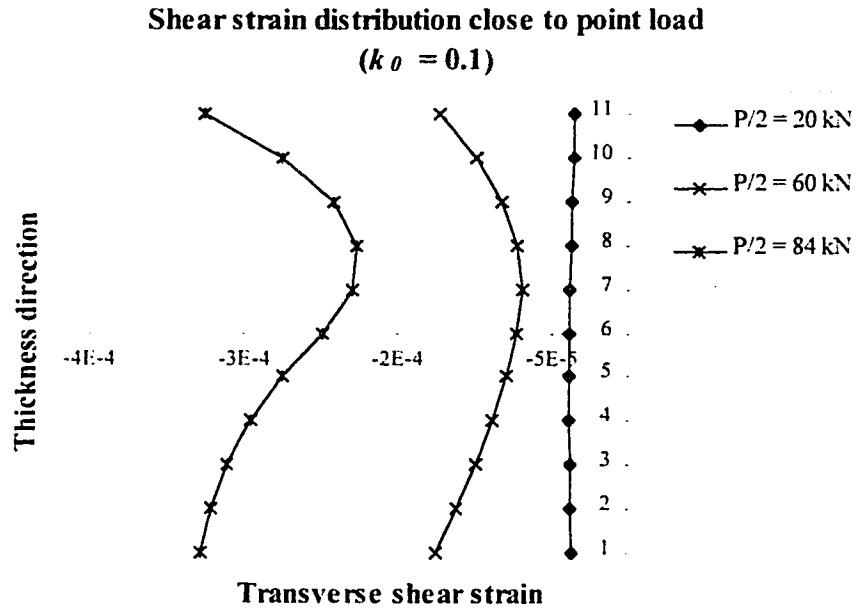


(a)- Beam cross section and loading

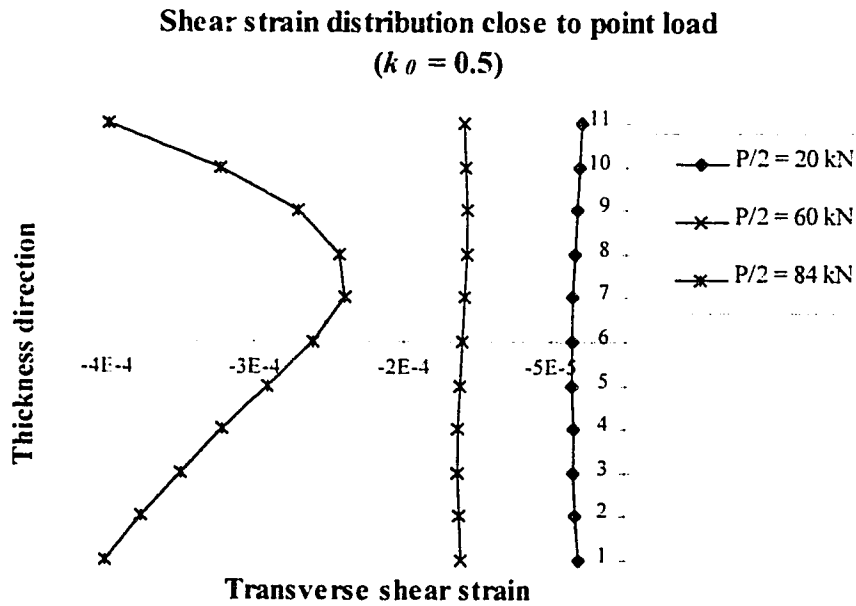


(b)- Finite element model with 10 elements

Figure 5.7 Refined shell based finite element model of a deep beam



(a)



(b)

Figure 5.8 Transverse shear strain distribution in deep beam with different k_0

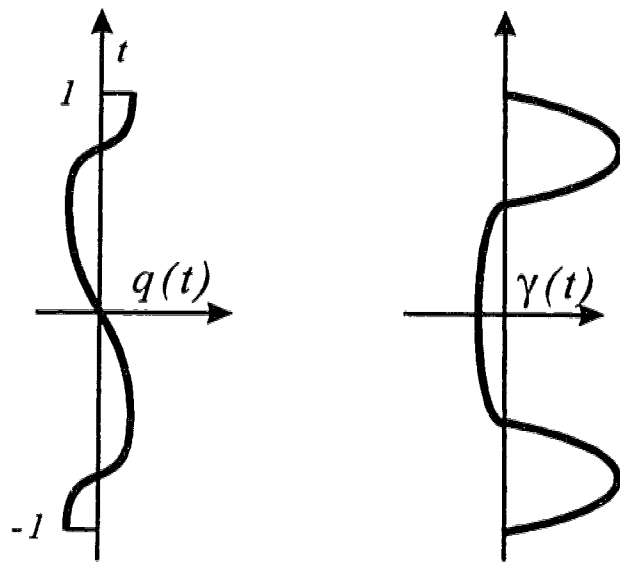


Figure 5.9 Proposed shape function for simultaneous softening at extreme fibers with the associated shear strain distribution

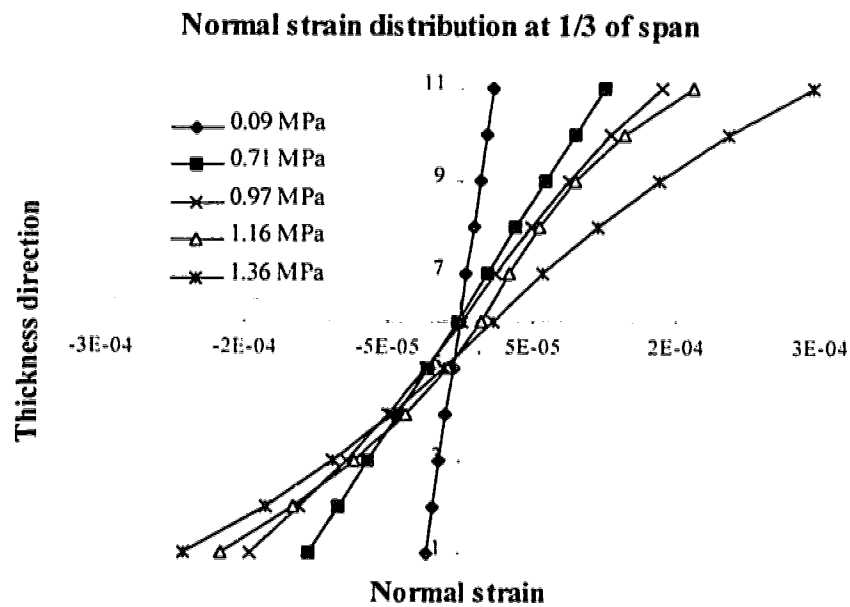
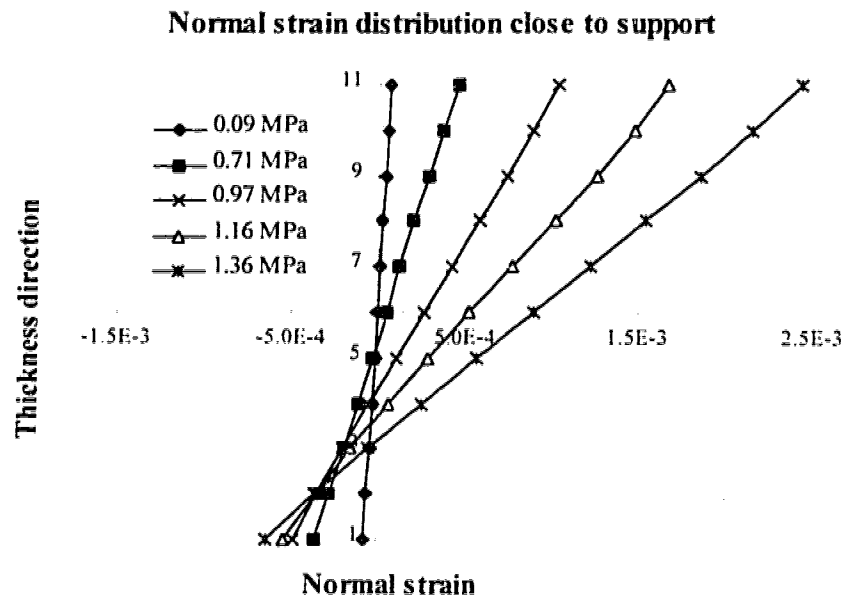
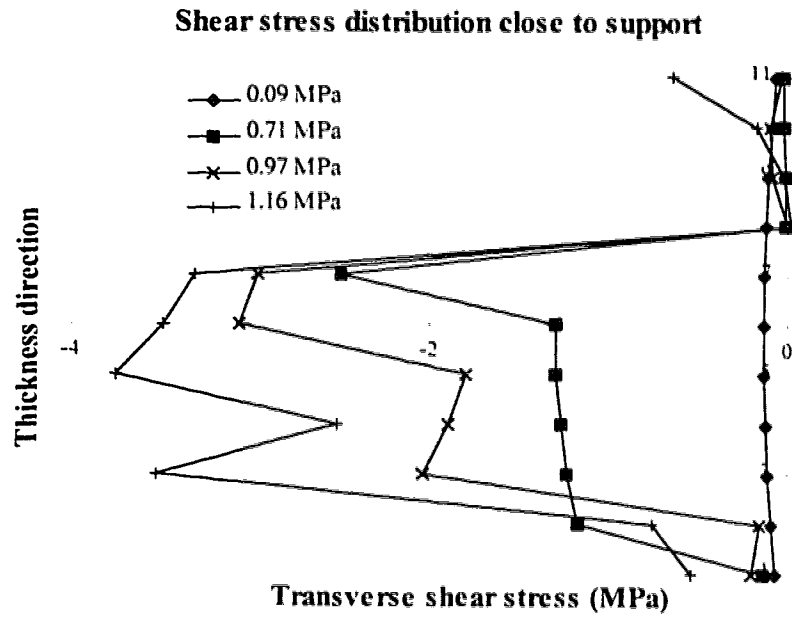
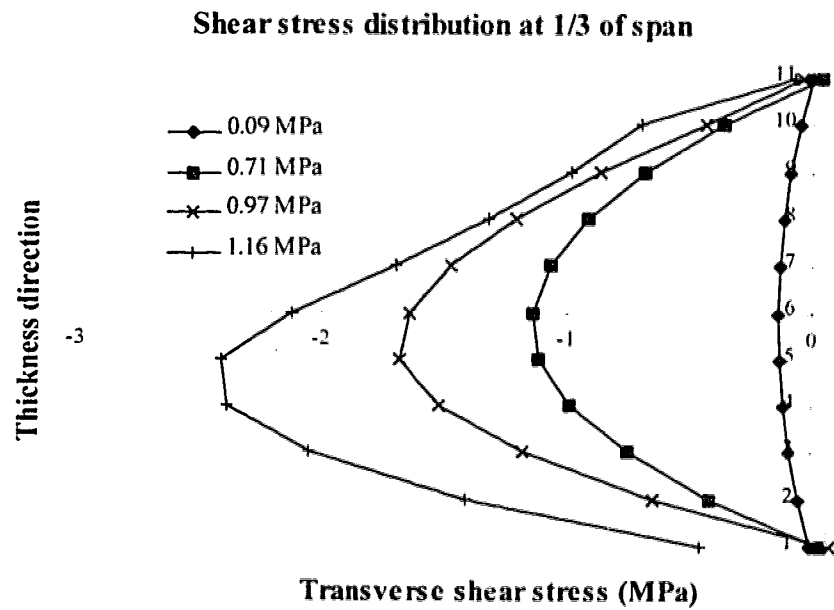


Figure 5.10 Normal strain distribution across the thickness in SP3 specimen
(legend describes average transverse shear stress)



(a)



(b)

Figure 5.11 Transverse shear stress distribution across the thickness in SP3
(legend describes average transverse shear stress)

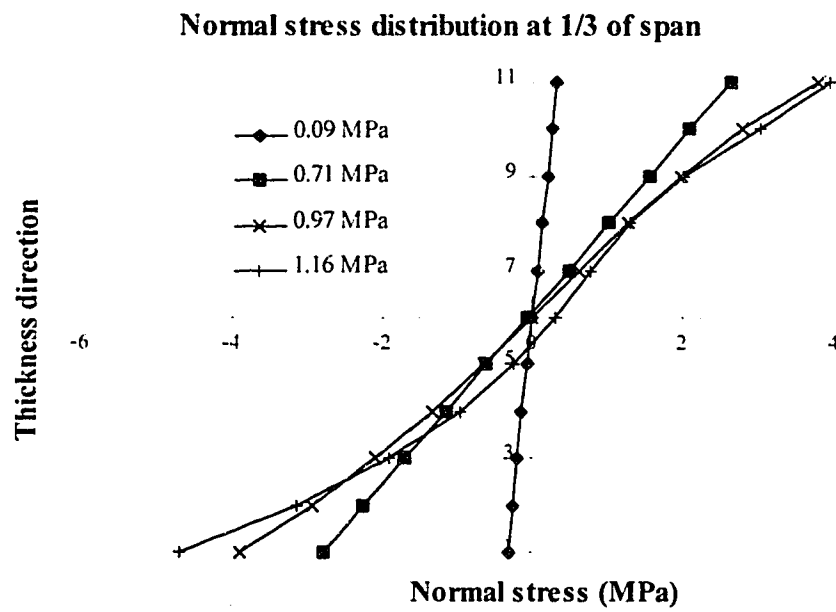
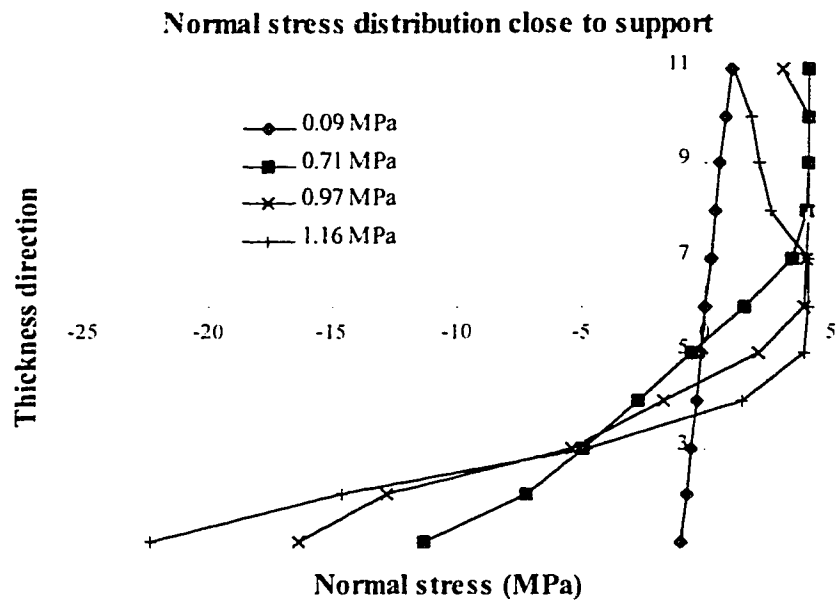


Figure 5. 12 Normal stress distribution across the thickness in SP3 specimen
(legend describes average transverse shear stress)

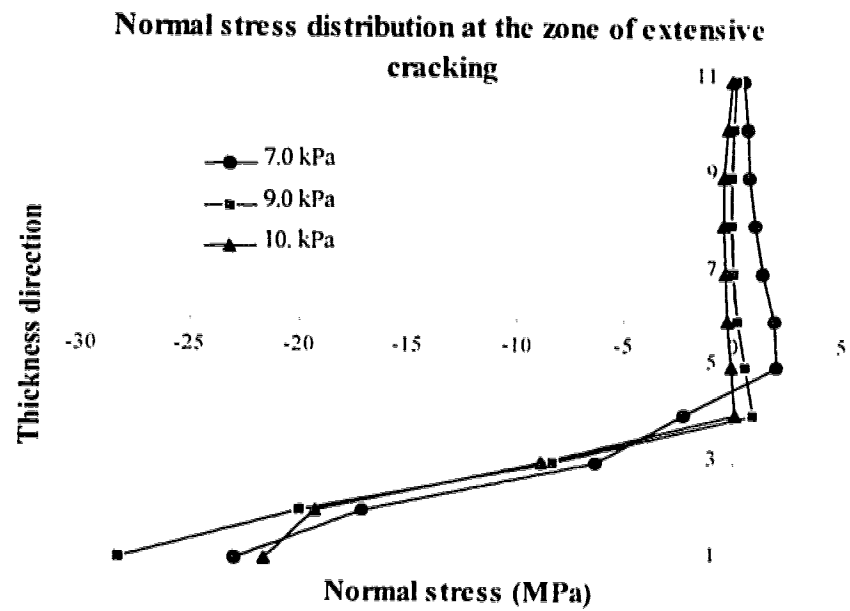
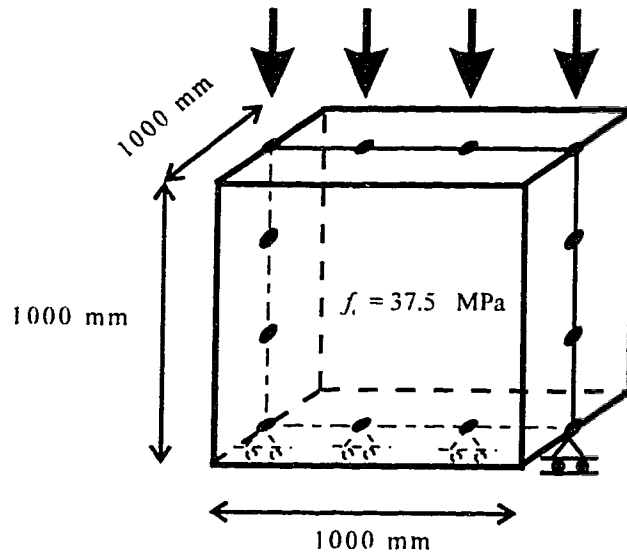
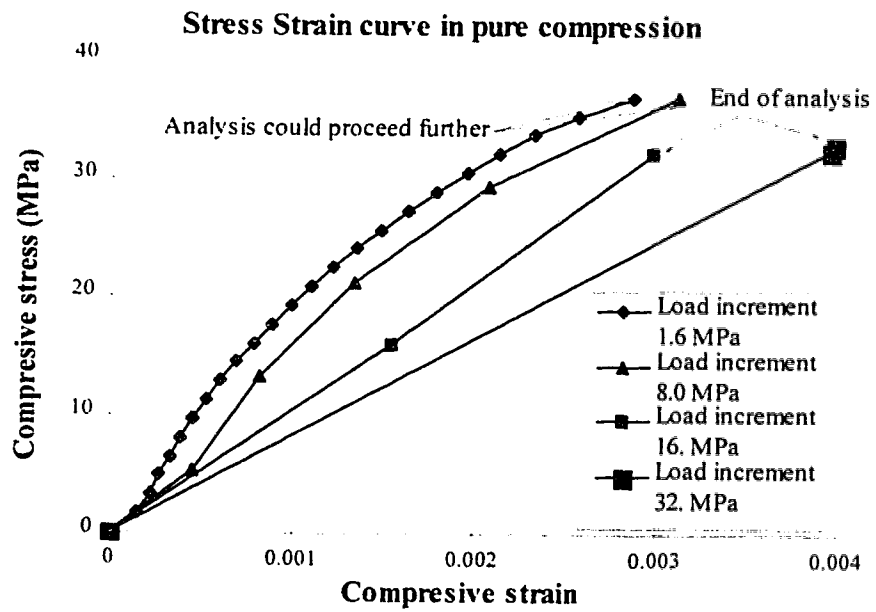


Figure 5.13 Distribution of normal stress across the thickness at a point close to column face in the Afhami et al. slab-column connection



(a)- Finite element model for compression test using shell element



(b)

Figure 5.14 Sensitivity of concrete material model to the increment of strain

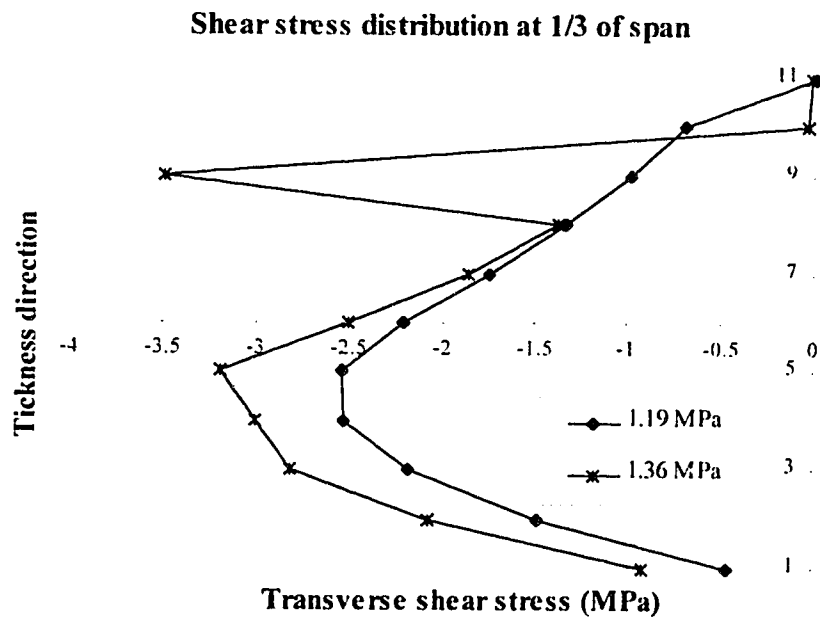
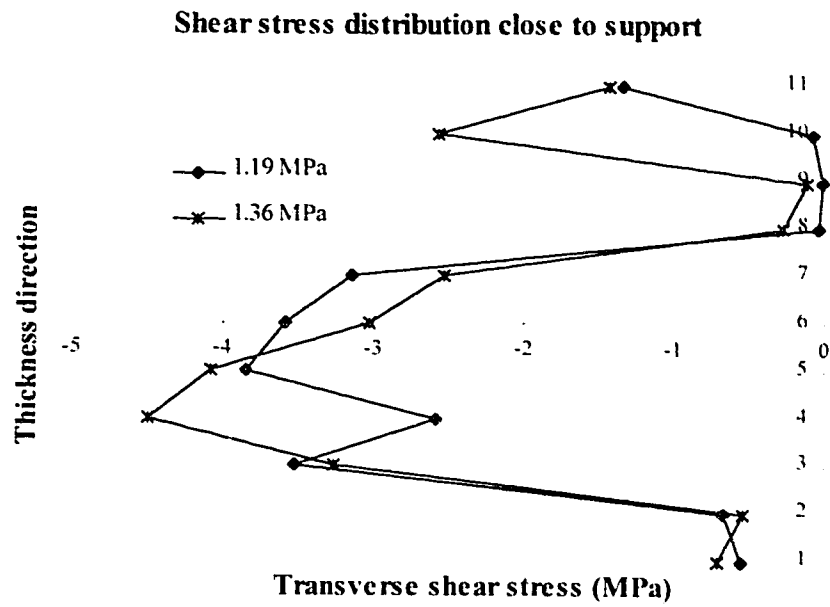


Figure 5.15 Shear stress distribution across the thickness in SP3 at high load level (legend describes average transverse shear stress)

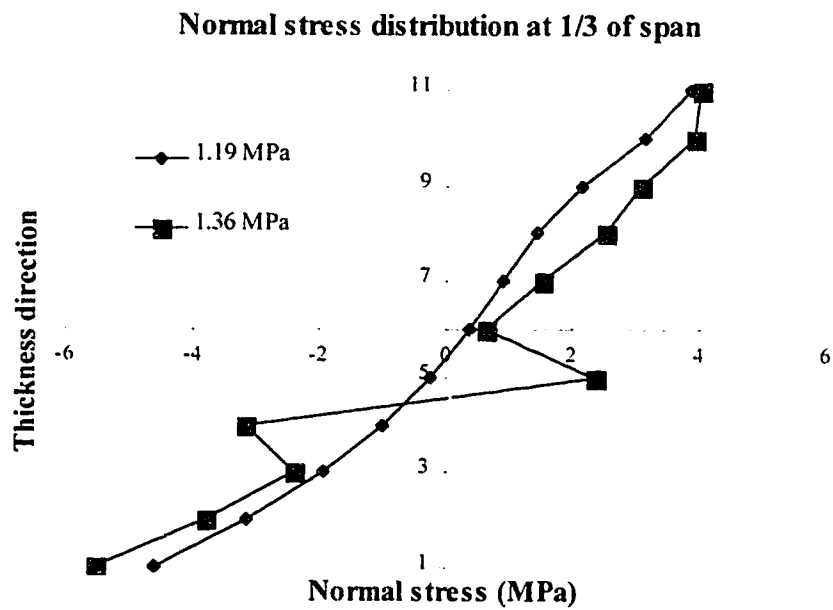
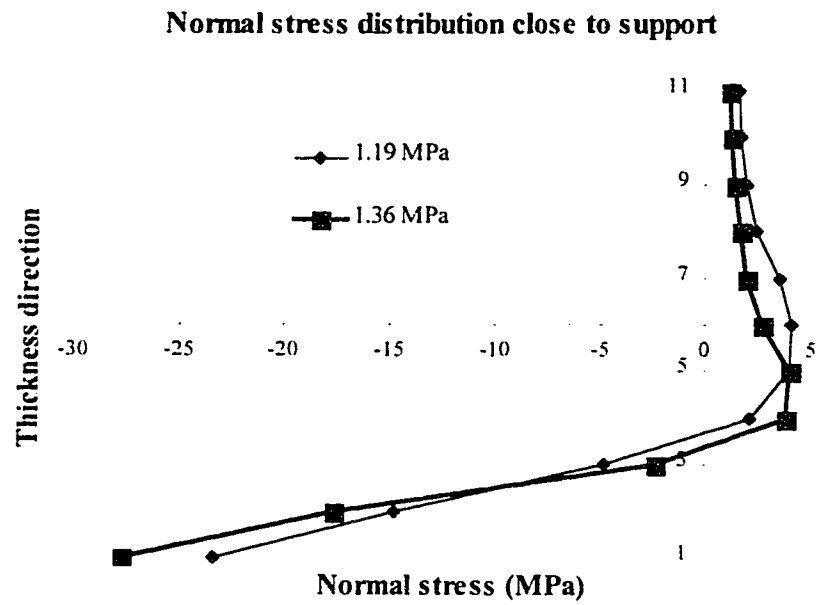


Figure 5.16 Normal stress distribution across the thickness in SP3 at high load level
(legend describes average transverse shear stress)

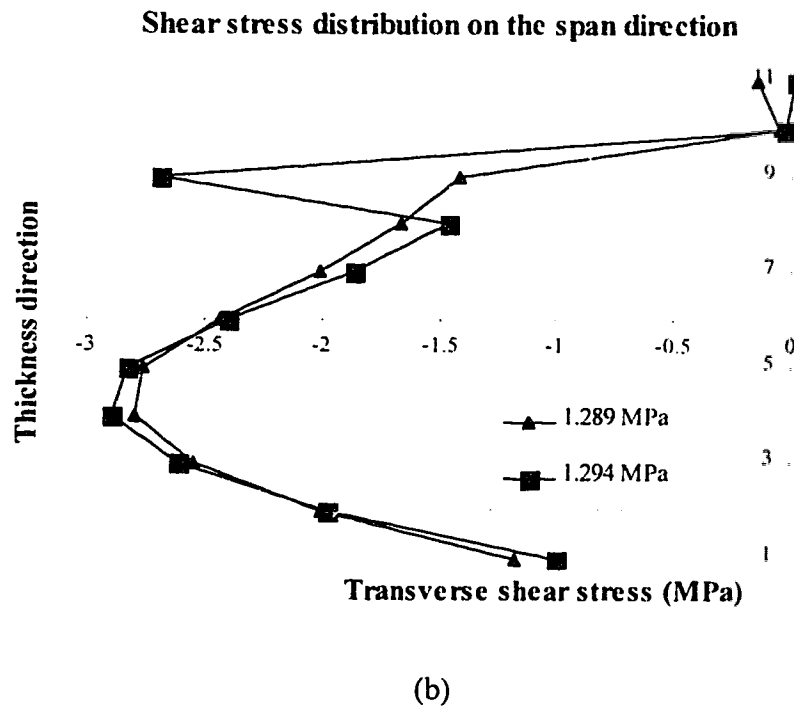
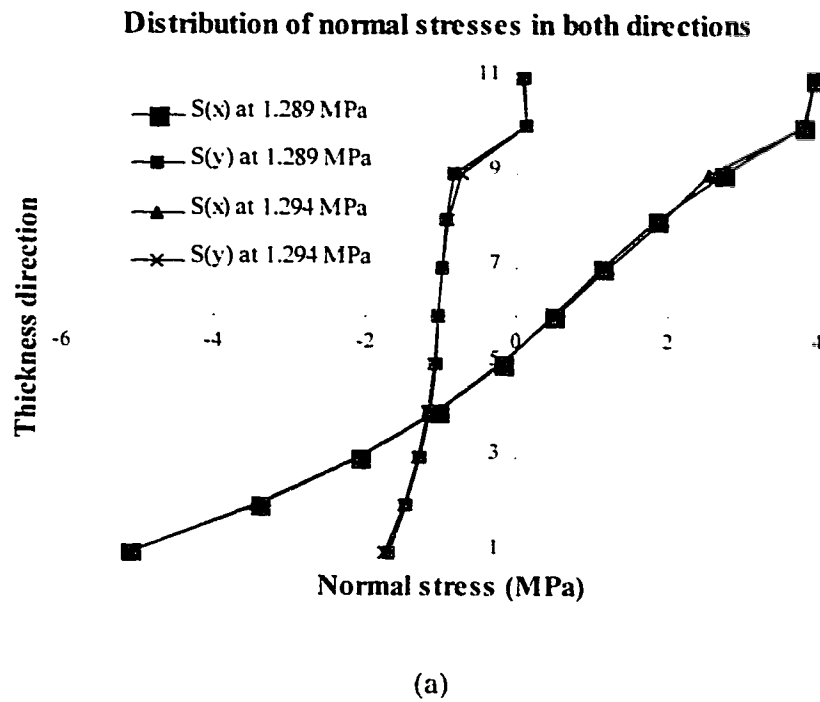


Figure 5.17 Normal and shear stress distribution in SP3 at two consecutive load steps (legend describes average transverse shear stress)

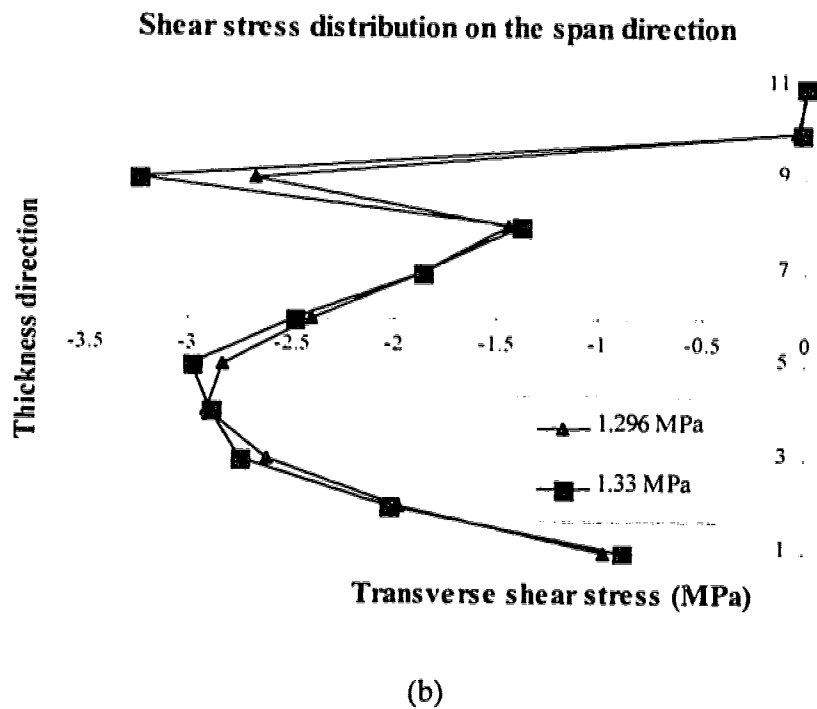
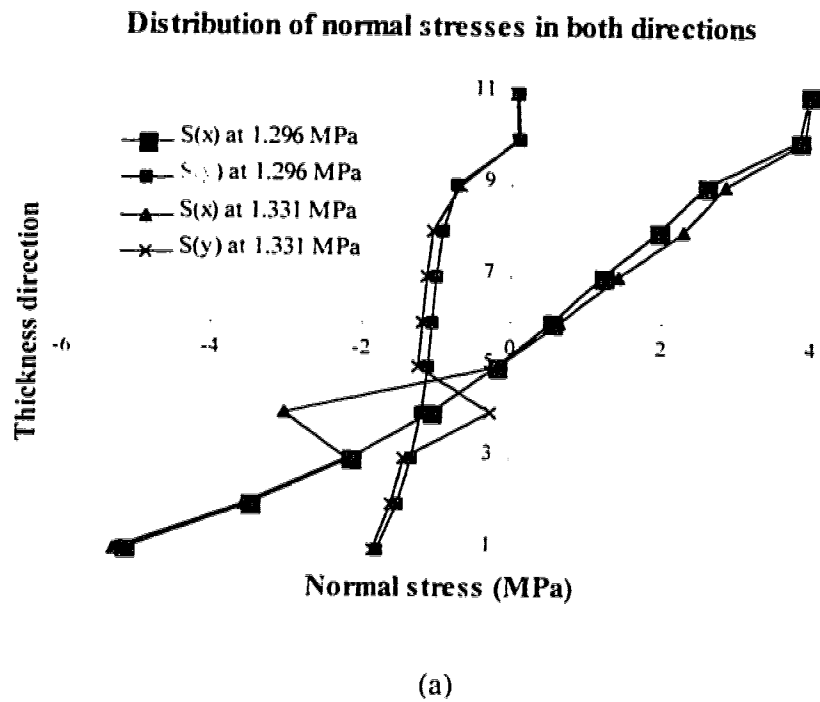
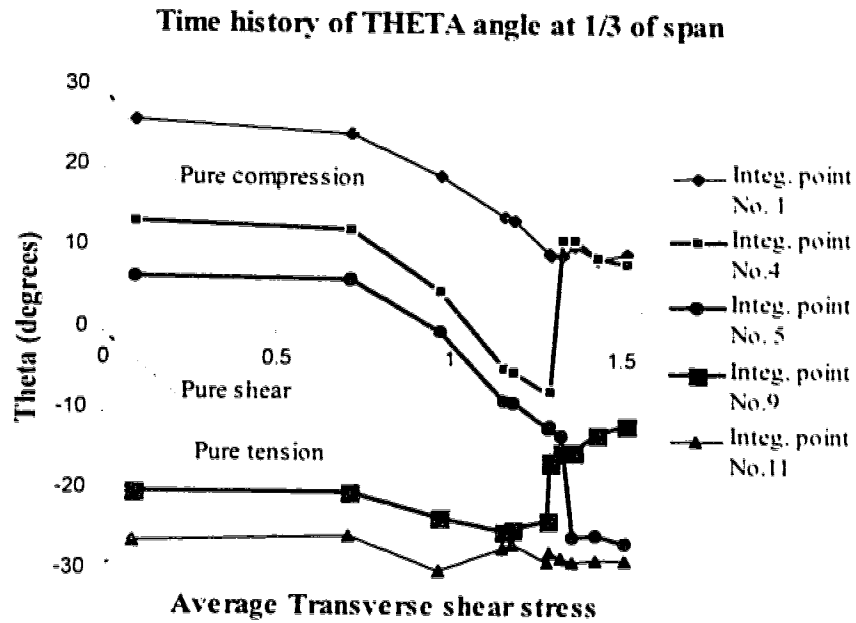
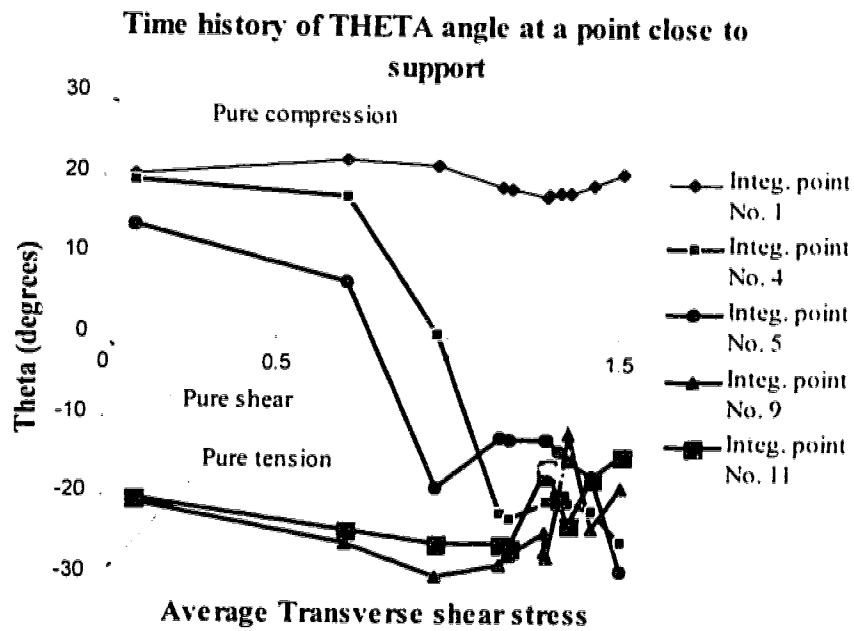


Figure 5.18 Normal and shear stress distribution in SP3 at two consecutive load steps (legend describes average transverse shear stress)



(a)



(b)

Figure 5.19 Time history of angle of similarity in SP3 for points across the thickness

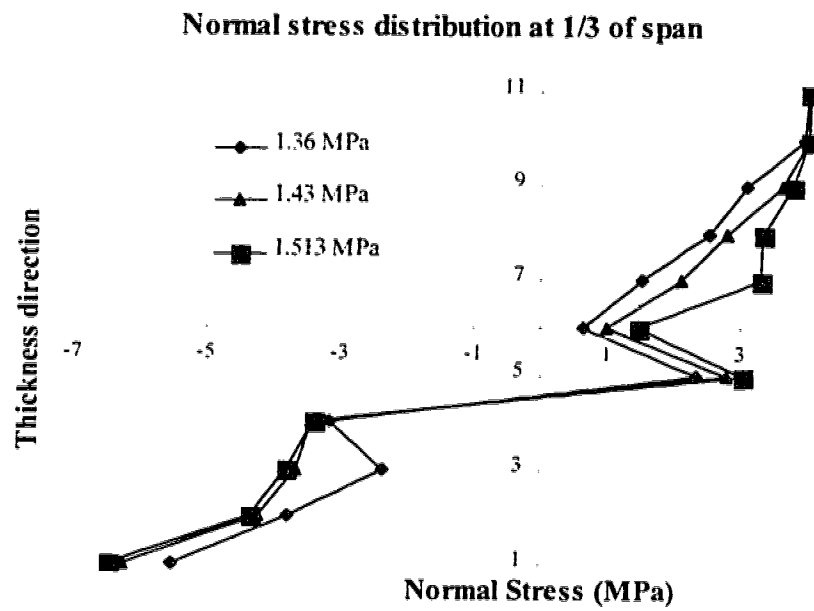


Figure 5.20 Normal stress distribution across the thickness in SP3 at high load level (legend describes average transverse shear stress)

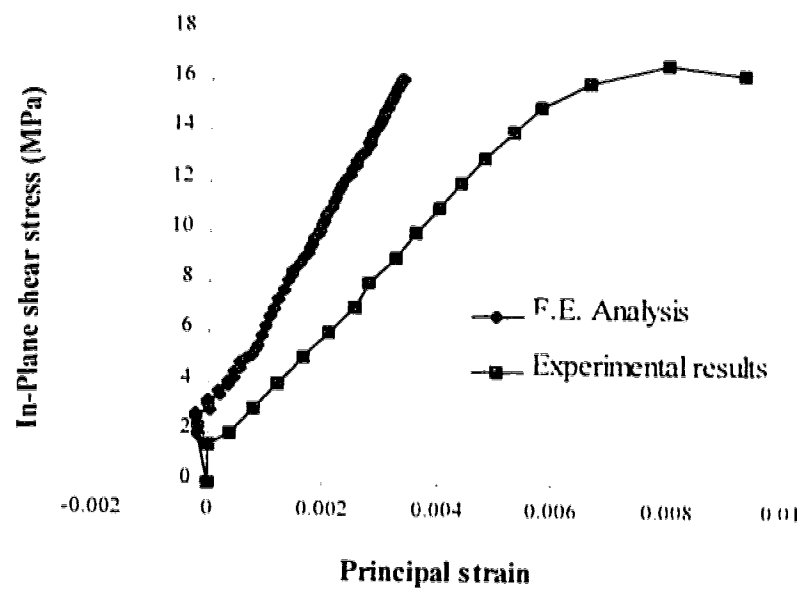
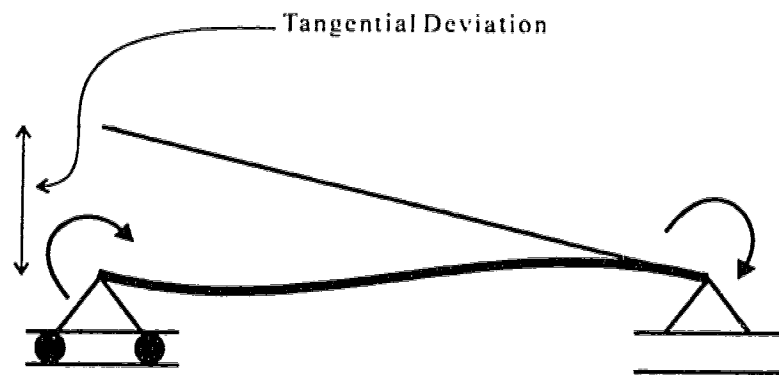
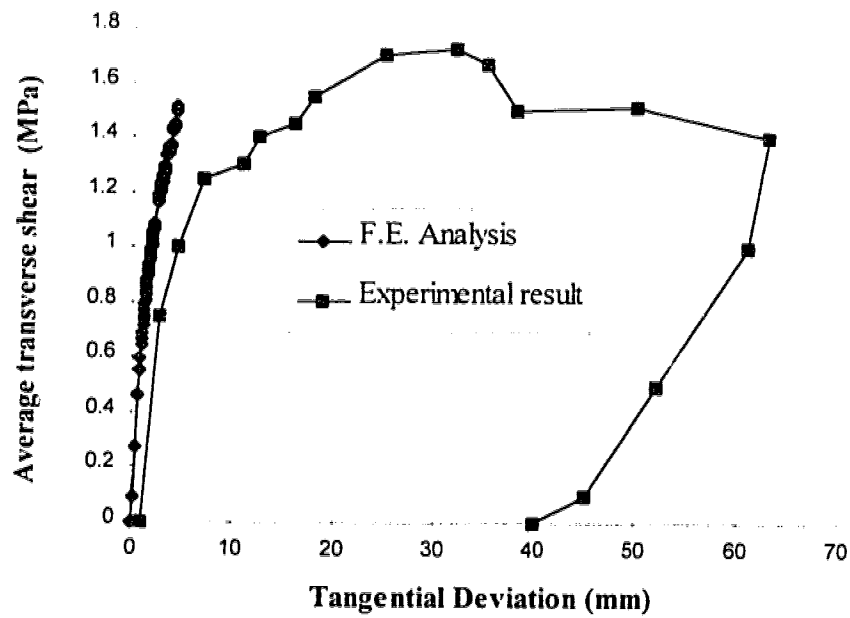


Figure 5.21 In-plane shear stress vs. principal strain in SP8 specimen



(a)- Definition of tangential deviation in SP3 specimen



(b)

Figure 5.22 Load-deformation response of SP3 specimen

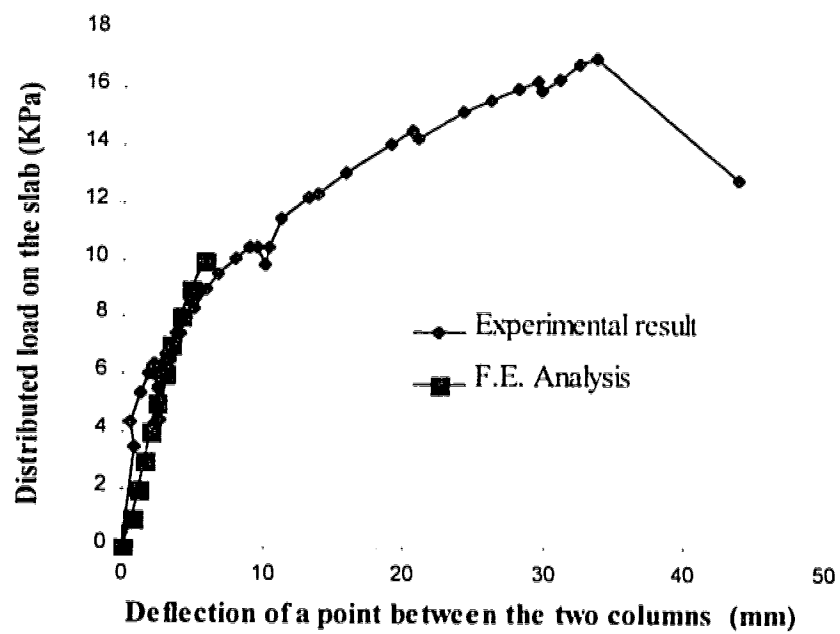
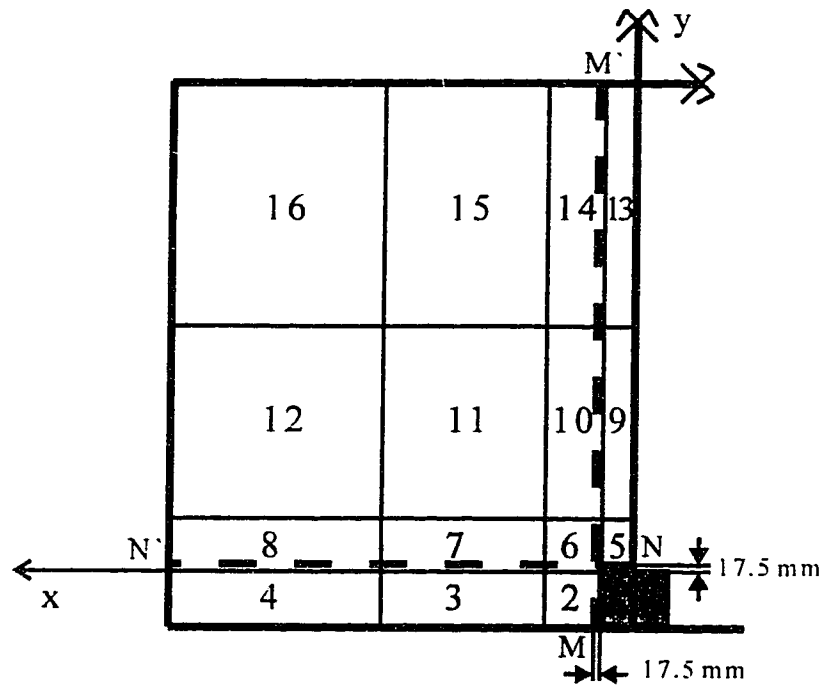


Figure 5.23 Load deformation behavior of Afhami et al. slab-column connection at point C



(a)- Finite element mesh for edge slab-column connection

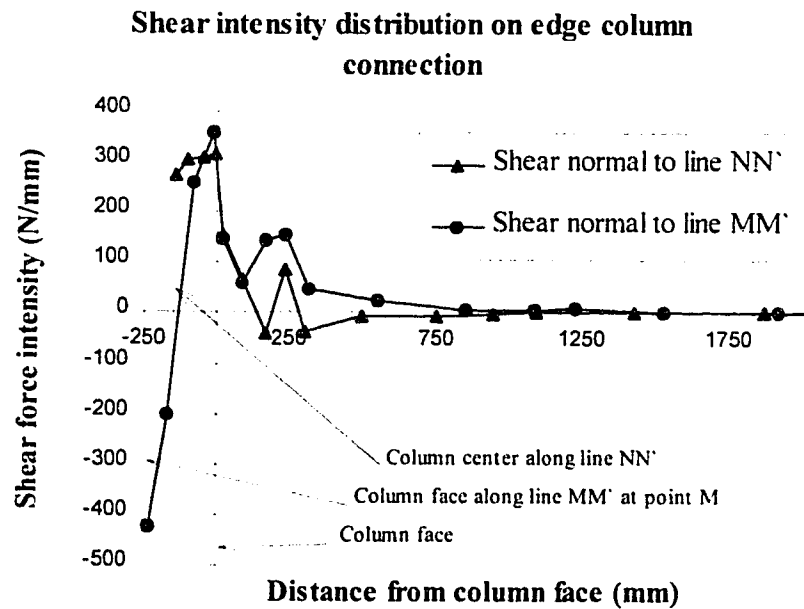


Figure 5.24 Shear intensity distribution on the face of interior strip and edge strip in the Afhami et al. specimen

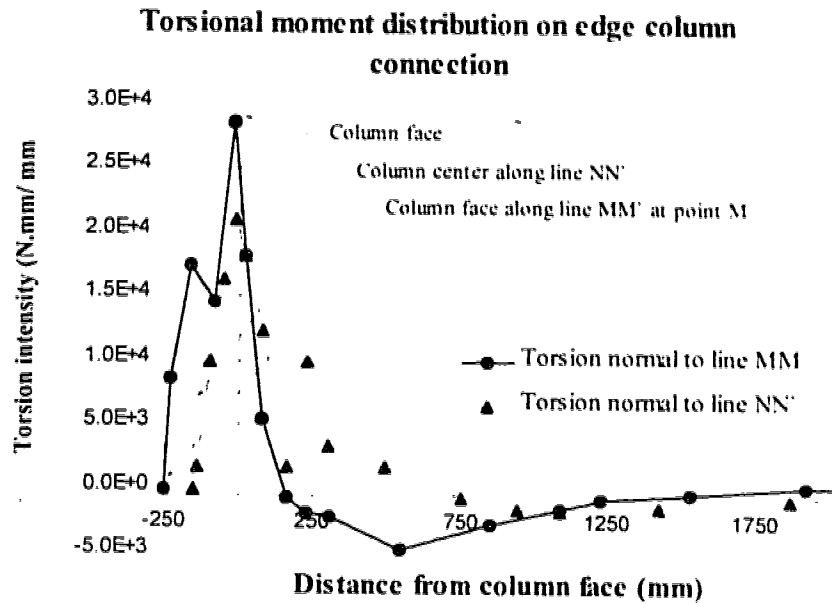


Figure 5.25 Torsional moment intensity on the face of interior strip and edge strip in the Afhami et al. specimen

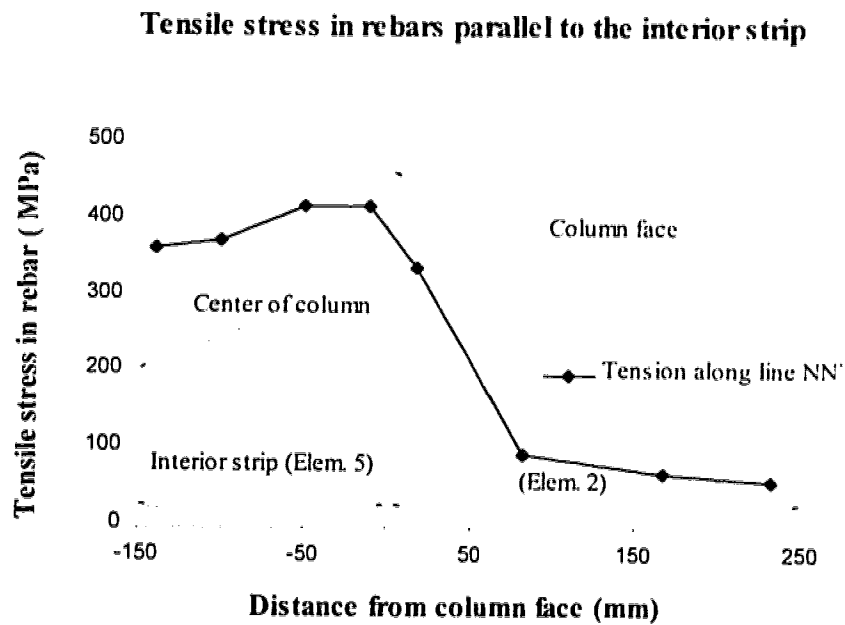
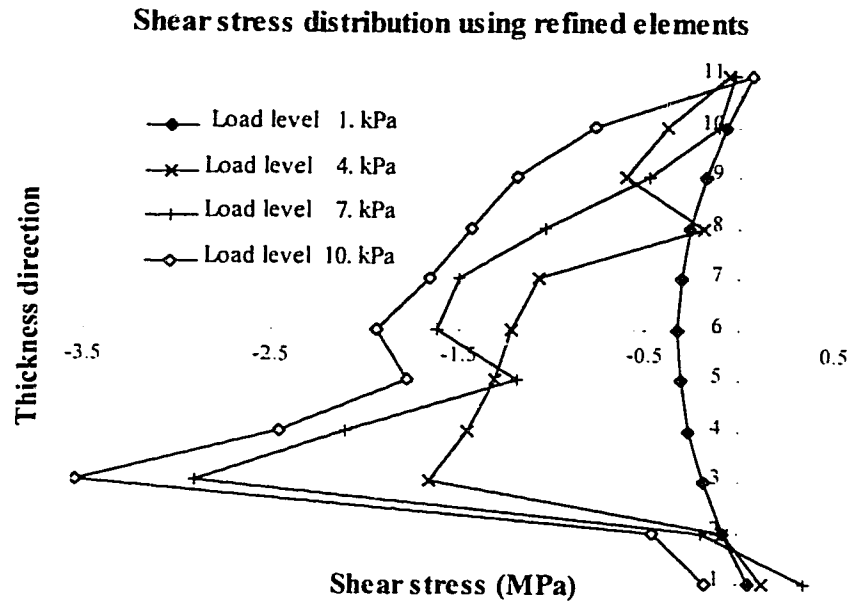
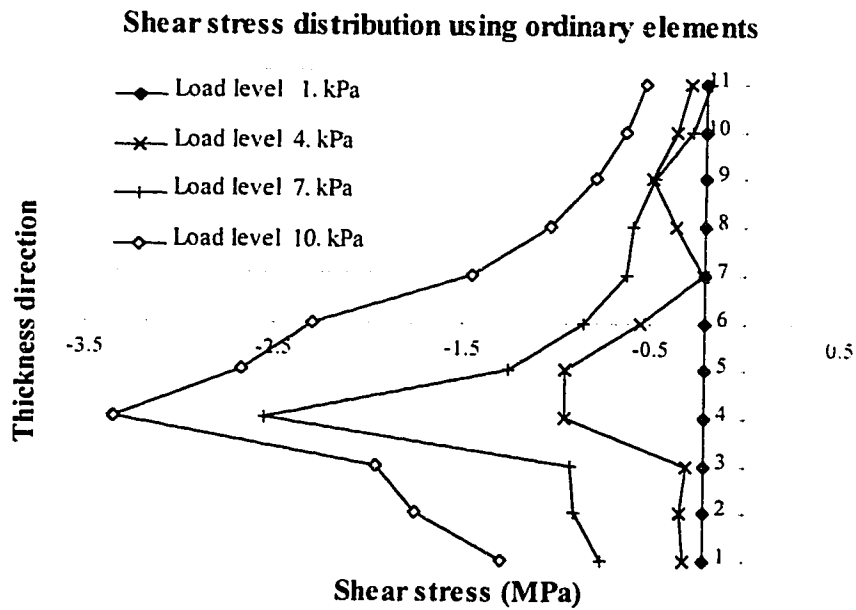


Figure 5.26 Tension in outer layer of reinforcement in the Afhami et al. slab-column connection



(a)



(b)

Figure 5.27 Shear stress distributions in Afhami et al. slab-column connection using refined and ordinary shell elements

CHAPTER SIX

SUMMARY AND CONCLUSION

6.1 Summary

The main objective in this study is to develop a finite element model for thick plate and shell structures in the region of high transverse shear force.

As the first step, a new shell element with the unique ability to adjust its strain field approximation to fit the actual distribution of strain in the structure has been developed. The new element is based on continuum approach in finite element formulation of shell elements and it is called “*Refined Degenerated Shell Element*”.

Analysis of plates and shells in the region of high transverse shear force requires a more accurate strain field representation in finite element modeling of structure. Using three dimensional elements is not practical in most cases and shell elements are usually preferred. Although some traditional plate-shell elements relax the constraint that normal cross sections remain normal to the neutral plane during transverse shear deformation, the section is still constrained to remain plane. The work reported here relaxes this constraint by introducing *shape functions across the thickness* to approximate the transverse shear strain field in the thickness direction. These shape functions are treated in the manner of *generalized rotations*, similar to the actual rotational degrees of freedom, undergoing small deformations. They are added, as new degrees of freedom, to the ordinary displacement field of the degenerated shell elements. The field is still able to simulate large deformation behavior of the element. Each shape function yields two independent variables, one in each direction.

By using the concept of shape functions across the thickness, the strain field approximation of the refined element is easily adjustable to different applications. In this work, two types of shape functions are proposed allowing a *parabolic transverse shear strain as well as an unsymmetric transverse shear strain distribution* in the thickness direction. These two modes of deformation are particularly important in the case of diffused material failure in concrete shell structures.

The performance of the new element has been tested in different applications using elasto-plastic material models. The results indicate that, the two sets of shape functions implemented in this model effectively remove the assumption that plane sections remain plane and a more realistic response for the structure has been followed. Also corresponding results are shown to be consistent even in the presence of strong discontinuities in the transverse shear force in the structure.

In the last phase of this study finite element modeling of concrete plate and shells has been discussed and problems associated with high transverse shear forces are highlighted. Localized fracture zone in this area reduces the level of continuity in displacement field (and its derivatives) of the structure. Finite element modeling of discontinuity needs a more sophisticated approach in discretization of the structure to remove mesh dependency problems in the numerical model. In addition, the significant amount of out of plane shear force in that region causes a three dimensional state of stress in concrete that can no longer be represented by orthotropic models usually available for concrete.

A three dimensional fracture energy based plasticity material model for concrete has been adopted in this study to address both of these problems. In addition to its three dimensional nature, the fracture energy based characteristics of the model can also reduce mesh dependency in finite element model. This material model is based on the Willam and Paramono (1989) approach and has been modified to account for the state of stress in plates and shells. The material model has been verified later in some shear dominated

states of stress pertinent to the stress field in plates and shells in the zone of high transfer shear force.

As the last step, the performance of the finite element model was examined in two different examples of high transverse shear forces: shear failure of a thick plate and punching shear of a thin slab. Numerical analysis revealed some of the characteristics of finite element model developed in this study. The ability of the refined shell elements to adjust its strain field approximation to the actual domain of strain in the structure was verified in the analysis of these examples. However it was shown that in some special cases a more sophisticated integration algorithm across the thickness is required. The concrete material model also revealed some of its shortcomings: numerical instability, problems in extensive cracking zone, calibration parameters and sensitivity to the increment of strain tensor.

Finite element analysis could not reach the ultimate load carrying capacity of the specimens reported in the test results. The growing inaccuracy in the numerical model due to problems in the concrete material model, led to instability in the analysis and caused convergence problem. The analysis was terminated thereafter. The numerical model, however, was able to qualitatively represent the behavior of the structures.

6.2 Conclusion

The new refined shell element developed in this study is quite successful in almost all the examples solved in the course of this study and it has a potential to be used in some other areas of application (multi-layered composite shells, for example) besides concrete structures. The adjustability concept of the element and the ease of programming in this approach provides the required versatility for this element to be used as a general shell element in refined applications. Also it can substitute the three dimensional modeling of the shell structures with brick elements in a variety of examples when ordinary shell elements are not rendering an accurate strain field in the structure.

However, the capability of this new element in the context of concrete structures was not invoked properly in this study due to problems in the concrete material model. The material model has shown good performance in three dimensional compression states of stress (see, Xie et al. 1994) but, to be able to use it in plate and shell applications, it has to be modified for shear and tension dominated state of stresses.

REFERENCES

- Abbasi, M.S.A., Baluch, M.H., Azad, A.K. and Abdel-Rahman, H.H. (1993). "Sensitivity study of criteria Governing Collapse of Centrally Loaded R/C Slabs." *Engineering Computations*, Vol. 10, pp. 175-187.
- Adebar, P.E., (1989). "*Shear Design of Concrete Offshore Structures*", Ph.D. Thesis, University of Toronto, Canada.
- Afhami, S., Alexander, S.D.B. and Simmonds, S. (1996). Research in progress, Department of Civil Engineering, University of Alberta, Edmonton, Canada.
- Ahmad, S., Irons, B. M. and Zienkiewicz, O.C. (1968). "Curved thick shell and membrane elements with particular reference to axi-symmetric problems." *Proc. 2nd conf. Matrix Methods in Structural Mechanics*, Wright-Patterson Air Force Base, Ohio.
- Alexander, S.D.B. and Simmonds, S.H. (1992). "Bond Model for Concentric Punching Shear." *ACI Structural Journal*, V. 89, No. 3, pp. 325-334.
- Averill, R.C. and Reddy, J.N. (1992). "An Assessment of four-noded Plate Finite Elements Based on a Generalized Third-order Theory." *International Journal for Numerical Methods in Engineering*, Vol. 33, pp. 1553-1572.
- Balakrishnan, S., Elwi, A.E. and Murray, D.W. (1988). "Effect of Modeling on NLFEA of Concrete Structures", *Journal of Structural Engineering*, ASCE, Vol. 114, No. 7, pp. 1467-1487.
- Barzegar, F. (1988). "Layering of RC Membrane and Plate elements in Nonlinear Analysis." *Journal of Structural Engineering*, ASCE, Vol. 114, No. 11, pp. 2474-2492.
- Basar, Y., Ding, Y. and Schultz, R. (1993). "Refined shear-deformation models for composite laminates with finite rotations." *Int. J. Solids Struct.* Vol. 30, pp. 2611-2638.
- Bathe, K.J., Walczak, J., Welch, A. and Mistry, N. (1989). "Nonlinear Analysis of Concrete Structures." *Journal of Computers and Structures*, Vol. 32, No. 3/4, pp. 563-590.
- Bazant, Z.P. (1976). "Instability, Ductility and Size Effect in Strain-Softening Concrete." *Journal of Engineering Mechanics*, ASCE, Vol. 102, No. EM2, pp. 331-344.
- Bazant, Z.P. (1984). "Microplane Model for Strain Controlled Inelastic Behavior." *Mechanics of Engineering Materials*, Desai, C.S. and R.H. Gallagher, eds., John Wiley and Sons, New York, N.Y., PP. 45-59.

- Bazant, Z.P. (1988-a). "Why Continuum Damage is Nonlocal : Micromechanics Arguments." *Journal of Engineering Mechanics*, ASCE, Vol. 117, pp. 1070-1087.
- Bazant, Z.P. and Gambarova, P. G. (1984). "Crack Shear in Concrete: Crack Band Microplane Model." *Journal of Structural Engineering*, ASCE, Vol. 110, No. 9, pp. 2015-2035.
- Bazant, Z.P. and Kim, S. (1979). "Plastic Fracturing Theory for Concrete." *Journal of the Engineering Mechanics Division*, ASCE, Vol. 105, No. EM3, PP. 407-428.
- Bazant, Z.P. and Oh, B.H. (1983). "Crack Band Theory for Fracture of Concrete Material and Structures." *RILEM*, Vol. 16, pp. 155-177.
- Bazant, Z.P. and Pijaudier-Cabot, G. (1988-b). "Nonlocal Continuum Damage Localization Instability and Convergence." *Journal of Applied Mechanics*, ASME, Vol. 55, pp. 287-294.
- Bazant, Z.P. and Prat, P.C. (1988). "Microplane Model for Brittle-Plastic Material: I. theory, II. Verification." *Journal of Engineering Mechanics*, ASCE, Vol. 114, No. 10, PP. 1672-1702.
- Bicanic, N., Selman, A., Xie, Y.M. and Pankaj, J. (1991). "On Mesh Dependence of Failure Mode Prediction for Dams." *Proc. Int. Conf. Dam Fracture, Boulder, Colorado*, V. Saouma, R. Dungar and D. Morris (Eds.), EPRI GS-7491, Palo Alto, pp. 3-20.
- Buechter, N. and Ramm, E. (1992). "Shell theory versus Degeneration - A comparison in large rotation finite element analysis." *Int. J. Numer. Methods Eng.*, Vol. 34, pp. 39-59.
- Carol, I., Prat, P. C. and Bazant, Z. P. (1992). "New Explicit Microplane Model for Concrete: Theoretical Aspects and Numerical Implementation." *Int. J. Solids Structures*, Vol. 29, No. 9, pp. 1173-1191.
- Cedolin, L. and Poli, S.D. (1977). "Finite Element Studies of Shear-Critical R/C Beams." *J. Eng. Mech. Div. ASCE*, Vol. 103 (EM3), pp. 395-410.
- Cervera, M. and Hinton, E. (1986). "Nonlinear Analysis of Reinforced Concrete plate and Shells Using a Three Dimensional Model." *Computational Modeling of Reinforced Concrete Structures*, Pineridge Press Limited, Swansea, Chapter 12, pp. 327-370.
- Cervera, M., Hinton, E. and Hassan, O. (1987). "Nonlinear Analysis of Reinforced Concrete plate and Shell Structures Using 20-Noded Isoparametric Brick Elements." *Comput. Struct.*, Vol. 25, pp. 845-869.

- Chan, D.H. (1986). "*Finite Element Analysis of Strain Softening Material*." Ph.D. thesis, Department of Civil Engineering, University of Alberta, Edmonton, Canada.
- Chen, W. F. (1982). "*Plasticity in Reinforced Concrete*.", McGraw Hill, , Vol. 114, No. 10, PP. 1672-1702.
- Clauss, D.B. (1987). "*Round-Robin Pretest Analysis of a 1:6 Reinforced Concrete Containment Model Subject to Static Internal pressurization*." NUREG/CR-4913, SAND87-0891, Sandia National Laboratories, Albuquerque, NM.
- Clauss, D.B. (1989). "*Round-Robin Analysis of the behavior of a 1:6 Reinforced Concrete Containment Model Pressurized to Failure: Posttest Evaluations*." NUREG/CR-5341, SAND89-0349, Sandia National Laboratories, Albuquerque, NM.
- Clough, R. W. and Fellipa, C.A. (1968). "A Refined Quadrilateral Element for Analysis of Plate Bending." *AFTDL-TR-68-150*.
- CSA Standard CAN3-A23.3-M84 (1984). "*Design of Concrete Structures for Buildings*", Canadian Standard Association, Rexdale, Ontario, Canada.
- Damjanic, F. and Owen, D.R.J., J.A. (1984). "Practical Consideration for Modeling of Post-Cracking Concrete Behavior for Finite Element Analysis of Reinforced Concrete Structures." *Proc. of the International Conference on Computer-Aided Analysis and Design of Concrete Structures*, pp. 693-706.
- Darwin, D. and Pecknold, D.A. (1977). "Nonlinear Biaxial Stress-Strain Law for Concrete" *Journal of Engineering Mechanics Division*, ASCE Vol. 103, No. EM2, pp.229-241.
- Drucker, D.C. (1951). "A more Fundamental Approach to Plastic Stress-Strain Relations." *Proc. 1st. U.S. Natl. Congr. Appl. Mech.*, ASME, New York, pp. 487-491.
- Drucker, D.C. (1959). "A Definition of Stable Inelastic Materials." *Journal of Applied Mechanics*, Vol.. 26, pp. 101-106.
- Elwi, A.A. and Murray D.W. (1979). "A 3D Hypoelastic Concrete Constitutive Relationship." *Journal of the Mechanical Engineering Division*, ASCE Vol. 105, No. EM4, pp. 623-641.
- Figueras, J.A. and Owen, D.R.J. (1983). "Anisotropic Elasto plastic Finite Element Analysis of Thick and Thin Plates and Shells." *Int. J. Numerical Methods in Engng.*, Vol. 19, pp. 541-566.

- Gedlin, J.S, Mistry, N.S. and Welch, A.K. (1986). "Evaluation of Material Models for Reinforced Concrete Structures." *Computers and Structures*, Vol. 24, pp. 225-232.
- Gilbert, R.I. and Warner R.F. (1977). "*Nonlinear Analysis of Reinforced Concrete Slabs with tension stiffening*." UNI-CIV Report no. R-167, University of New South Wales, Kensington, N.S.W.
- Hand, F.R., Pecknold, D.A. and Schnobrich, W.C. (1972). "*A Layered Finite Element Nonlinear Analysis of Reinforced Concrete Plates and Shells*." Civil Engng Studies, SRS 389. University of Illinois, Urbana, IL.
- Hibbitt, Karlsson and Sorensen, Inc. (1993). "*ABAQUS-User's Manuals*." Pawtucket, RI, USA.
- Hillerborg, A. (1978). "A Model for Fracture Analysis." *Division of Building Material*., Report TVBM-3005, Lund Institute of Technology, Sweden.
- Hillerborg, A., Modeer, M. and Peterson P.E. (1976). "Analysis of Crack Formation and Crack Growth by Means of Fracture Mechanics and Finite Elements" *Cement and Concrete research*, 6, No. 6, pp. 773-782.
- Hinton, E. and Owen, D.R.J. (1984). "*Finite Element Software for Plates and Shells*." Pineridge Press Ltd. Swansea, U.K.
- Horschel, D.S. (1988-a). "Design, Construction and investigation of a 1/6-Scale Reinforced Concrete Containment Building." *NUREG/CR-5083, SAND88-0030*, Sandia National Laboratories, Albuquerque, NM.
- Horschel, D.S. (1988-b). "Experimental Results for Pressure Testing a 1/6-Scale Nuclear power plant containment." *NUREG/CR-5121, SAND88-0906*, Sandia National Laboratories, Albuquerque, NM.
- Hsieh, S.S., Ting, E.C. and Chen, W.F. (1982). "A Plasticity Fracture Model for Concrete." *International Journal of Solids and Structures*, Vol. 18, No. 3, PP. 181-197.
- Jofriet, J.C. and McNiece, G.M. (1971). "Finite Element Analysis of Reinforced Concrete Slabs." *J. Structural Div. ASCE*, Vol. 97, No. ST3, pp. 785-806.
- Klein, D.G. (1986). "A Finite Element Model for Reinforced Concrete Slabs with Consideration of Transverse Shear Deformation." *Computational Modeling of Reinforced Concrete Structures*, Pineridge Press Limited, Swansea, Chapter 7, pp. 189-216.

Li, Z.H. and Owen, D. R. J. (1989). "Elastic-Plastic Analysis of Laminated Anisotropic Shells by Refined Finite Element Laminated Model." *Comp. Struct.*, Vol. 32, No. 5, pp. 1005-1024.

Liao, C.L., Reddy, J.N. and Engelstad, S.P. (1988). "A Solid-Shell Transitional Element for Geometrically Non-Linear Analysis of Laminated Composite Structures." *International Journal for Numerical Methods in Engineering*, Vol. 26, No. 8, pp. 1843-1854.

Lin, C.S. and Scordelis, A.C. (1975). "Nonlinear Analysis of Reinforced Concrete Shells of general form." *J. Struct. Div. ASCE*, Vol. 101, No. 3, pp. 523-538.

Massicotte, B., Elwi, A.E. and MacGregor, J.G. (1988). "*Analysis of Reinforced Concrete Panels Loaded Axially and Transversally*." Structural Engineering Report No. 161, Department of Civil Engineering, University of Alberta, Edmonton, Canada.

Massicotte, B., MacGregor, J.G. and Elwi, A.E. (1990). "Behavior of Concrete Panels Subjected to Axial and Lateral Loads." *Journal of Structural Engineering*, ASCE, Vol. 116, No. 9, pp. 2324-2343.

Mawenya, A.S. and Davies, J.D. (1974). "Finite Element Bending Analysis of Multilayer Plates." *Int. J. for Numer. Methods in Engr.*, Vol. 8, No. 2, pp. 215-225.

McLean, D.I. (1987). "*A study of the Punching Shear in Arctic Offshore Structure*." Ph.D. Dissertation, Civil Engineering Department, Cornell University, Ithaca, NY.

Menetrey, Ph. and Willam, K.J. (1995). "Triaxial Failure Criterion for Concrete and its Generalization." *ACI Structural Journal*, Vol. 92, No. 3, PP. 311-318.

Moe, J. (April 1961). "*Shearing Strength of Reinforced Concrete Slab and Footings under Concentrated Loads*." Development Department Bulletin, No. D47, Portland Cement Association, Skokie.

Moehle, J.P., Kreger, M.E. and Leon, R. (1988). "Background to Recommendations for Design of Reinforced Concrete Slab-Column Connections." *ACI Structural Journal*, V. 85, No. 6, pp. 636-644.

Ngo, D. and Scordelis, A.C. (1967). "Finite element analysis of reinforced concrete beams." *Journal of American Concrete Institute*, ACI, Vol. 64, pp. 152-163.

Noguchi, h. and Schnobrich, W.C. (1993). "Finite Element Analysis of Reinforced Concrete in Japan and US: Introduction and Overview." *Proceeding of the International Workshop on Finite Element Analysis of Reinforced Concrete Structures II*, Published by ASCE, New York, NY, pp. 1-35.

Noor, A.K. and Burton, W.S. (1989). "Assessment of Shear Deformation Theories for Multilayered Composite Plates." *Appl. Mech. Rev. ASME*, Vol. 42, No. 1, pp. 1-13.

Oliver, J. (1989). "A Consistent Characteristic length for smeared crack analysis." *Int. J. for Numerical Methods in Engineering*, Vol. 28, pp. 461-474.

Oliver, J. (1995). "Continuum Modeling of Strong Discontinuities in Solid Mechanics." *Proceedings COMPLAS 4 Barcelona*, Pineridge Press, Swansea, UK, pp. 455-479.

Oliver, J. and Simo, J.C. (1994). "Modeling Strong Discontinuities by means of Strain Softening Constitutive Equations." *Euro-C 1994, Computer Modeling of Concrete Structures*, Pineridge Press, Swansea, UK, pp. 363-372.

Ortiz, M. and Quigley, J.J. (1989). "Element Design and Adaptive Meshing in Strain Localization Problems." *Proceedings COMPLAS 2 Barcelona*, Pineridge Press, Swansea, UK, pp. 213-236.

Ortiz, M. and Quigley, J.J. (1991). "Adaptive Mesh Refinement in Strain Localization Problems." *Comp. Meth. Appl. Mech. Engrg*, Vol. 90, pp. 781-804.

Ottosen, N.S. (1977). "A Failure Criterion for Concrete." *Journal of the Engineering Mechanics Division*, ASCE, Vol. 103, No. EM4, PP. 527-535.

Ottosen, N.S. (1979). "Constitutive Model for Short Term Loading of Concrete." *Journal of the Engineering Mechanics Division*, ASCE, Vol. 105, No. EM1, PP. 127-141.

Owen, D. R. J. and Li, Z.H. (1987). "A Refined Analysis of Laminated Plates by Finite Element Displacement Methods -I. Fundamentals and Static Analysis, II. Vibration and Stability." *Comp. Struct.*, Vol. 26, No. 6, pp. 907-923.

Owen, D.R.J. and Figueiras, J.A. (1984). "Ultimate Load Analysis of Reinforced Concrete Plates and Shells Including Geometric Nonlinear effects." *Finite Element software for Plates and Shells*, Pineridge Press, Swansea, pp. 327-388.

Paramono, E. and Willam, K. (1989). "Fracture Energy-Based Plasticity Formulation of Plain Concrete." *Journal of Engineering Mechanics*, ASCE, Vol. 115, No. 6, pp. 1183-1204.

Ramm, E. (1976). "Geometrisch nichtlineare Elastostatik und finite Elemente." Habilitation, Bericht Nr. 76-2, Institut für Baustatik, Universität Stuttgart, Germany.

Ramm, E. (1977). "A Plate/Shell element for large deflections and rotations." *U.S.-Germany Symp. on formulations and computational Algorithms in finite element analysis*, MIT 1976, MIT press.

Rashid, Y.R. (1968). "Analysis of Prestressed Concrete pressure Vessels." *Nuclear Engng. Design*, Vol. 7, pp. 334-344.

Reddy, J. N. (1987). "A small strain and moderate rotation theory of elastic Anisotropic plates." *J. Appl. Mech.* Vol. 54, pp. 623-626.

Reddy, J. N. (1989). "On refined computational models of composite laminates." *Int. J. Num. Meth. Engng.* Vol. 27, pp. 361-382.

Reddy, J.N. (1984-a). "A simple high-order theory for laminated composite plates." *J. Appl. Mech.* Vol. 51, pp. 745-752.

Reddy, J.N. (1984-b). "A Refined nonlinear theory of plates with transverse shear deformation." *Int. J. Solid Struct.* Vol. 20, pp. 881-896.

Regan, P.E. and Braestrup, M.W. (1985). "Punching Shear in Reinforced Concrete: A State of Art Report." *Bulletin d'Information*, No. 168, Comité, Euro-International Du Béton, Lausanne, Switzerland, pp. 72-75.

Reissner, E. (1945). "The effect of transverse shear deformation on the bending of the elastic plates." *J. Appl. Mech.* Vol. 12, pp. 69-77.

Romano, M. (1969). "On Leon's Criteria." *Meccanica*, PP. 48-66.

Rots, J.G. (1988). "Computational Modeling of Cracked Concrete." Ph.D. thesis, Dept. of Civ. Engrg, Delft Univ. of Technology, Delft, The Netherlands.

Rots, J.G. and deBorst, R. (1987). "Analysis of Mixed Mode Fracture in Concrete." *Journal of Engineering Mechanics*, ASCE, Vol. 113, No. 11, PP. 1739-1758.

Saito, H., et al. (1989). "Experimental Study on RCCV of ABWR Plant." *Transaction of the 10th International Conference on Structural Mechanics in Reactor Technology*, Vol. J., Japan.

Scanlon, A. (1971). "Time Dependent Deflections of Reinforced Concrete Slabs." Ph.D. dissertation, Department of Civil Engineering, University of Alberta, Edmonton, Canada.

Scordelis, A.C. and Chan, E.C. (1987). "Nonlinear Analysis of Reinforced Concrete Shell." *Computer Applications in Concrete Technology*, ACI-SP-98, American Concrete Inst., Detroit, Mich., pp. 25-57.

Simo, J.C. and Rafai, M.S. (1990). "A Class of Mixed Assumed Strain Methods and the Method of Incompatible Modes." *Int. J. Num. Meth. Engng.*, Vol. 29, pp. 1595-1638.

Simo, J.C. Oliver, J. and Armero, F. (1993). "An Analysis of Strong Discontinuities Induced by Strain-Softening in Rate-Independent Inelastic Solids." *Computational Mechanics*, Vol. 12, pp. 277-296.

Stegmuller, H., Hafner, L., Ramm, E. and Satteler, J. M. (1983). "*Theoretische Grundlagen zum FE-programm system NISA-80*." Mitteilung Nr. 1, Institut für Baustatik der Universität Stuttgart, Germany.

Steinmann, P. and Willam, K. (1991-a). "Finite Elements for Capturing Localized Failure." *Archive of Applied Mechanics*, Springer-Verlag, 61, pp. 259-275.

Steinmann, P. and Willam, K. (1991-b). "Performance of Enhanced Finite Element Formulation in Localized Failure Computations." *Comp. Meth. Appl. Mech. Engrg.* Vol. 90, pp. 845-867.

Van Mier, J.G.M. (1984). "*Strain-Softening of Concrete under Multi-axial Loading Conditions*." Ph.D. Dissertation, Technische Hogeschool Eindhoven.

Vecchio, F.J. and Collins, M.P. (1982). "*The Response of Reinforced Concrete to Inplane Shear and Normal Stresses*." Report No. 82-03, Department of Civil Engineering, University of Toronto, Toronto, Canada.

Weatherby, J.R. (1990). "*Posttest Analysis of a 1:6 Scale Reinforced Concrete Reactor Containment Building*." NUREG/CR-5476, SAND89-2603, Sandia National Laboratories, Albuquerque, NM.

Wempner, G. (1989). "Mechanics and Finite Elements of Shells." *Applied Mech. Rev.*, ASME, Vol. 42, No. 5, pp. 129-142.

Willam, K., Hurlbut, B. and Sture, S. (1986). "Experimental and Constitutive aspects of Concrete Failure." *Finite Element Analysis of Reinforced Concrete structure*, ASCE Publications, NY, pp. 226-254.

Willam, K.J. and Warnke, E.P. (1974). "Constitutive Model for the Triaxial Behavior of Concrete." *IABSE Seminar on Concrete Structure Subjected to Triaxial Stresses*, Paper III-1 Bergamo, Italy.

Xie, J., Elwi, A.E. and MacGregor, J.G. (1994). "*Numerical Investigation of Eccentrically Loaded Tied High Strength Concrete Columns*." Structural Engineering Report, University of Alberta, Edmonton, Alberta, Canada.

Zienkiewicz, O.C. and Zhu, J.Z. (1987). "A Simple Error Estimator and Adaptive Procedure for Practical Engineering Analysis." *Intl. J. Num. Meth. Engng.*, 24, pp. 337-357.

Ziyaeifar, M. and Elwi A.E. (1995) "Elasto-Plastic Response of Degenerated Plate-Shell Elements with Variable Transverse Shear Strain." *Proceeding of the Fourth International Conference on Computational Plasticity, Barcelona, Spain*, Owen, D.R.J., Onate, E and Hinton, E. eds., Pineridge Press, Swansea, Vol. 2, , pp. 2037-2047.

Ziyaeifar, M. and Elwi A.E. (1996-a) "Degenerated Plate Shell Elements with Refined Transverse Shear Strain." *Journal of Computers and Structures*, Vol. 60, No. 6, pp. 1079-1091.

Ziyaeifar, M. and Elwi A.E. (1996-b) "Adjustable Refined Strain Field in Degenerated Shell Elements ❶ ." *Journal of Finite Elements in Analysis and Design*, Vol. 22, No. 1, pp. 85-91.

❶ This paper was qualified as a candidate in 1995 R.J. Melosh Competition for the best student paper in finite element method.